UNIVERSITÀ DEGLI STUDI DI NAPOLI "FEDERICO II"
FACOLTÀ DI SCIENZE MATEMATICHE, FISICHE E NATURALI

Dottorato di Ricerca in Fisica Fondamentale ed Applicata
ciclo XIX

DISSERTAZIONE

High Energy Astronomy and Astrophysics with Cosmic Rays and Gamma particles

di

ALESSANDRO CUOCO

Il Coordinatore:
Prof. G. Miele

NOVEMBRE 2006

Abstract

Our knowledge of the universe has been derived, since now, from observations of the electromagnetic radiation in a quite narrow range near the optical band. However, advances in detectors technology allow at present either to enlarge the electromagnetic energy band explored, as in the case of γ-astronomy in the TeV range, either to consider other types of radiations like neutrinos, Cosmic Rays or, possibly, gravitational waves.

This dissertation deals in particular with gamma and cosmic rays. Likely, the first step toward CR astronomy would be the detection of correlation between the related all-sky diffuse emission and the cosmological Large Scale Structures. In the first part of the dissertation the possibility to recognize the cosmological LSS with CRs of $E > 10^{19}$eV is explored, while the first hints of this signal from the actual available statistics are carefully checked. In the second part of the dissertation the expected correlation of LSS and the diffuse emission from γ-rays is also studied, looking for the prospects of detection with the next generation of γ-observatories. The possibilities to use the diffuse gamma anisotropies like a tool for Dark Matter γ-emission searches are also investigated.

Keywords:
Astroparticle Physics, Cosmic Rays, Large Scale Structures, Gamma Astronomy

Preface

Traditional astronomy has, until now, explored the universe in a wide energy window ranging from the very low radio frequencies, passing through the infrared and optical, until the X-band at the KeV-GeV energy. The range of observed frequencies is slowly but steadily expanding in both direction: new large-area radio telescopes plan to perform detailed high-redshift surveys of the low frequency universe, while the novel discipline of γ-astronomy in the last fifteen years has created a new picture of the sky in the TeV energy range.

Particles above the TeV range, due to the very low flux expected, can be observed only indirectly through the secondaries and the showers they produce interacting with the earth's atmosphere. The flux of these high energetic particles, commonly named Cosmic Rays, is largely dominated by atomic nuclei, mainly protons, with only about a fraction 10^{-5} of photons. A brief review of the physics of CRs is provided in chapter 1. Nonetheless, advances in the the techniques of gamma/hadron shower discrimination in the TeV range have allowed the development of ground-based gamma astronomy. Doubts remains about the possibility to use directly the bulk of charged cosmic rays to perform astronomy until the highest energies observed, of the order of 10^{20}eV. The main difficulty comes from the presence of the galactic and extragalactic magnetic fields. They are extremely weak, of the order μG for galactic fields and nG for the extragalactic, but intense enough to bend the trajectories of CRs along distances of kpc or Mpc, scrambling their arrival directions and hiding the direct astrophysical information. In practice, in this regime, only statistical considerations can be made about the sources.

Nonetheless, in the Ultra High Energy (UHE) range ($>10^{19}$eV) the kinetic energy and magnetic rigidity of CR particles is such that hundreds Mpc distances can be traveled with deflection of few degrees, partially restoring the initial directional information. Interestingly, at these energies CR particles loose rapidly energy in the interaction with the Intergalactic Medium so that only particles coming from few times 100 Mpc, a relatively short distance in cosmological term, can reach the earth. Given the relevance that the Large Scale Structure of the universe plays throughout this dissertation, a brief introduction of the issue is contained in chapter 2. UHE astronomy of the Nearby Universe seems then possible though the very low statistics is the major limitation, the CR flux at this energy being less of 1 particle

per century per km^2. With this statistics, basically two kind of astrophysical scenario could be supported: i) the 10^{20}eV sky is dominated by few nearby powerful sources and even with very few detected events we should see them clustered in spots or multiplets; ii) the sources are weak and numerous: they cannot be singularly resolved but we can see their diffuse emission in the form of an almost uniform distribution of events. Possibly, tiny anisotropies due to the clustering properties of the sources could be present. A third scenario (iii) could be possible in which the emission is not of astrophysical origin but is related, instead, to new physics, like the decaying of super-massive particle or of topological defects. The primary goal of astronomy at this energy is thus the discrimination of these scenarios.

After that the small clustering of few events observed by the AGASA experiment has not been confirmed by other independent observations, at the moment the scenario ii) is the most attracting. This issue is the main topic of chapter 3 in which the problem of statistics and the kind of anisotropy signal expected in the sky is discussed in detail. The chapter is based on the publication:

> [I] A. Cuoco, R. D. Abrusco, G. Longo, G. Miele and P. D. Serpico, "The footprint of large scale cosmic structure on the ultra-high energy cosmic ray distribution," JCAP **0601** (2006) 009 [astro-ph/0510765].

Actually, in this scenario a reasonable hypothesis is that the sources of UHECRs trace the Large Scale distribution of matter in the nearby universe; the distribution of the events is then expected to show some large scale anisotropy correlated with the local distribution of matter. To gain insight in this problem we use the information relative to this matter anisotropy, available through various astronomical catalogues like PSCz, 2Mass, SDSS and the 2dF, to build a simple model of the pattern and intensity of the expected fluctuations. This model can then be used to forecast the statistics needed to robustly test this scenario. Luckily, the results confirm that the required statistics is reachable in few years of operation of the large-area AUGER observatory, hopefully providing the answer to these uncertainties.

Even if the actual statistics is not enough to draw strong conclusion on the subject, it is worth testing the actual data looking for some first hints of anisotropies. Interestingly, very recently has been found that clustering proprieties of the actual available data (of the order of 100 events) have a prominent peak at about 20° showing then a large scale anisotropy. In chapter 4 we test this signal comparing it with what expected from scenario ii). We found that Large Scale Structures anisotropies nicely explain the characteristics of the data clustering features. Indeed, the evidence is still not very strong, about 3-σ, and need to be confirmed by higher statistics,

however it could be certainly a first step towards the CR origin clarification. The chapter is based on the paper:

[II] A. Cuoco, G. Miele and P. D. Serpico, "First hints of large scale structures in the ultra-high energy sky?," astro-ph/0610374.

The rest of the dissertation is devoted to γ-astronomy. An introduction to the field is offered in chapter 5. The link with the first part is offered again by the local LSS: γ propagating through the intergalactic medium at TeV energies suffer an attenuation similar to UHECRs, this time due the e^+e^- Pair Production on the Infrared/Optical background, that, again, introduces a gamma-horizon of few hundreds Mpc. The extragalactic γ-background, discovered only few years ago by EGRET, is then expected to show anisotropies correlated with the LSS pattern in the local universe, similarly to the case of UHECR. We study the expected anisotropies in chapter 6; the chances of detection are then addressed in the light of the forthcoming satellite and ground-based detectors. The chapter is based on the paper:

[III] A. Cuoco, S. Hannestad, T. Haugbølle, G. Miele, P. D. Serpico and H. Tu, "The Signature of the Large Scale Structures on the very-high energy gamma-ray sky," (in preparation)

These anisotropy studies are important also for the prospects of search for indirect Dark Matter emission. Dark Matter, in fact, is expected to self-annihilate, though with a very slow rate, producing γ photons just in the 100 GeV-10 TeV range (the exact value depending on the underlying DM mass). The extragalactic γ-background anisotropies could then be a powerful mean to disentangle the DM emission from the ordinary astrophysical contribution.

In the 3-years period of my PhD at Naples I worked also on other arguments besides that presented in this dissertation, that I briefly summarize below.

Neutrino Astronomy
Considering different types of radiation other than the electromagnetic constitutes one of the most powerful means to extend our knowledge of the universe. Besides the Cosmic Rays, considered above, a very promising messenger is the neutrino which, with its very weak interaction properties, allows in principle to test the very distant universe or the inner and denser core of the astrophysical accelerators. Unluckily, just because of these weak interactions, the construction of a neutrino telescope results extremely difficult, requiring large amounts of target material for the detection. The actual efforts are converging towards a km^3 detectors placed both in ice or water. No

extraterrestrial neutrinos has been detected yet (apart from the exceptional case of emission from Sn1987A and the usually detected solar neutrinos). At the moment, then, Neutrino astronomy is still in a phase of detector characterization. In particular, in the work:

[IV] A. Cuoco, G. Mangano, G. Miele, S. Pastor, L. Perrone, O. Pisanti and P. D. Serpico, "Ultra high energy neutrinos in the Mediterranean: Detecting ν_τ and ν_μ with a km^3 telescope," astro-ph/0609241.

is performed a study of the ultra high energy neutrino detection performances of a km^3 Neutrino Telescope sitting at the three proposed sites for ANTARES, NEMO and NESTOR in the Mediterranean sea. The attention is focused on the effect of the underwater surface profile on the total amount of yearly expected τ and μ crossing the fiducial volume in the limit of full detection efficiency and energy resolution. Also emphasized is the possible enhancement of matter effect by a suitable choice of the geometry of the Telescope.

Primordial nucleosynthesis, Cosmic Microwave Background and Large Scale Structure Clustering

One of the goals of cosmology is to pursue the universe as far as possible in time. Cosmic Microwave Background (CMB), the relic thermal emission of Big Bang explosion at $T \simeq 2.73^\circ K$, and Primordial nucleosynthesis (BBN) are the means to observe the universe when its age was 100,000 yrs and few minutes only, respectively. Their study allows then to compare the standard model of cosmology at two very different ages and to test the overall cosistency. In particular, in the work:

[V] A. Cuoco, F. Iocco, G. Mangano, G. Miele, O. Pisanti and P. D. Serpico, "Present status of primordial nucleosynthesis after WMAP: results from a new BBN code," Int. J. Mod. Phys. A **19** (2004) 4431 [astro-ph/0307213].

theoretical estimates for nuclei abundances, along with the corresponding uncertainties, are evaluated using a new numerical code. The combined analysis of CMB and primordial nucleosynthesis prediction for Deuterium produces results in good agreement with the simplest scenario of three non degenerate neutrinos. A slight discrepancy, instead, appears when ^4He mass fraction measurements are considered, pointing toward a systematic in the measurement or, possibly, to the effect of exotic physics, like a slightly degenerate relic neutrino background.

CMB measurements seems, moreover, at present time, the only way to gain some insight on the analogous background of cosmological neutrinos

(with $T \simeq 1.95^{\circ}K$), not detectable in a direct way but, whose presence, influences the pattern of the anisotropies in CMB data. Additional information is also provided by the power spectrum of LSS, as measured for example by SDSS and 2dF, whose slope is sensitive to the presence of neutrinos. In the work:

[VI] A. Cuoco, J. Lesgourgues, G. Mangano and S. Pastor, "Do observations prove that cosmological neutrinos are thermally distributed?," Phys. Rev. D **71** (2005) 123501 [astro-ph/0502465].

the usual assumption that relic neutrinos possess a Fermi-Dirac distribution, is tested. A Bayesian likelihood analysis is performed showing that current cosmological observations of BBN abundances, CMB anisotropies and LSS clustering are compatible with very large deviations from the standard picture.

Contents

Chapter 1

Brief review of Cosmic Ray physics

Cosmic rays represent one of the most fascinating research themes in modern astronomy and physics. The field is very wide and involves many different aspects like particle physics, cosmology, high-energy astrophysics and astronomy. In this chapter a brief review of the various involved issue is presented together with a basic description of the various experimental techniques and some of the (pre-Auger) observational results. To integrate the material presented here, suggested further readings are for instance [1; 2; 3] and the extensive reviews [4; 5; 6; 7; 8].

1.1 Introduction

Cosmic rays, first discovered by Victor Hess in 1912, are mainly charged particles accelerated at very high energies by astrophysical sources located anywhere beyond the atmosphere of the Earth. 89% of cosmic rays consists of protons, followed by $\alpha-$particles ($\sim 10\%$) and heavier nuclei ($\sim 1\%$) [1]. All elements of the periodic table, including transuranic elements, have been detected. More details on the composition of cosmic rays can be found in Ref. [1] and references therein.

Within the flux of incoming particles one can distinguish different components. The most relevant ones are galactic CR (GCR) and solar energetic particles (SCR). GCR originate from sources located in our galaxy outside the solar system. It is believed that GCR are a consequence of astrophysical events like stellar flares, stellar coronal mass ejections, supernova explosions, particle acceleration by pulsars. The smallest detectable energy of GCR is about 1 GeV. Below this energy, the screening effect of the solar wind is too strong to allow them to penetrate the heliosphere [9].

The number of particles at a certain energy E within a certain small energy interval dE is called the spectrum. Cosmic rays have usually a powerlaw

[1] It should also be noted that the flux of particles below the energy of 10GeV strongly depends on the 11–year solar cycle.

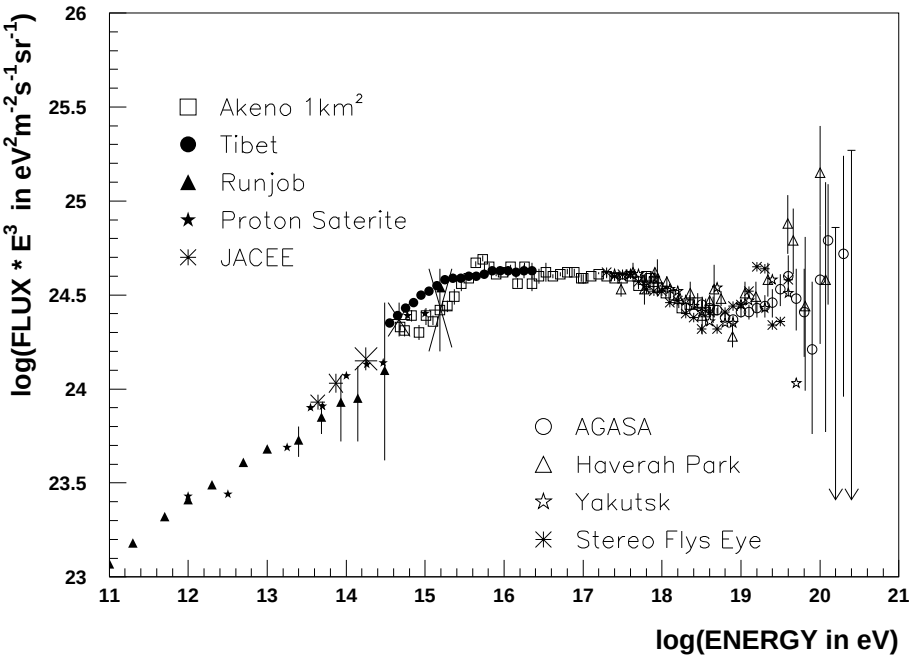

Figure 1.1: The CR all-particle spectrum observed by different experiments above 10^{11} eV (from Ref. [4]). The differential flux in units of events per area, time, energy, and solid angle was multiplied with E^3 to project out the steeply falling character. The "knee" can be seen at $E \simeq 4 \times 10^{15}$ eV, the "second knee" at $\simeq 3 \times 10^{17}$ eV, and the "ankle" at $E \simeq 5 \times 10^{18}$ eV

spectrum, which is referred to as a non-thermal behavior, since non-thermal processes are thought to be producing such spectra. Flux is usually expressed as the number of particles, coming in per area, per second, per solid angle in steradians (all sky is 4 π), and per energy interval. Cosmic rays have a spectrum near $E^{-2.7}$ up the the knee, at about 5×10^{15} eV, and then about $E^{-3.1}$ beyond, up the ankle, at about 3×10^{18} eV, beyond which the spectrum becomes hard to quantify, but can very approximately again be described by $E^{-2.7}$. We will refer to the range $E \geq 10^{18}$ as the Ultra High Energy (UHE) range. There is no other strong feature in the spectrum, especially no cutoff at the upper end. There is some limited evidence from the newest experiments (AGASA [10; 11; 12] and HiRes [15; 16]) for another feature, at about 3×10^{17} eV, called *the second knee*, where the spectrum appears to dip. Both the first and the second knee may be at an energy which is proportional to charge, i.e. at a constant Larmor radius, and therefore may imply a range in energies per particle. Figure 1.1 shows the overall cosmic ray spectrum.

The arrival directions of CR are quite isotropic. This feature is strongly

related to the interactions of CRs with the magnetic field of our galaxy of the order of 6×10^{-6} Gauss. More precisely one should note that there are two different components in the magnetic fields of our galaxy, a regular one and a turbulent one, see Ref. [18]. The strengths and directions of the magnetic fields belonging to the turbulent component are random [9; 18]. Due to this randomness, the trajectories of CR are randomly bent. As a consequence, the flux of CR which arrives on the Earth is also random or, more precisely, isotropic. However at a ceratin threshold, of the order of 10^{18}eV, CR have enough rigidity to escape the galaxy following trajectories which are almost straight lines. For this reason, the ultra high energy protons which reach the Earth should arrive along directions which are approximately parallel to the galactic plane. However, this conclusion is not confirmed by observations. Observations show in fact that the spatial distribution of ultra high energy protons is isotropic, so that their directions are not aligned with the galactic plane. This is of course a strong hint that UHECR are of extragalactic origin. This transition is believed however to cause a break in the energy spectrum that we observe in the ankle.

The energies of these cosmic ray particles, that we observe, range from a few hundred MeV to $\simeq 300\,\mathrm{EeV}$. The integral flux ranges from about 10^{-5} cm^{-2} s^{-1}, sr^{-1}, at 1 TeV per nucleus for protons, to 1 particle per steradian per km^2 and per century around 10^{20} eV, a decrease by a factor of 3×10^{19} in integral flux, and a corresponding decrease by a factor of 3×10^{27} in differential flux, i.e. per energy interval (see also Fig. 1.1). Electrons have only been measured to a few TeV.

The features of the "knees" are instead believed to originate from a change in chemical composition. The chemical composition is rather close to that of the interstellar medium, with a few strong peculiarities relative to that of the interstellar medium. Concerning the energy dependence towards the knee, and beyond, the fraction of heavy elements appears to continuously increase, with moderately to heavy elements almost certainly dominating beyond the knee [17], all the way to the ankle, where the composition seems to become light again [19; 20; 21]. This means, at that energy we observe a transition to what appears to be mostly Hydrogen and Helium nuclei. At much higher energies we can only show consistency with a continuation of these properties, we cannot prove unambiguously what the nature of these particles is.

Finally much uncertainty is around a possible end of the CR spectrum at the higher energies around 10^{20}eV. In fact, it has been noted that protons of energies above $5{\times}10^{19}$eV would lose their energy by interacting with the photons of the microwave background radiation. This effect was predicted in 1966, one year after the detection of the microwave background radiation, by Greisen [22], Kuzmin and Zatsepin [23](the GZK-effect). Protons with

energies above that threshold will be slowed down during their travel to the Earth by photo-pion production until their energy falls below the GZK-limit. This mechanism is so efficient that, in practice, protons with energies higher than 5×10^{19}eV should not be observed on the Earth if their source is located at distances which are greater than $\simeq$100 Mpc (see sec. 3.3.1). Experimentally, however, the cutoff has been both ruled out by AGASA [10] and confirmed by HiRes [24]. A final statement is expected from the AUGER observatory.

1.2 Interaction of CR with the Earth's atmosphere

Generalities

When CR arrive near the Earth, they hit the nuclei of the atoms of the atmosphere, in particular nitrogen and oxygen, producing in this way secondary particles. The first interaction of the CR primary particle takes place in the top 10% of the atmosphere [25]. The most relevant reactions, reminding that 90% or more of CR consists of protons, are:

$$pp \longrightarrow pn\pi^+ \qquad \text{or} \qquad pp \longrightarrow pp\pi^0 \tag{1.1}$$

$$pn \longrightarrow pp\pi^- \qquad \text{or} \qquad pn \longrightarrow pn\pi^0 \qquad \text{or} \qquad pn \longrightarrow nn\pi^+ \tag{1.2}$$

$$\tag{1.3}$$

though, one should remember that the collisions of CR with the atmosphere gives raise also to less relevant reactions, which produce particles like kaons, η particles and even resonances.

In the above reactions all the secondary particles are hadrons, namely protons p, neutrons n and pions in all their charged states $\pi^\pm, \pi^0$. Pions may in turn decay according to the following processes:

$$\pi^+ \longrightarrow \mu^+\nu_\mu \quad \text{and} \quad \pi^- \longrightarrow \mu^-\bar{\nu}_\mu \tag{1.4}$$

$$\pi^0 \longrightarrow \gamma\gamma \tag{1.5}$$

where the $\mu^\pm$'s are muons, the γ's are photons and $\nu_\mu, \bar{\nu}_\mu$ are respectively muonic neutrinos and their anti-particles. The mean life of pions is 26ns for $\pi^\pm$ and 10^{-16} seconds in the case of π^0. For this reason, charged pions may still collide with air atoms before decaying, but it is very unlikely that this happens in the case of neutral pions, which have a very short mean life. Other secondary particles, like protons, neutrons and photons interact very

frequently with the atoms of the atmosphere giving raise in this way to a cascade of less and less energetic secondary particles i.e. an *Extensive Air Shower* (EAS). At the end, these particles are stopped by the atmosphere or, if the energy of the primary particle was sufficiently high, they can reach the ground.

The main mechanism of energy loss of high energetic hadrons consists in the disintegration of the molecules of the atmosphere, see Fig 1.2. This leads to the creation of new particles through nuclear interactions like those shown in Eqs. (1.1) and (1.2). At lower energies, dissipative processes become dominant, in which the molecules of the atmosphere get either ionized or excited. The most relevant process of this kind in the case of heavy charged particles is the ionization of the molecules of the atmosphere. Lighter charged particles like electrons and positrons lose their energies not only by ionization, but also by bremsstrahlung. This consists in the radiative loss of energy of charged particles moving inside matter, when they are deflected by the electrostatic forces of the positive charged nuclei of the surrounding molecules.

The total number of secondary particles N_{sec} within the cascade grows rapidly, mainly sustained by the processes of bremsstrahlung and pair production due to electrons, positrons and photons. Hadrons like protons and, to a less extent, neutrons, are easily stopped by the atmosphere, so that they increase relevantly the number of particles by disintegrating the molecules of air only during the first stages of the formation of the cascade. The decays of pions given in Eqs. (1.4) and (1.5) produce muons and photons of considerable energies. The muons are very penetrating particles and do not interact very much with the air. They lose a small fraction of their energy before reaching the ground by ionizing the molecules of the atmosphere. The photons give raise instead to electron-positron pairs e^+e^-. In turn, electrons and positrons create other electrons by ionization or other photons due to bremsstrahlung. In this way, while the cascade propagates inside the atmosphere, the number of its electrons, positrons and photons grows almost exponentially. The maximum number of particles inside the cascade is attained when the average energy per electron reaches the threshold $E_T \sim$80MeV. When the energy of electrons in air falls below that threshold, ionization starts to prevail over bremsstrahlung as the main mechanism of energy loss of electrons in air and the process for increasing the number of particles described above ceases to be effective.

If the energy of the primary particle is below 10^{14}eV, essentially only the penetrating muons and neutrinos are able to arrive to the sea level, while the other particles in the cascade are absorbed at higher altitudes. Muons have a short mean life at rest (2.2ns), but since they travel at very high speeds, they manage to reach the surface of the Earth due to the relativistic boosting

of time. Part of these muons can still decay, giving raise to electrons e^- or positrons e^+, mainly according to the processes: $\mu^+ = e^+ + \nu_e + \bar{\nu}_\mu$ and $\mu^- = e^- + \bar{\nu}_e + \nu_\mu$.

When the energy of the primary particles is instead above 10^{14}eV, the cascade of secondary particles arrives to the ground before being stopped by the atmosphere creating an air shower, see Fig.1.2.

At sea level (atmospheric thickness of 1033 g/cm^2) the number of secondaries reaching ground level (with energies in excess of 200 keV) is about 3×10^{10} particles. 99% of these are photons and electrons/positrons in a ratio of 6 to 1. Their energy is mostly in the range 1 to 10 MeV and they transport 85% of the total energy. The remaining 1% is shared between mostly muons with an average energy of 1 GeV (and carrying about 10% of the total energy), pions of a few GeV (about 4% of the total energy) and, in smaller proportions, neutrinos and baryons. The lateral development of the shower is represented by its Molière radius (or the distance within which 90% of the total energy of the shower is contained) which, in the standard air is 70 m. However, the actual extension of the shower at ground level is of course much larger. As an example, at a distance of 1 km from the shower axis, the average densities of photons/electrons/muons are 30/2/1 per m^2. Usually the hadronic component, which is composed by heavier particles than those of the muon and electromagnetic components, is less deflected from the direction of the incident primary particle by the interactions with the atmosphere and it is thus concentrated in a narrow cone inside the air shower. The center of the cone is roughly aligned with the direction of the original primary particle. The maximum number of particles, i. e. the so-called point of shower maximum or simply shower maximum, is attained at an altitude of 2–3 km above the sea level.

Showers initiated by heavier nuclei can be described by making use of a superposition principle: a heavy nucleus of mass number A and energy E can be in a first approximation considered as a superposition of A showers initiated by nucleons each with an energy of E/A, therefore less penetrating than a nucleon with energy E (roughly 100 g/cm^2 higher in the atmosphere for iron).

High Energy behavior

At very high energies ($>10^{15}$eV) the physics of atmospheric showers is further complicate by the fact that the CM energy exceeds the range studied by Particle Accelerators and extrapolations have to be used while new effects starts to appear.

For a photon shower the proportion of muons will be even smaller and

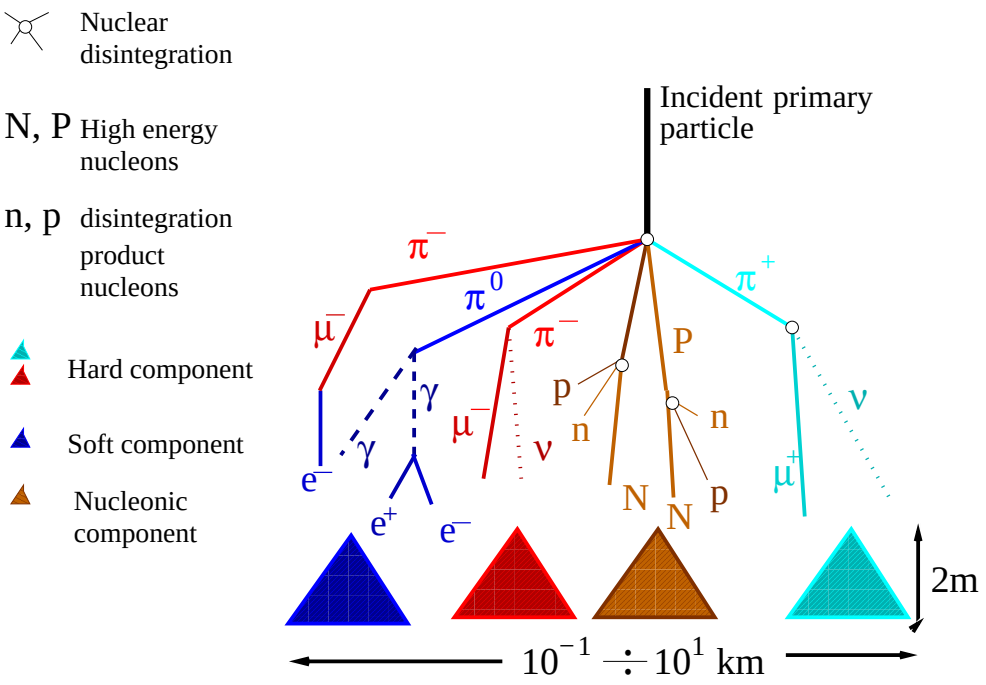

Figure 1.2: (From Ref.[8]) This figure illustrates schematically how air showers generate from cosmic rays. The high energetic primary particle, usually a proton, whose trajectory has been denoted in black, starts to interact with the molecules of the upper atmosphere. In this way, secondary particles are produced, which give raise to other particles (tertiary, quaternary etc.) via other interactions with the atmosphere or via decay processes. The total flux of particles can be divided in a *electromagnetic component* (photons, electrons and anti-electrons or positrons), see the blue trajectories in the figure, in a *muon component*, see the cyan and red trajectories, and finally in a *nucleonic component* (mainly protons, neutrons, rarely pions) denoted in brown. At the sea level, the air shower has the form of a pancake, whose height is around two meters, while its radius usually around a few hundreds of meters, but may reach some tents of kilometers in the case of very energetic cosmic rays. The nucleonic component is usually confined in a narrow cone centered along the direction of the incoming primary particle.

at the highest energies and another physical process will have important consequences on the EAS detection and characterization. This is the Landau-Pomeranchuk-Migdal (LPM) effect[26] which describes the decrease of the photon/electron nucleus cross-sections with energy and with the density of the medium with which they interact. Even in the upper atmosphere, the LPM effect becomes appreciable at energies in the EeV range so that it is possible for a photon of 100 EeV to develop an EAS very deep in the atmosphere, yielding less than 10^9 particles at ground level. Such a shower would have an extension of only a few km^2.

These effects are studied through heavy use of EAS Monte Carlo programs such as AIRES,[27] CORSIKA,[28] or MOCCA.[29] At the UHECR ranges, where the center-of-mass energies are much higher (almost two orders of magnitude) than those attainable in the future (and the most powerful) accelerator LHC, the correct modelling of the EAS in these programs becomes delicate. Some data are available from accelerator experiments such as HERA,[30] and showers of about 10^{16} eV are now being well studied through experiments such as KASCADE.[31] The models are thus constrained at lower energies and then extrapolated at higher ranges.

The most commonly used models for the high energy hadronic interactions of the simulation programs are SIBYLL [32], VENUS [33], QGSJet [34] and DPMJet [35]. Some detailed studies of the different models are available [36]. A clear conclusion is that the simulation results are never identical, even when the same theoretical models are used in different programs. However, when simulating a shower, these models are only used for the first few interactions and an EAS yields about 10^{10} or 10^{11} particles at ground level. Therefore the main shower parameters, such as the reconstructed direction and energy of the primary CR, are never strongly dependent on the chosen model. However, the identification of the primary is more problematic. Whatever technique is chosen the parameters used to identify the primary cosmic ray undergo large physical fluctuations which make an unambiguous identification difficult.

A complete analysis done by the KASCADE group on the hadronic core of EAS[31] has put some constraints on interaction models beyond accelerator energies. Various studies seem to indicate QGSJet as being the model which best reproduces the data[36; 37] with still some disagreement at the *knee* energies (10^{16} eV). For the highest energies, additional work (and data) is needed to improve the agreement between the available models.

1.3 The detection of the UHECR

When the cosmic ray flux becomes smaller than 1 particle per m^2 per year, satellite borne detectors are not appropriate any more. This happens above 10^{16} eV (the "knee" region). Then large surfaces are needed. The detectors then become ground-based and what they detect is not the incident particle itself but the cascade of secondary particles initiated by the cosmic ray interactions with the atmosphere (i.e. its EAS). The object of study is therefore this cascade.

Another distinction has to be made between the techniques used at lower and higher energies. Air showers can actually be observed at much lower energies than the knee region. Gamma ray astronomy, for example, uses the properties of the EAS (production of Cerenkov light by charged secondaries in the atmosphere) to detect and measure cosmic photons from a few tens of GeV up. We will discuss more extensively gamma detection in chapter 5. The main difference with the higher energies is that above a few hundreds of TeV and up to 10^{20} eV, cosmic rays are mainly charged particles which cannot be associated with a point source as is the case with photons. Therefore a ground-based cosmic ray detector must survey the whole sky and not point at a defined source.

There are two major techniques used in the detection of the highest energy cosmic rays. The first, and the most frequent, is to build an array of sensors (scintillators, water Cerenkov tanks, muon detectors) spread over a large area. The detectors count the particle densities at any given moment, thus sampling the EAS particles hitting the ground. The surface of the array is chosen in adequation with the incident flux and the energy range one wants to explore (large array surfaces for weak fluxes, large density of sensors for lower energies). From this sampling of the lateral development of the shower at a given atmospheric depth one can deduce the direction, the energy and possibly the identity of the primary CR. The second technique, until recently the exclusivity of the Fly's Eye (then HiRes) group, consists in studying the longitudinal development of the EAS by detecting the fluorescence light produced by the interactions of the the charged secondaries.

1.3.1 The optical fluorescence technique

The idea that one could use the fluorescence light produced in the atmosphere to detect and characterize the EAS was first suggested independently by Greisen and Suga [38] and then by a few other authors in the early sixties. The basic principle is simple [39] (although the detector itself and the mea-

suring techniques are quite sophisticated): the charged particles produced in the development of the EAS excite the nitrogen atoms of the atmosphere which then emit, very quickly and isotropically, fluorescence light which can be detected by a photo-multiplier. The emission efficiency (ratio of the energy emitted as fluorescence light to the deposited one) is poor (less than 1%), therefore observations can only be done on clear moonless nights (which results in an average 10% duty cycle) and low energy showers can hardly be observed. At higher energies, the huge number of particles in the shower produce enough light to be detected even at large distances. The fluorescence yield is 4 photons per electron per meter at ground level. The emitted light is typically in the 300-400 nm UV range to which the atmosphere is quite transparent. Under favorable atmospheric conditions an UHECR shower can be detected at distances as large as 20 km (about two attenuation lengths in a standard desert atmosphere at ground level).

The first successful detectors based on these ideas were built by a group of the University of Utah, under the name of "Fly's Eyes", and used with the Volcano Ranch ground array (see Section 1.3.3). A complete detector was then installed at Dugway (Utah) and started to take data in 1982. An updated version, the High-Resolution Fly's Eye, or HiRes, is presently running on this same site.

Figure 1.3 shows the geometry of the detection of an air shower by Fly's Eye type detectors (which are usually given the more generic name of "fluorescence detectors" or "fluorescence telescopes"). The detector sees the shower as a variable light bulb moving at the speed of light along the shower axis. A rough estimate of the equivalent radiated power would be $3E/EeV$ watts at the shower maximum, where E is the primary energy in EeV. The detector itself is a set of phototubes mounted on a "camera" set at the focal plane of a mirror. Each phototube sees a small portion of the sky (typically 1°). A fit on the pattern of tubes hit by the fluorescence photons determines with a precision better than one degree the plane containing the detector and the shower axis. In the *stereo mode* (EAS seen by

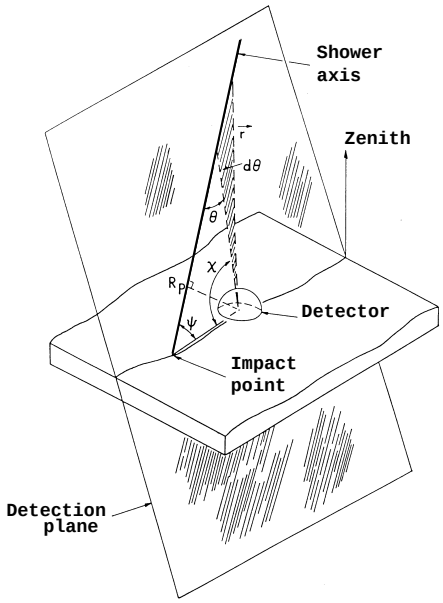

Figure 1.3: The principle of the detection of an EAS by a fluorescence telescope.[39]

two telescopes installed a few km apart), two planes are thus reconstructed and their intersection gives the incident direction with good precision. In the *mono mode* (EAS seen by a single telescope), one has to rely on the the time of arrival of the photons on the tubes. A good reconstruction of the direction (the Ψ angle) then needs a large number of pixels to be hit, enough to measure simultaneously the angular velocity and the angular acceleration of the shower development. Finally, in the *hybrid mode*, i.e. simultaneous detection of the EAS with a fluorescence telescope *and* a ground array, the knowledge of the intersection of the shower axis with the array plane (reconstructed by the array) allows the selection of the right direction in the family of lines in the detector-shower axis plane. For 100 EeV showers, a precision of 0.2° can then be reached.

The fluorescence technique is the most appropriate way to measure the energy of the incident cosmic ray: it is a partial calorimetric measurement with continuous longitudinal sampling. The amount of fluorescence light emitted is proportional to the number of charged particles in the shower. The EAS has a longitudinal development usually parameterized by the analytic Gaisser-Hillas function giving the size N_{e} of the shower (actually the number of the ionizing electrons) as a function of atmospheric depth x:

$$N_{\mathrm{e}}(x) = N_{\max} \left(\frac{x - x_0}{X_{\max} - x_0} \right)^{(X_{\max} - x_0)/\lambda} \mathrm{e}^{(X_{\max} - x)/\lambda}$$

where $\lambda = 70\,\mathrm{g/cm^2}$, x_0 is the depth at which the first interaction occurs, and $X_{\max}$ the position of the shower maximum. The total energy of the shower is proportional to the integral of this function, knowing that the average energy loss per particle is 2.2 MeV/g cm^{-2}.

In practice several effects have to be taken into account to properly convert the detected fluorescence signal into the primary CR energy. These include the subtraction of the direct or diffused Cerenkov light, the (wavelength dependent) Rayleigh and Mie (aerosol) scatterings, the dependence of the attenuation on altitude (and elevation for a given altitude) and atmospheric conditions, the energy transported by the neutral particles (neutrinos), the hadrons interacting with nuclei (whose energy is not converted into fluorescence) and penetrating muons whose energy is mostly dumped into the earth. One also has to take into account that a shower is never seen in its totality by a fluorescence telescope: the Gaisser-Hillas function parameters are measured by a fit to the visible part of the shower, usually cut at the beginning (interaction point) and the end (tail absorbed by the earth). All these effects contribute to the systematic errors in the energy measurement which needs sophisticated monitoring and calibration techniques, e.g the use of powerful

laser beams shot through the atmosphere. The overall energy resolution one can reach with a fluorescence telescope is of course dependent on the EAS energy but also on the detection mode (mono, stereo or hybrid). The HiRes detector should have a resolution of 25% or better above 30 EeV in the *mono* mode. This improves significantly in the stereo or hybrid modes (about 3% *median* relative error at the same energy in the latter case).

1.3.2 The ground array technique

A ground array is a set of particle detectors distributed as a more or less regular matrix over some surface. The surface of the array is a direct function of the expected incident flux and of the statistics needed to answer the questions at hand. The 100 km^2 AGASA array is appropriate to confirm the existence of the UHECR with energies in excess of 100 EeV (which it detects at a rate of about one event per year). To explore the properties of these cosmic rays and hopefully answer the open question of their origin, the relevant detector will no doubt be the Auger Observatory with its 6000 km^2 surface over two sites.

The array detectors count the number of secondary particles which cross them as a function of time. Therefore, they sample the non-absorbed part of the shower which reaches the ground. The incident CR's direction and energy are measured by assuming that the shower has an axial symmetry. This assumption is valid for not too large zenith angles (usually $\theta < 60°$). At larger angles the low energy secondaries are deflected by the geomagnetic fields and the analysis becomes more delicate.

The direction of the shower axis (hence of the incident CR) is reconstructed by fitting an analytical function (the "lateral distribution function" or LDF) to the measured densities. The LDF explicit form depends on each experiment.

Once the zenith angle correction is made for the LDF, an estimator of the primary CR energy is extracted from this function. At energies below 10 EeV, this estimator is usually taken as the particle density (whatever particles detected by the array stations) at 600 m from the shower core, ρ_{600}. The density at 600 m is chosen for the following reason. Because of variations on the primary interaction point (and the position of the shower maximum), there are large fluctuations in the ground densities close to the core. At the same time, the statistical fluctuations in the measured densities are important at large distances where the densities are low. Monte Carlo studies show that somewhere in between, the overall fluctuation reaches a minimum. This happens to be at 600 m from the core, a value slowly increasing when one goes to the highest energies. In the UHECR range, a more appropriate density is

ρ_{1000}. Once this value is determined, the primary energy is related to it by a quasi-linear relation:

$$E = k\rho_{600}^{\alpha}$$

where α is a parameter close to 1. Of course, to be able to reconstruct the LDF, many array stations have to be hit at the same time by a shower. The spacing between the stations determines the threshold energy for a vertical shower: the 500 m spacing of the Haverah Park triggering stations corresponds to a threshold of a few 10^{16} eV, while the 1.5 km separation of the Auger Observatory stations makes this array almost 100% efficient for energies above 10 EeV.

1.3.3 Past and present detectors

The EAS detection performance of a ground based detector is given by its *acceptance* (or *aperture*) $\mathcal{A}$. For detectors large enough so that boundary effects can be neglected, it is assumed that at a given energy an EAS is detected whenever the shower axis hits the ground within an area S (for most cases the surface covered by the ground array) and with a zenith angle having a value between 0 (vertical showers) and a maximum $\theta_{\max}$, usually about 60°. The total geometrical aperture is then: $\mathcal{A} = S \cdot f_{\rm dc} \cdot \int_0^{\theta_{\max}} \cos\theta d\Omega = \pi S \sin^2\theta_{\max}$ usually given in km^{2}sr units. The factor $f_{\rm dc}$ takes into account the duty cycle of the experiment, of order ~ 0.1 for an optical detector and $\sim$1 for a ground array.

The detectors that have contributed to the study of UHECRs are listed below, with their total exposures in the relevant energy range [4].

- **Volcano Ranch**[40] (New Mexico, USA). This is the first detector claiming to have detected a $> 10^{20}$eV event in February 1962. It was an array of 3 m^2 scintillator counters with a spacing of 900 m and a total area of about 8 km^2. The detector's total exposure was estimated to be of the order of 60 km^2 sr year.

- **Haverah Park**[41] (Great-Britain), an array of water Cerenkov tanks of various sizes and spacings covering an area of 12 km^2. The detector took data during almost 20 years (1968-1987) with a total exposure of 270 km^2 sr year. It reported $4 > 10^{20}$eV events.

- **SUGAR**[42] *Sidney University Giant Air-Shower Recorder* (Australia, $1968 - 1979$). This experiment was made of 54 pairs of buried scintillators spaced each other by 50 m, for a total area covered of 100 km^2. Until recently it has been the only giant detector for EAS in the southern hemisphere.

- **Fly's Eye**[19; 20](Utah, USA), a binocular system of fluorescence telescopes. It is now being replaced by HiRes, a new generation fluorescence detector of larger aperture on the same site. Its total exposure is estimated at about 600 km^2 sr year in the mono-mode (an EAS detected only by one of the two telescopes) and 170 in the stereo-mode. The Fly's Eye detected the most energetic particle ever (320 EeV), but unfortunately in the mono-mode, hence with relatively large errors on the measurements of the incident direction and energy.

- **AGASA**[11](Akeno, Japan), the largest, before AUGER, ground array in the world. It was composed of 111 scintillator counters (2.2 m^2 surface and almost 1 km spacing) over an area of 100 km^2, with also 27 muon counters. AGASA has taken data from 1990 to 2003, with a total exposure of 670 km^2 sr year. The inner AKENO core was instrumented for the observation of lower energy events.

- **Yakutsk**[43](Russia, 1974, present) This experiment was a pioneer in the test of multi-instrument approach to EAS detection. It consists of a combination of scintillators, muon and air-Cerenkov detectors with a total covered area of about 12 km^2.

- **HiRes**[15] The "High Resolution Fly's Eye" or HiRes is an improved version of the original Fly's Eye detector. The present version of the detector design consists of two "Eyes" separated by 13 km, situated at a military site in Dugway (Utah, USA). The basic fluorescence telescope of HiRes is a mirror equipped with a camera of 256 phototubes, each phototube (pixel) watching an angular region of space of $1^\circ \times 1^\circ$. Therefore, each telescope has a field of view of $16^\circ \times 16^\circ$, and a complete eye is expected to cover a field of 30° in elevation and 360° in azimuth with 44 telescopes. Its aperture is about 350 km^2 sr at 10 EeV and about 1000 km^2 sr at 100 EeV. This gives a detection rate (based on the empirical formula, see above) of about 10 events/year above 100 EeV. The HiRes detector's optimal operating range is therefore the decade between 5 and 50 EeV.

Among the previously mentioned experiments, only HiRes and Yakutsk are still taking data, though the latter has been "down-graded" to study a lower energy region. The solution to many unanswered questions in UHECRs should come with two experiments of the next generation:

- **Auger**[44] The Auger Observatory is a detector whose design is based on the "hybrid" detection mode (EAS simultaneously observed by a ground array and a fluorescence detector).

The Observatory whose construction started during the fall of 1999, once completed, will be covering two sites, respectively in the southern (Pampa Amarilla, province of Mendoza, Argentina) and northern (Colorado, USA) hemispheres. The southern hemisphere detector is especially interesting since very few detectors took data in the past in this part of the world from where the direction of the center of our galaxy is visible.

The size of the ground array is adapted to its physics aims: explore the spectrum around and above the GZK cutoff. Therefore the surface of each site was chosen to be of 3000 km^2, so as to provide a statistics of a few tens of expected events per year above 100 EeV. The detector is designed to be fully efficient for showers with energies of 10 EeV and above, with a duty-cycle of 100%. This will make the link with the part of the energy spectrum well explored by AGASA and HiRes. The energy threshold defines the spacing of the detector "stations": with a spacing of 1.5 km between the stations, a 10 EeV vertical shower will hit on average 6 stations which is enough to fully reconstruct the EAS. With such a spacing on a regular grid, the total number of stations is about 1600. Each station is a cylindrical tank (the same basic design as the Haverah Park array, but with much more sophisticated electronics), of 10 m^2 surface and 1.2 m height. The tanks are filled with filtered water in which the secondary particles from the EAS produce light by Cerenkov radiation.

Because of the size of the array, the stations have to work in a stand-alone mode: they are powered by solar panels and batteries, and the communication with the central station where the data-taking system is installed is done by telecommunication techniques. The giant array is completed by an optical device detecting the fluorescence light produced in the EAS. Each telescope sees an angle of about 30×30 degrees. On the southern site, 24 telescopes are planned grouped in 4 stations of 6 telescopes each with a field of view of 180 degrees. In the hybrid mode (10% of the events), the detector is expected to have on average 10% energy resolution and an angular precision of about 0.3°. For the array alone those numbers become 20% and less than 1°. The statistics attainable with such a detector is dependent on what exactly will happen above the GZK cutoff. However, with its total aperture of 14000 km^2sr (both sites), the Auger Observatory should detect of the order of 6000 events above 10 EeV and 60 above 100 EeV per year.

- **Telescope Array**[45] The Telescope Array(TA) is a joint Japanese-

American project of a purely optical detector which, in its initial design, aims to be used as a gamma-astronomy device as well as a fluorescence detector. Its basic principles are identical to the HiRes technique. The individual telescopes are made of 3 meter diameter segmented mirrors with a camera of 256 pixels. Each pixel (hexagonal phototubes) sees a patch of sky in a solid angle of $1^\circ \times 1^\circ$ (hence a field-of-view of $16^\circ \times 16^\circ$ per telescope). One TA station is made of 42 telescopes, thus viewing the sky over 2π in azimuth and 30° in elevation. The experiment site is in Utah, near the actual HiRes Site and the Panned Auger Noth. The total aperture of the array should be about 5 times the HiRes acceptance, depending on the spacing of the stations and the performance of the pixels.

1.4 Chemical composition

The identification of the primary cosmic ray with a fluorescence telescope is based on the shower maximum in the atmosphere ($X_{\max}$) which depends on the nature and the energy of the incident cosmic ray. At a given energy, and on the average, a shower generated by a heavy nucleus reaches its maximum higher in the atmosphere than that of a light nucleus or a proton. Simulations show typical values of (respectively for iron nuclei and protons) 750 and 850 g/cm^2. Unfortunately, physical fluctuations of the interaction point and of the shower development (larger than the precision on the shower reconstruction) blur this ideal image. As an example, at 10 EeV the typical fluctuation on the $X_{\max}$ position is 50 g/cm^2. Thus, when the fluorescence technique is used alone, it is practically impossible to define the primary composition on a shower-by-shower basis. Therefore, one must look for statistical means of studying the chemical composition and/or use the hybrid detection method where a multi-variable analysis becomes possible.

The former method uses the so-called *elongation rate* measured for a sample of showers within some energy range. The depth of the shower maximum as a function of the energy for a given composition is given by [46]:

$$X_{\max} = D_{\mathrm{el}} \ln\left(\frac{E}{E_0}\right)$$

where E_0 is a parameter depending on the primary nucleus mass. Therefore, incident samples of pure composition will be displayed as parallel straight lines with the same slope D_{el} (the *elongation rate*) on a semi-logarithmic diagram.

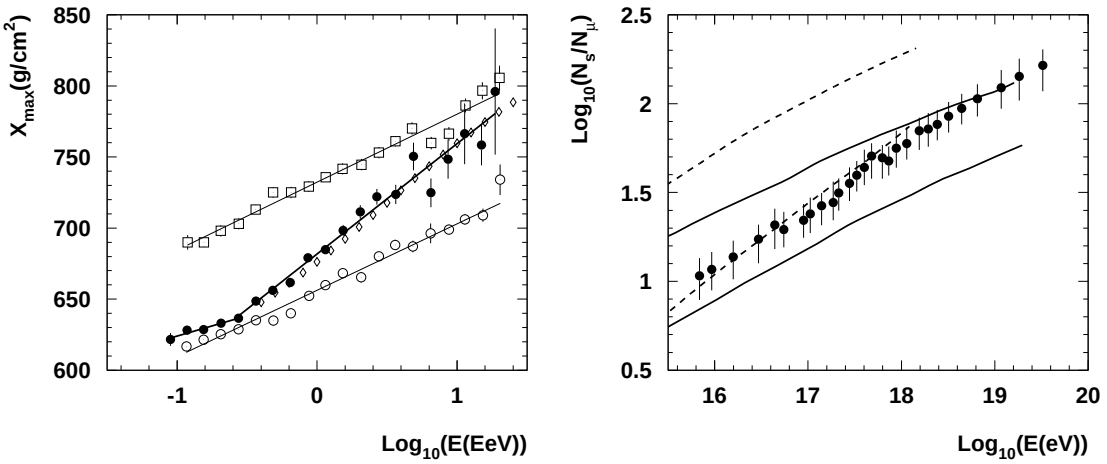

Figure 1.4: Left: the X_{max} elongation rate. Black dots: Fly's Eye data. Open squares : proton X_{max} distribution based on the KNP model. Open circles: iron X_{max} distribution based on the KNP model. Diamonds: expected mean X_{max} distribution based on a simple two component model. Right: the ratio of charged particle size to muon size (muon threshold 1 GeV) as a function of the primary energy from the Yakutsk experiment. Solid lines are the Monte Carlo predictions of the QGS model (Upper curve: proton, lower curve: iron). Dashed lines are the Monte Carlo predictions of a scaling model(Upper curve: proton, lower curve: iron). (From Ref.[6])

A ground array makes use of two main effects to separate heavy from light nuclei (and from photons): the proportion of muons compared to the electromagnetic component of the shower and the rise time of the detected signal. Both parameters are due to the way the muons are produced during the shower development. The muons in a shower come from the decay of charged pions when they reach an energy low enough so that their decay length becomes smaller than their interaction length. Since this happens earlier in the case of a primary heavy nucleus, the resulting shower is richer in muons than a proton shower. At the same time, and since muons are produced earlier in the shower development, they reach the ground also earlier, compared to the electromagnetic component which undergoes many interactions before reaching the detector array.

One must keep in mind that observables contributing to the identification (depth of the shower maximum, muon to electron-photon ratio in the EAS at a given depth, position of the first interaction...) are subject to large fluctuations and each identity signature includes an unavoidable background. Therefore, the UHECR chemical composition is very likely to be unveiled only on a statistical basis, and by cross-checking the information deduced from as large a number of parameters as possible.

- **Composition from X_{max} measurements**

  The Fly's Eye group derive their composition estimate by comparing the measurements with Monte Carlo predictions. The Monte Carlo showers are generated using a QCD Pomeron model (the so-called KNP model) [47; 48]. The Monte Carlo generated showers are then passed through the detector Monte Carlo simulation program to account for detector trigger biases. Those events triggering both Fly's Eye sites in the detector Monte Carlo are written to a data file with the same format as the real data. This fake data set is then reconstructed using the same programs used in the real data analysis.

  The mean X_{max} as a function of primary energy measured by the Fly's Eye detectors, is shown in Fig.1.4(a) together with the model Monte Carlo generated proton and iron showers. From the figure, one can see that the composition is heavy at a few times 10^{17} eV and gradually shifts to light primaries near 10^{19}eV. The same conclusion is reached by comparing the rise and fall of the full X_{max} distributions in each energy bin [49]. The elongation rate (the increment of X_{max} per decade of energy) from 0.3 EeV to 10 EeV is $78.9\pm3 g/cm^2$ per decade for the real data, and 50 g/cm^2 per decade for the Monte Carlo simulated proton or iron showers.

  Constraints on hadronic interaction models by the Fly's Eye measurements arise from the fact that the Fly's Eye measures both the absolute X_{max} position at each energy and the elongation rate. The absolute mean value of X_{max} around 3×10^{17} eV (about $630 g/cm^2$) essentially rejects any model with a large elongation rate, since those large elongation rate models inevitably predict a deeper X_{max} at 3×10^{17} eV, even with an iron primary.

  The facts that the measured absolute value of X_{max} at 3×10^{17} eV is low and that the measured elongation rate is high, naturally leads to the conclusion that the composition is becoming lighter over the energy range observed. Of course, a quantitative prediction of how quickly the composition gets lighter is still model dependent.

- **Composition from muon to electron ratio**

  In addition to the Cherenkov lateral distribution, the Yakutsk group also measured muon densities. The all charged particle size is plotted against muon size in Fig.1.4(b). Two model predictions are plotted in the same figure, one uses the QGS model [50], and the other uses an old-fashioned scaling model[51]. It is interesting to note that the QGS

model predicts a charged particle to muon ratio which is more than a factor of two smaller than the scaling model prediction at energies above 10^{18} eV. The Yakutsk group reach the same conclusion as the Fly's Eye about the composition as their X_{max} result, if the QGS model is used to interpret the data. On the other hand, the scaling model predicts fewer muons, and prefers a flux of almost 100% iron below 10^{18} eV before running into difficulty above 10^{18}eV where a composition heavier than iron is required.

The AGASA experiment has measured the muon density as a function of the primary energy of cosmic rays or rather as function of S600, their observable energy estimator.

The AGASA group based their primary identification on the muon content of the EAS at ground level,[52] an essentially independent method. Showers initiated by heavier nuclei are expected to have a higher muon content than light nuclei or protons, the gamma showers being the poorest in muons. Initially the conclusion of the AGASA experiment was quite opposite to the Fly's Eye: no change in chemical composition. However a critical review of both methods[53] showed that the inconsistencies were mainly due to the scaling assumption of the interaction model used by the AGASA group. The authors concluded that if a model with a higher (compared to the one given by scaling) rate of energy dissipation at high energy is assumed, as indicated by the direct $X_{\max}$ measurements of the Fly's Eye, both data sets demonstrate a change of composition, a shift from heavy (iron) at 0.1 EeV to light (proton) at 10 EeV. Different interaction models as long as they go beyond scaling, would lead to the same qualitative result but eventually with a different rate of change.

It is clear, that better measurements and a further refinement of interaction models are necessary to resolve the composition issue. Gamma rays have also high cross sections with air and are still another possible candidate for UHECR but no evidence were found up to now for a gamma signature among the highest energy events. The most energetic Fly's Eye event was studied in detail [54] and found incompatible with an electromagnetic shower. Both interpretations of the AGASA and the Fly's Eye data favor a hadronic origin. Finally, it is worth mentioning that UHE neutrinos may also be detected by their EAS. This is important because the detection of neutrinos (together with an important component of photons) in the higher energy range of the spectrum would be a solid signature of the top-down mechanisms (see Section 1.5.3). However neutrino EAS will hardly be distinguishable from an

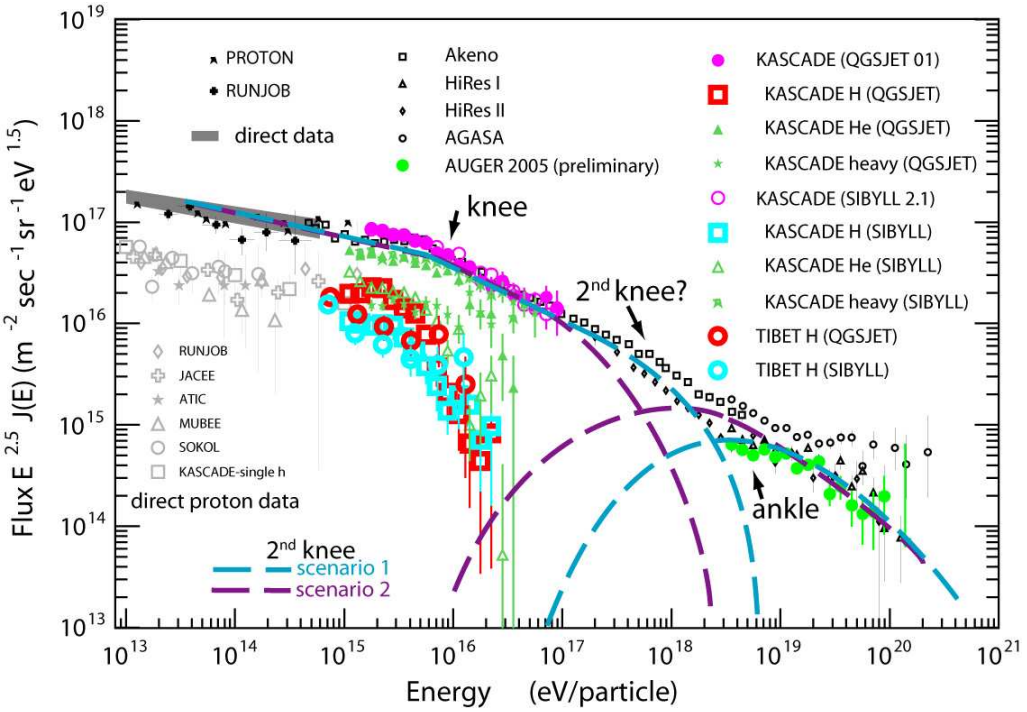

Figure 1.5: Primary cosmic ray flux [57]. Results of some experiments for the all-particle spectrum as well as for spectra of individual mass groups, in particular for protons. Possible scenarios for the origin of a second knee are also shown.

hadronic shower; an alternative and promising way of detecting ultra-high energy neutrinos would be to use horizontal air showers [55], i.e. showers generated by cosmic rays with incident zenith angles larger than 60°. In any case, for neutrinos the interaction should occur uniformly in atmospheric depth, a feature which is not reproduced by the current data. While neutrinos may very well be one of the components of the high energy end of the cosmic ray spectrum and prove to be an unambiguous signature of the new physics underlying the production mechanisms (see below) they do not seem to dominate the observations at least up to energies of a few 10^{20} eV.

Finally, it is worth describing some results in the energy range below the ankle where a satisfactory scenario is reached by assuming standard astrophysical acceleration in supernova remnants. The most interesting results in analyzing EAS in the knee region are originating from the KASCADE experiment, where the data analyses aim to reconstruct the energy spectra of individual mass groups, taking into account not only different shower observables (muon and electron shower sizes), but also their correlations on an event-by-event basis. By applying unfolding procedures (based on Monte-Carlo simulations using different hadronic interaction models) to the exper-

imental data individual energy spectra are obtained as displayed in Fig. 1.5. A knee like feature is clearly visible in the all particle spectrum, which is the sum of the unfolded single mass group spectra, as well as in the spectra of primary proton and helium. KASCADE claims that the elemental composition of cosmic rays is dominated by the light components below the knee and by a heavy component above the knee feature [56]. Some other results are reviewed in ref. [57].

1.5 Possible sources of the UHECR and Acceleration Mechanisms

Today's understanding of the phenomena responsible for the production of UHERC, i.e. the transfer of macroscopic amounts of energy to microscopic particles, is still limited. One distinguishes two classes of processes: the so called "Top-Down" and "Bottom-Up" scenarios. In the former, the cosmic ray is one of the stable decay products of a super-massive particle. Such particles with masses exceeding 1 ZeV can either be meta-stable relics of some primordial field or highly unstable particles produced by the radiation, interaction or collapse of topological defects. Those processes are briefly reviewed in Section 1.5.3.

In the second scenario discussed in section 1.5.2 the energy is transferred to the cosmic rays through their interaction with electromagnetic fields. This classical approach does not require new physics as opposed to the "Top-Down" mechanism, but does not exclude it either since, in some models, the accelerated particle - the cosmic ray - is itself "exotic".

Once accelerated the cosmic rays must propagate from their source to the observer. At energies above 10 EeV and except for neutrinos, the Universe is not transparent to ordinary stable particles on scales much larger than about 10 Mpc. Regardless of their nature, cosmic rays lose energy in their interaction with the various photon backgrounds, dominantly the copious Cosmic Microwave Background (CMB) but also the Infra-Red/Optical (IR/O) and the Radio backgrounds. The GZK cutoff puts severe constraints on the distance that a cosmic ray can travel before losing most of its energy or being absorbed. The absence of prominent visible astrophysical objects in the direction of the observed highest energy cosmic rays together with this distance cutoff adds even more constraints on the "classical" Bottom-Up picture.

For a more detailed review we address to the report by P.Bhattacharjee and G.Sigl [58] and the references therein.

1.5.1 Particle Propagation and the GZK cutoff

We will focus here on the propagation of atomic nuclei (in particular protons) and photons. Electrons are not considered as potential UHECR because they radiate most of their energy while crossing the cosmic magnetic fields. Among the known stable particles, and within the framework of the Standard Model, those are the only possible candidates for UHECR. As we mentioned in Section 1.4, the actual data effectively favor a hadronic composition.

Soon after the discovery of the cosmic background radiation by Penzias and Wilson (1965), Greisen [22] and Zatsepin and Kuzmin [23] predicted that there would be a cutoff in the spectrum of protons around 6×10^{19} eV due to photopion production on the microwave background. This has become known as the GZK cutoff.

The principal reactions of protons p with background photons ($\gamma_{2.7K}$) are

$$\begin{aligned} p + \gamma_{2.7K} &\longrightarrow n + \pi^+ && (1.6)\\ &\longrightarrow p + \pi^0 \\ &\longrightarrow p + e^+ + e^-. && (1.7) \end{aligned}$$

The dominant background photons are microwaves, which have a peak energy of 6×10^{-4} eV and a photon density of about 400 per cm^3. Though the threshold energy for pair production [Eq. (1.7)] is about 10^{18} eV and the mean free path is $\sim$ 1 Mpc, compared to $10^{19.6}$ eV and $\sim$ 6 Mpc for pion production [Eq. (1.6)], the energy loss, per interaction, for pair production is only 0.1% compared to 20% for pion production. Thus the process is less significant than the photo-pion production.

A cutoff in the spectrum is predicted around several times 10^{19} eV if the primary cosmic-ray energy spectrum extends beyond 10^{20} eV and the sources are distributed uniformly throughout the universe, so that above the cutoff only sources not far that $\sim$100 Mpc can be seen at Earth. More details on protons propagation is given in Sec.3.3.1.

In the case of heavy nuclei of mass A, photodisintegration and pairproduction processes are important:

$$\begin{aligned} A + \gamma_{2.7K} &\longrightarrow (A-1) + N && (1.8)\\ &\longrightarrow (A-2) + 2N \\ &\longrightarrow A + e^+ + e^-. && (1.9) \end{aligned}$$

where N is a nucleon (proton or neutron). The main channels are (γ, n) and (γ, p). The energy-loss rate through double-nucleon emission such as $(\gamma, 2n)$, (γ, np), or $(\gamma, 2p)$ is about one order of magnitude lower than that

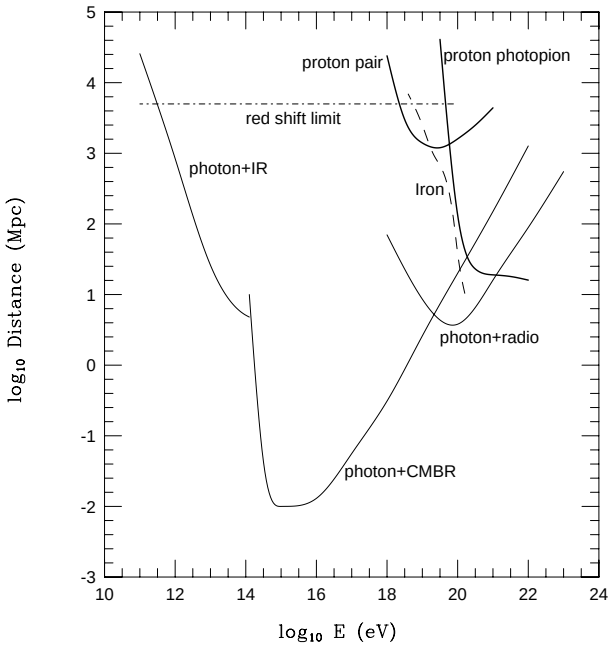

Figure 1.6: Attenuation length of photons, protons and iron in various background radiations as a function of energy.[4] The dot-dashed line represents the absolute upper limit on the distance a particle can travel toward Earth, regardless of its initial energy.

through single-nucleon emission. The energy loss due to IR photons is only effective below 5×10^{19} eV, while energy loss in interactions with microwave background photons is most significant for energies above 2×10^{20} eV [59]. Though a nucleus does not disintegrate through pair creation, it loses energy and there is an effect on the rate of energy loss, most notably in the region between 5×10^{19} and 2×10^{20} eV.

In the case of gamma rays, pair creation through interaction with the cosmic background radiation is most important in a wide energy range above the threshold of 4×10^{14} eV,

$$\gamma + \gamma_{2.7K} \longrightarrow e^+ + e^-. \tag{1.10}$$

It should be noted that attenuation due to pair creation on diffuse background radio photons becomes dominant over microwave effects above 2×10^{19} eV. The propagation of photon through the intergalactic medium will be discussed more extensively in chapter 6. The attenuation length for photons proton and nuclei is shown in Figure 1.6.

1.5.2 Conventional acceleration: Bottom-Up scenarios

One essentially distinguishes two types of acceleration mechanisms:

- Direct, one-shot acceleration by very high electric fields. This occurs in or near very compact objects such as highly magnetized neutron stars or the accretion disks of black holes. However, this type of mechanism does not naturally provide a power-law spectrum.

- Diffusive, stochastic shock acceleration in magnetized plasma clouds which generally occurs in all systems where shock waves are present such as supernova remnants or radio galaxy hot spots. This statistical acceleration is known as the Fermi mechanism of first (or second) order, depending on whether the energy gain is proportional to the first (or second) power of β, the shock velocity.

Extensive reviews of acceleration mechanisms exist in the literature, e.g. on acceleration by neutron stars [60], shock acceleration and propagation [61], non relativistic shocks [62], and relativistic shocks [63].

Hillas has shown [64] that irrespective of the details of the acceleration mechanisms, the maximum energy of a particle of charge Ze within a given site of size R is:

$$E_{\max} \approx \beta Z \left(\frac{B}{1\,\mu\mathrm{G}}\right)\left(\frac{R}{1\,\mathrm{kpc}}\right) 10^{18}\ \mathrm{eV} \tag{1.11}$$

where B is the magnetic field inside the acceleration volume and β the velocity of the shock wave or the efficiency of the acceleration mechanism. This condition essentially states that the Larmor radius of the accelerated particle must be smaller than the size of the acceleration region, and is nicely represented in the Hillas diagram shown in Figure 1.7.

Inspecting the Hillas diagram one sees that only a few astrophysical sources satisfy the necessary, but not sufficient, condition given by Eq. (1.11). Among the possible candidates we find, pulsars, Active Galactic Nuclei (AGN) and Fanaroff-Riley Class II (FR-II) radio galaxies. Some of them are reviewed e.g. by Biermann [7].

1.5.3 "Exotic" sources: Top-Down scenario

One way to overcome the many problems related to the acceleration of UHECR, their flux, the visibility of their sources and so on, is to introduce a new unstable or meta-stable super-massive particle, currently called the X-particle. The decay of the X-particle produces, among other things,

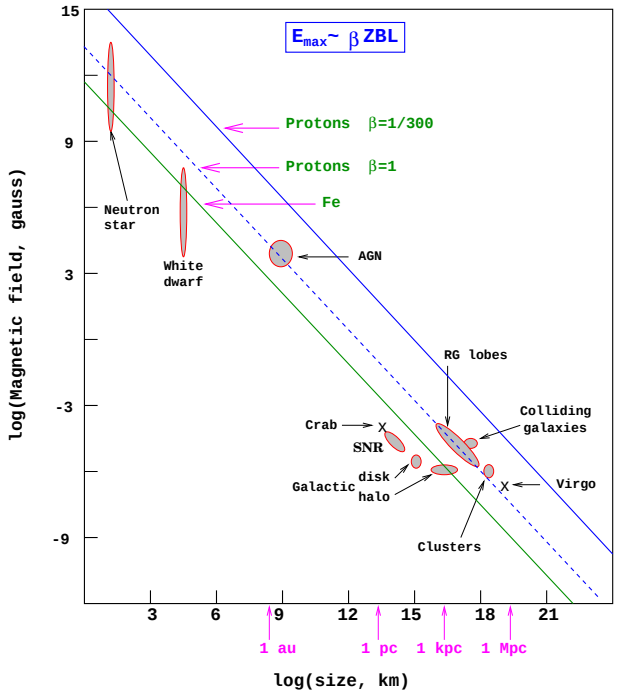

Figure 1.7: Size and magnetic field strength of possible acceleration sites [5]. Objects below the diagonal lines cannot accelerate the corresponding elements (Iron with $\beta = 1$ or protons $\beta = 1$ and $\beta = 1/300$) above 10^{20} eV.

quarks and leptons. The quarks hadronize, producing jets of hadrons which, together with the decay products of the unstable leptons, result in a large cascade of energetic photons, neutrinos and light leptons with a small fraction of protons and neutrons, part of which become the UHECR.

For this scenario to be observable three conditions must be met:

- The decay must have occurred recently since the decay products must have traveled less than about 100 Mpc because of the attenuation processes discussed above.

- The mass of this new particle must be well above the observed highest energy (100 EeV range), a hypothesis well satisfied by Grand Unification Theories (GUT) whose scale is around 10^{24}-10^{25} eV.

- The ratio of the volume density of this particle to its decay time must be compatible with the observed flux of UHECR.

The X-particles may be produced by way of two distinct mechanisms:

- Radiation, interaction or collapse of Topological Defects (TD), producing X-particles that decay instantly. In those models the TD are leftovers from the GUT symmetry breaking phase transition in the very early universe. However very little is known on the phase transition itself and on the TD density that survives a possible inflationary phase, and quantitative predictions are usually quite difficult to rely on.

- Super-massive metastable relic particles from some primordial quantum field, produced after the now commonly accepted inflationary stage of our Universe. Lifetime of those relics should be of the order of the age of the universe and must be guaranteed by some almost conserved protecting symmetry. It is worth noting that in some of those scenarios the relic particles may also act as non-thermal Dark Matter.

In the first case the X-particles instantly decay and the flux of UHECR is related to their production rate given by the density of TD and their radiation, collapse or interaction rate, while in the second case the flux is driven by the ratio of the density of the relics over their lifetime.

More about X-particles

Topological defects
There is a very wide variety of topological defect models. Many authors have addressed this field. Among them we cite Vilenkin and Shellard [66] and Vachaspati [67; 68] for a review on TD formation and interaction, and Bhattacharjee [69], Bhattacharjee and Sigl [58] and Berezinky, Blasi and Vilenkin [70] for a review on experimental signatures in the framework of the UHECR.

According to the current picture on the evolution of the Universe, several symmetry breaking phase transitions such as $GUT \Longrightarrow H \ ... \Longrightarrow SU(3) \times SU(2) \times U(1)$ occurred during the cooling. For those "spontaneous" symmetry breakings to occur, some scalar field (called the Higgs field) must acquire a non vanishing expectation value in the new vacuum (ground) state. Quanta associated to those fields have energies of the order of the symmetry breaking scale, e.g. $10^{15} - 10^{16}$ GeV for the Grand Unification scale. Such values are indeed perfectly in the range of interest for the above mentioned X-particles.

During the phase transition process, non causal regions may evolve towards different states in such a way that at the different domain borders, the Higgs field keeps a null expectation value. Energy is then trapped in a TD whose properties depend on the topology of the manifold where the Higgs potential reaches its minimum (the vacuum manifold topology).

Possible TDs are classified according to their dimensions: magnetic monopoles (0-dimensional, point-like); cosmic strings (1-dimensional); a subvariety of the previous which carries current and is supra-conducting; domain walls (2-dimensional); textures (3-dimensional). Among those, only monopoles and cosmic strings are of interest as possible UHECR sources: textures do not trap energy while domain walls, if they existed, would overclose the Universe [71].

Supermassive relics
Supermassive relic particles may be another possible source of UHECR.[72] Their mass should be larger than 10^{12} GeV and their lifetime of the order of the age of the Universe since these relics must decay now (close by) in order to explain the UHECR flux. Unlike strings and monopoles, but like monopolonia, relics aggregate under the effect of gravity like ordinary matter and act as a (non thermal) cold dark matter component. The distribution of such relics should consequently be biased towards galaxies and galaxy clusters. A high statistics study of the UHECR arrival distributions will be a very powerful tool to distinguish between aggregating and non-aggregating Top-Down sources.

1.6 Distribution of the sources

A necessary ingredient in the search for the origin of the UHECR is to locate their sources. This is done by reconstructing the incident cosmic ray's direction and checking if the data show images of point sources or correlations with distributions of astrophysical objects in our vicinity. Since a likely possibility as for the nature of the UHECR is that they are protons, we will say a some words about what we know of the galactic and extragalactic magnetic fields: this will show that for supra-GZK energies, proton astronomy is possible to some extent.

1.6.1 Magnetic fields

There are a limited number of methods to study the magnetic fields on galactic or extragalactic scales [73]. One is the measure of the Zeeman splitting of radio or maser lines in the interstellar gas. This method informs us mainly on the galactic magnetic fields, as extragalactic signals suffer Doppler smearing while the field values are at least three orders of magnitude below the galactic ones. The magnetic field structure of the galactic disc is therefore thought to be rather well understood. One of the parametrizations currently

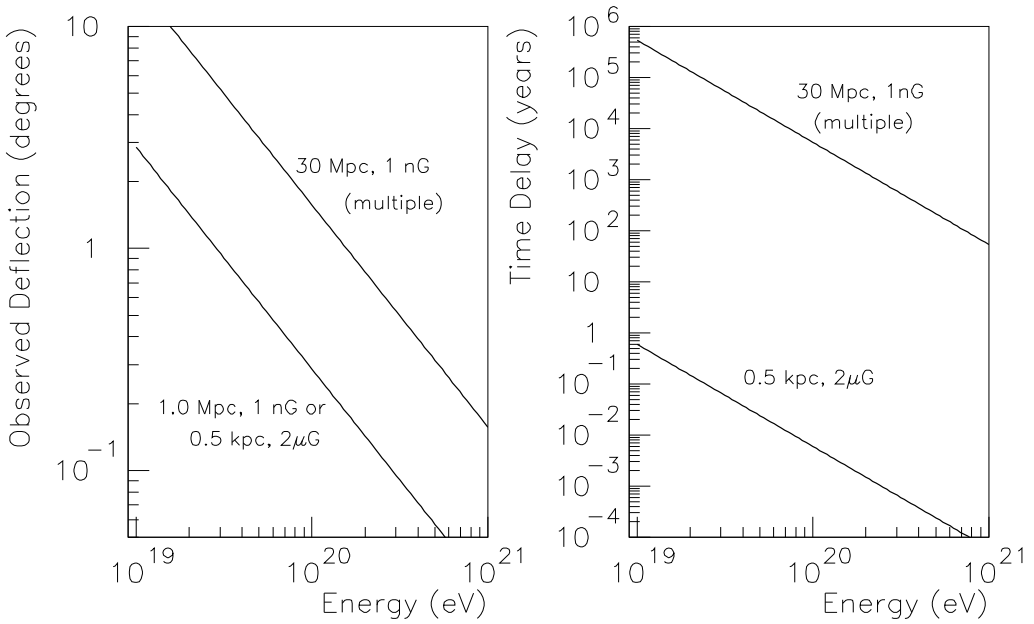

Figure 1.8: Effect of magnetic fields on the propagation of a proton as a function of energy: angular deviation (left) and time delay (right), with respect to a straight line trajectory, in the framework of three realistic scenarios [75].

used is that of Vallée [74]: concentric field lines with a few μG strength and a field reversal at about one half of the disk radius. Outside the disk and in the halo, the field model is based on theoretical prejudice and represented by rapidly decreasing functions (e.g. gaussian outside the disk).

The study of extragalactic fields is mainly based on the Faraday rotation measure (FRM) of the linearly polarized radio sources. The rotation angle actually is a measurement of the integral of the function $n_e B_\parallel$ where n_e is the electron/positron density and $B_\parallel$ the longitudinal field component along the line of sight. Therefore, the FRM needs to be complemented by another measurement, namely that of n_e. This is done by observing the relative time delay versus frequency of waves emitted by a pulsar. Since the group velocity of the signal depends simultaneously on its frequency but also on the plasma frequency of the propagation medium, measurement of the dispersion of the observed signals gives an upper limit on the average density of electrons in the line of sight. Here again, because of the faintness of extragalactic signals, our knowledge of the strength and coherence distances of large scale extragalactic fields is quite weak and only upper limits over large distances can be extracted. An educated guess gives an upper limit of 1 nG for the field strength and coherence lengths of the order of 1 Mpc [73].

A few other more or less indirect methods exist for the study of large

scale magnetic fields. *If* the UHECR are protons and *if* they come from point-like sources, the shape of the source image as a function of the cosmic ray energy will certainly be one of the most powerful of them. The Larmor radius R of a charged particle of charge Ze in kiloparsecs is given by:

$$R_{\rm kpc} \approx \frac{1}{Z}\left(\frac{E}{1\,{\rm EeV}}\right)\left(\frac{B}{1\,\mu{\rm G}}\right)^{-1}$$

The Larmor radius of a charged particle at 320 EeV is larger than the size of the galaxy if its charge is less than 8. If we take the currently accepted upper limit (10^{-9} G) for the extragalactic magnetic fields, a proton of the same energy should have a Larmor radius of 300 Mpc or more.

In Figure 1.8, three different situations are envisaged to evaluate the effects of magnetic fields on a high energy cosmic proton. The situations correspond to what is expected a-) for a trajectory through our galactic disk (0.5 kpc distance inside a 2 μG field) or b-) over a short distance (1 Mpc) through the extragalactic (1 nG) field (same curve), and finally c-) a 30 Mpc trajectory through extragalactic fields with a 1 Mpc coherence length (multiple scattering effect). One can see that at 100 EeV, the deviation in the third case would be about 2°. This gives an idea of the image size if the source is situated inside our local cluster or super-cluster of galaxies. Since the angular resolution of the (present and future) cosmic ray detectors can be comparable to or much better than this value, we expect to be able to locate the point-like sources (if they exist) or establish correlations with large-scale structures.

However, let us remember that this working hypothesis of very weak extragalactic magnetic fields is not universally accepted. Several authors advocated our bad knowledge of those fields showing that the arguments like the puzzling absence of correlations between the direction of the UHECR and either point sources or large structures drop out if one envisages stronger magnetic fields (typically at the μG level) either locally [76] or distributed over larger, cosmological, scales [77].

Finally, worth mentioning is the possibility to study EGMF with simulation of large structures formation. Some progresses have been obtained in this field, though the results have still to be significantly improved due to the technical difficulties involved and the large amount of computational resources required. The main results have been obtained in refs. [78] and [79]. Qualitatively the simulations agree in finding that EGMFs are mainly localized in galaxy clusters and filaments, while voids should contain only primordial fields. However, the conclusions of Refs. [78] and [79] are quantitatively rather different and further work is still required to make more reliable the results.

1.6.2 Large Scale Anisotropies

In the search for potential sources, the propagation arguments incite us to

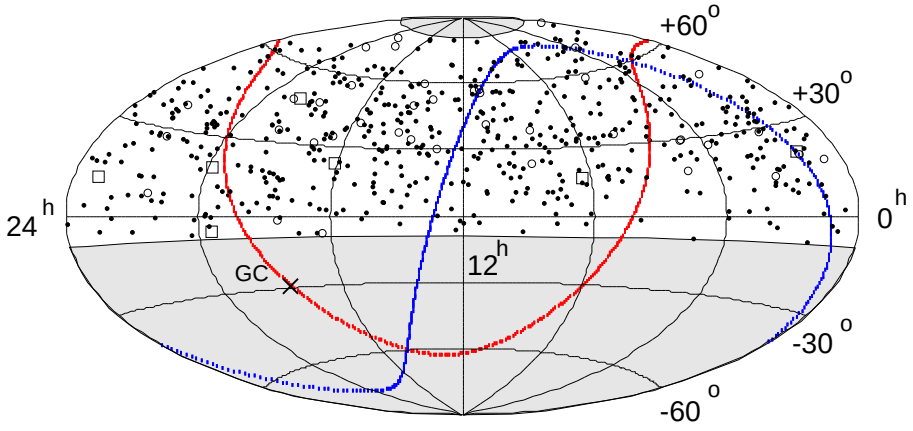

Figure 1.9: Arrival directions of cosmic rays with energies above 10 EeV (equatorial coordinates), as measured by the AGASA experiment [80]. The thick dotted lines show the galactic and supergalactic planes (GC indicating the galactic center). The shaded regions are those invisible to the AGASA detector.

look for correlations with the distribution of astrophysical matter within a few tens of Mpc. In our neighborhood, there are two structures showing an accumulation of objects, both only partially visible from any hemisphere: the galactic disk on a small scale and the supergalactic plane on a large scale, a structure roughly normal to the galactic plane, extending to distances up to $z \approx 0.02$ (about 100 Mpc) and correlated with a denser distribution of radio galaxies. In equatorial coordinates with the hypothesis of an isotropic distribution of the sources, and over large periods of data taking, the right ascension distribution of events must be uniform and the declination distribution can be parameterized with the known zenith angle dependence of the detector aperture.

An analysis on the correlation between arrival directions and possible source locations was done by the AGASA experiment for the highest energy range [80]. The analysis is based on 581 events above 10 EeV, a subset of 47 events above 40 EeV and 7 above 100 EeV. Figure 1.9 is a compilation of the total sample in equatorial coordinates. The dots, circles and squares are respectively events with energies above 10, 40 and 100 EeV. The data show no deviation from the expected uniform right ascension distribution. An excess of 2.5 σ is found at a declination of 35° and can be interpreted as a result of observed clusters of events (see below). No convincing deviation from isotropy is found when the analysis is performed in galactic coordinates.

The same collaboration [81] made also a similar analysis for the lower energy region (events down to 1 EeV and detected with zenith angles up to 60°). In this article, a slight effect of excess events in the direction of the galactic center was announced. A similar study [82] with the Fly's Eye data, concludes on a small correlation with the galactic plane for events with energies lower than 3.2 EeV and isotropy for higher energies.

In summary, both the AGASA and Fly's Eye experiments seem to converge on some anisotropy in the EeV range (correlation with the galactic plane and center) and isotropy above a few tens of EeV. With the present data it is difficult to come to any clear conclusion on the anisotropy issues, especially at the highest energies. All we can do is acknowledge the problems and make a list of technical requirements to solve them. First of all, and whatever the analysis methods used, statistics is the sinews of war. One needs at least an order of magnitude in the rate with which we are detecting the relevant events in the highest energy range, hence in the collecting detectors' aperture. This is the principal aim of the next generation of experiments. Second, the powerful harmonic analysis needs full sky coverage and, as much as possible, uniform exposure. This means data from both hemispheres. All the data used in the above analyses come from the northern hemisphere. Possible correlations with the galactic plane or the galactic center will only be confirmed, or invalidated, if a detector systematically explores the southern sky. Also, due to day-night effects, a fluorescence detector does not have a uniform right-ascension coverage. One should also take into account the angular acceptance. The scintillator technique (used in the AGASA detector) has an intrinsic limitation for large angles. The use of Cerenkov tanks (as in the Haverah Park experiment) circumvents this limitation: it can even detect horizontal showers with equal efficiency, although the bending of the charged particles of the shower makes the analysis more difficult for large angles. All these constraints have been carefully considered in the design of the next generation experiments.

We will try in the next two chapters to make clearer the expectations for Large Scale anisotropies together with a forecast of the statistics required to safely detect them; also, we will examine not only the AGASA and Fly's Eye data, but all the actual available data at high energies (roughly $\sim$100) in search of some hint of correlation with LSS.

1.6.3 Small Scale Anisotropies

If the sources of UHECR are nearby astrophysical objects and if, as expected, they are in small numbers, a selection of the events with the largest magnetic rigidity would combine into multiplets or clusters which would indicate the

direction to look for an optical or radio counterpart. Such an analysis was done systematically by the AGASA group [80]. Figure 1.10 shows the sub-

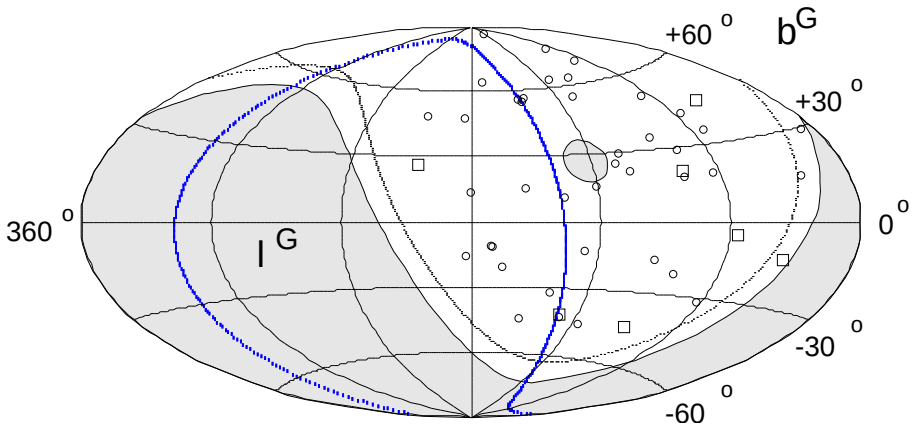

Figure 1.10: Arrival directions of cosmic rays with energies above 40 EeV (galactic coordinates), as measured by the AGASA experiment [80].

sample of events in the AGASA catalog with energies in excess of 100 EeV (squares) and in the range 40-100 EeV (circles). A multiplet is defined as a group of events whose error boxes (2.5° circles) overlap. One can see that there are three doublets and one triplet. If one adds the Haverah Park events, the most southern doublet also becomes a triplet. The chance probability of having as many multiplets as observed with a uniform distribution are estimated by the authors to less than 1%. However, it should be noted that the chance probability is very difficult to evaluate in an *a posteriori* analysis and depends strongly on the assumed experimental error box size.

A search for nearby astrophysical objects within an angle of 4° from any event in a multiplet was also done, and produced a few objects. One of the most interesting candidates is Mrk 40, a galaxy collision, since the shock waves generated in such phenomena are considered by some authors [83] as being valid accelerating sites.

Another way of using the observed multiplets, *assuming* that they come from an extragalactic point source, is to consider the galactic disk as a magnetic spectrometer which can give information on the charge of the incident cosmic rays. A detailed analysis, using different galactic magnetic field models has been performed in ref. [84].

Chapter 2

The large-scale structure of the Universe

Given the relevant role that LSS play in the subsequent chapters, a brief review is provided in the present chapter partly based on the papers [85; 86; 87; 88; 89] on which we address the reader for further details. Some of the recent and past observational results are discussed together with the last results from computational intensive N-body simulations. The conventional paradigm of Structure Formation is discussed in which weak ripples in the primordial plasma have been amplified by gravitational forces, resulting finally in the present dark matter haloes and galaxies.

2.1 Introduction

The past two and a half decades have seen enormous advances in the study of cosmic structure, both in our knowledge of how it is manifest in the large-scale matter distribution, and in our understanding of its origin. A new generation of galaxy surveys – the 2-degree Field Galaxy Redshift Survey, or 2dFGRS[90], and the Sloan Digital Sky Survey, or SDSS2[91] – have quantified the distribution of galaxies in the local Universe with a level of detail and on length scales that were unthinkable just a few years ago. Surveys of quasar absorption and of gravitational lensing have produced qualitatively new data on the distributions of diffuse intergalactic gas and of dark matter. At the same time, observations of the cosmic microwave background radiation, by showing us the Universe when it was only about 400,000 years old, have vindicated bold theoretical ideas put forward in the 1980s regarding the contents of the Universe and the mechanism that initially generated structure shortly after the Big Bang. The critical link between the early, near-uniform Universe and the rich structure seen at more recent times has been provided by direct numerical simulation. This has made use of the unremitting increase in the power of modern computers to create ever more realistic virtual

universes: simulations of the growth of cosmic structure that show how astrophysical processes have produced galaxies and larger structures from the primordial soup. Together, these advances have led to the emergence of a "standard model of cosmology" which, although seemingly implausible, has nevertheless been singularly successful.

Figure 2.1 strikingly illustrates how well this standard model can fit nearby structure. The observational wedge plots at the top and at the left show subregions of the SDSS and 2dFGRS, illustrating the large volume they cover in comparison to the ground-breaking Center for Astrophysics (CfA) galaxy redshift survey[92] carried out during the 1980s (the central small wedge). These slices through the local three-dimensional galaxy distribution reveal a tremendous richness of structure. Galaxies, groups and clusters are linked together in a pattern of sheets and filaments that is commonly known as the "cosmic web"[93]. A handful of particularly prominent aggregations clearly stand out in these images, the largest containing of the order of 10,000 galaxies and extending for several hundred million light years. The corresponding wedge plots at the right and at the bottom show similarly constructed surveys of a virtual universe, the result of a simulation of the growth of structure and of the formation of galaxies in the current standard model of cosmology. The examples shown were chosen among a set of random "mock surveys" to have large structures in similar positions to the real surveys. The similarity of structure between simulation and observation is striking, and is supported by a quantitative comparison of clustering[94].

In Fig. 2.2 is instead illustrated the very local universe ($z<0.06$) through the photometric observations of the 2Mass Survey [141]. The filamentary structure is visible even more clearly near us while, at the same time, the contrast with the large voids is striking.

The early 1980s produced two audacious ideas that transformed a speculative and notoriously uncertain subject into one of the most rapidly developing branches of physics. The first was the proposal that the ubiquitous dark matter that dominates large-scale gravitational forces consists of a new (and still unidentified) weakly interacting elementary particle. Because these particles are required to have small random velocities at early times, they were dubbed "cold dark matter" or CDM. (Hot dark matter is also possible, for example a neutrino with a mass of a few tens of electron volts. Early cosmological simulations showed, however, that the galaxy distribution in a universe dominated by such particles would not resemble that observed[95].) The second idea is "cosmic inflation"[96], the proposal that the Universe grew exponentially for many doubling times perhaps $\sim 10^{35}$ seconds after the Big Bang, driven by the vacuum energy density of an effective scalar field that rolls slowly from a false to the true vacuum. Quantum fluctuations in this

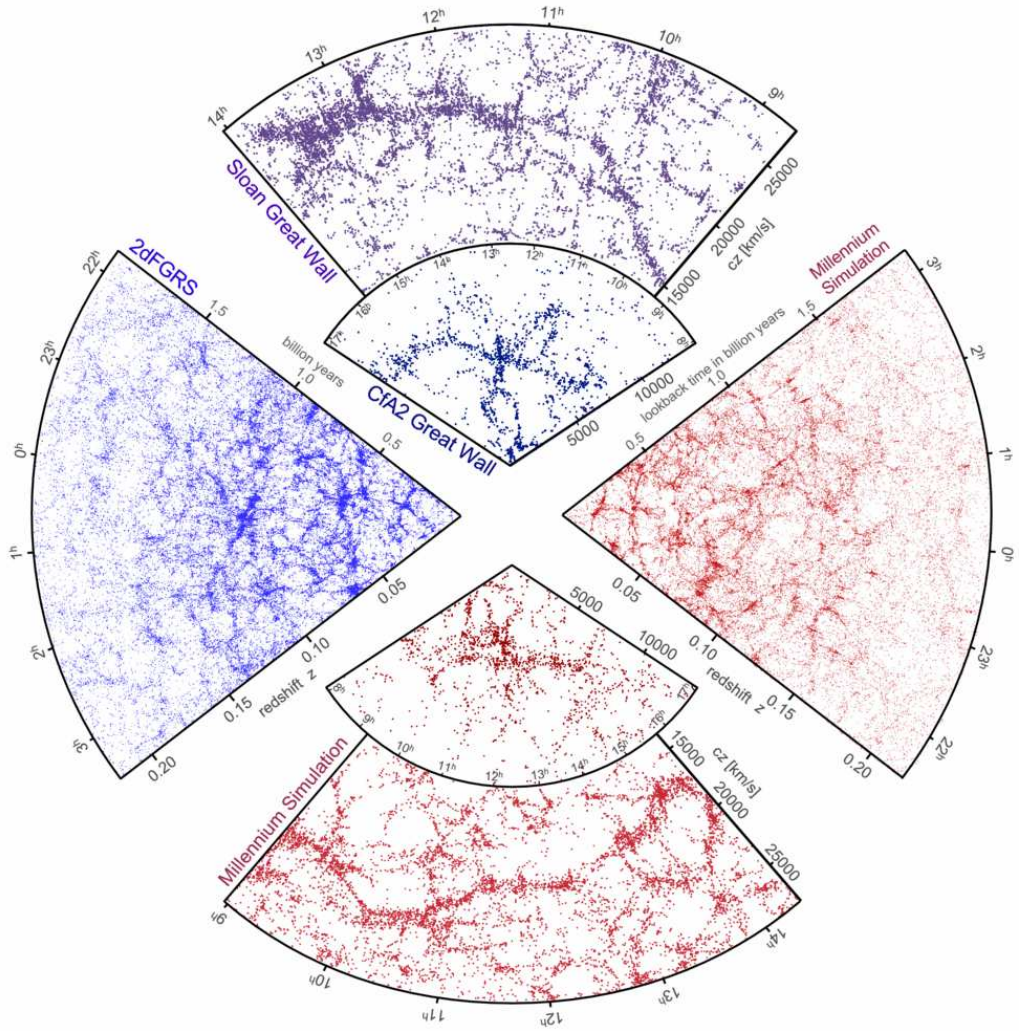

Figure 2.1: The galaxy distribution obtained from spectroscopic redshift surveys and from mock catalogues constructed from cosmological simulations. The small slice at the top shows the CfA2 "Great Wall"[92], with the Coma cluster at the centre. Drawn to the same scale is a small section of the SDSS, in which an even larger "Sloan Great Wall" has been identified[87]. This is one of the largest observed structures in the Universe, containing over 10,000 galaxies and stretching over more than 1.37 billion light years. The wedge on the left shows one-half of the 2dFGRS, which determined distances to more than 220,000 galaxies in the southern sky out to a depth of 2 billion light years. The SDSS has a similar depth but a larger solid angle and currently includes over 650,000 observed redshifts in the northern sky. At the bottom and on the right, mock galaxy surveys constructed using semi-analytic techniques to simulate the formation and evolution of galaxies within the evolving dark matter distribution of the "Millennium" simulation[94] are shown, selected with matching survey geometries and magnitude limits.

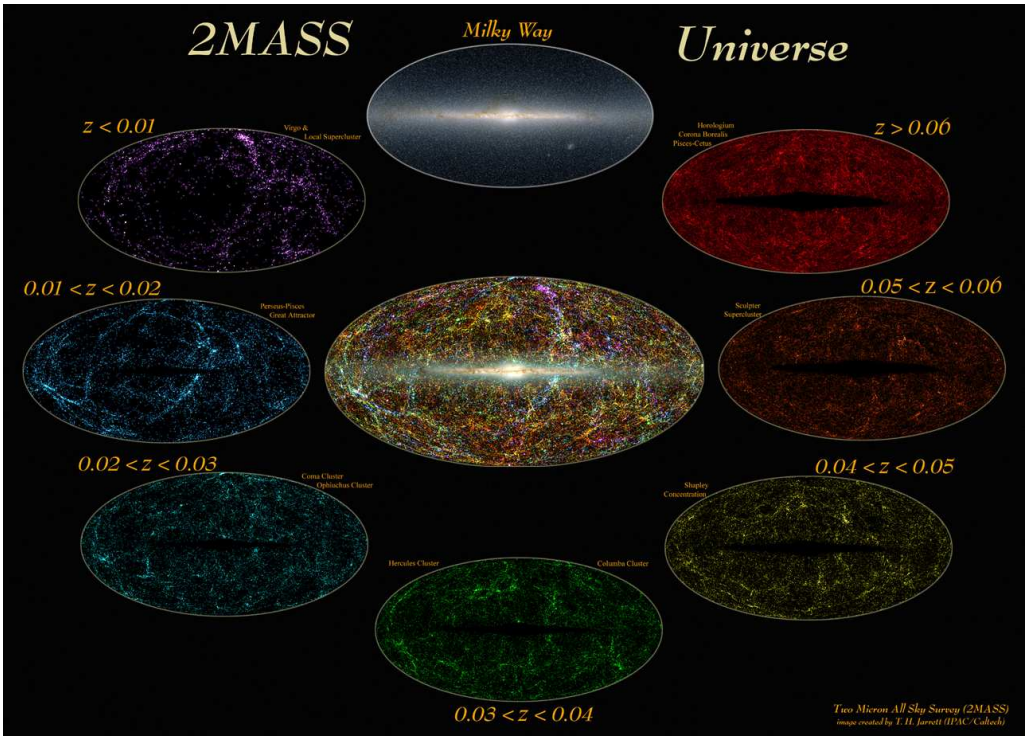

Figure 2.2: The Large Scale Structure of the nearby universe (z<0.06) mapped by the 2Mass survey [141]. The galaxies of the sample are divided into seven layers of redshift (binned in Δz=0.01) showing the well known local structures. In the first slide dominant is the Virgo Cluster; the second slide shows the Perseus cluster and the Great Attractor; the third the Coma and Ophiuchus clusters; the fourth the Hercules and the Columba clusters; the fifth the Shapley Concentration; the sixth the Sculptur Super-Cluster and the last the Horologium, the Corona Borealis and the Pisces-Cetus Super-Clusters. The galaxies' redshifts are calculated through a photometric technique as described in [142].

"inflaton" field are blown up to macroscopic scales and converted into genuine ripples in the cosmic energy density. These weak seed fluctuations grow under the influence of gravity and eventually produce galaxies and the cosmic web. Simple models of inflation predict the statistical properties of these primordial density fluctuations: their Fourier components should have random and independent phases and a near-scale-invariant power spectrum[97]. Inflation also predicts that the present Universe should have a flat geometry. With concrete proposals for the nature of the dark matter and for the initial fluctuation distribution, the growth of cosmic structure became, for the first time, a well-posed problem that could be tackled with the standard tools of physics.

The backbone of the cosmic web is the clumpy yet filamentary distribution

of dark matter. The presence of dark matter was first inferred from the dynamics of galaxy clusters by Zwicky[98]. But it took over half a century for dark matter to become an integral part of our view of galaxies and of the Universe as a whole, and for its average density to be estimated reliably. Today, the evidence for the pervasive presence of dark matter is overwhelming and includes galactic rotation curves, the structure of galaxy groups and clusters, large-scale cosmic flows and, perhaps most directly, gravitational lensing, a phenomenon first proposed as an astronomical tool by Zwicky himself[99]. The distorted images of background galaxies as their light travels near mass concentrations reveal the presence of dark matter in the outer haloes of galaxies[100; 101], in galaxy clusters[102] and in the general mass field[103].

When expressed in units of the critical density required for a flat cosmic geometry, the mean density of dark matter is usually denoted by $\Omega_{\rm dm}$. Although a variety of dynamical tests have been used to constrain $\Omega_{\rm dm}$, in general such tests give ambiguous results because velocities are induced by the unseen dark matter and the relation of its distribution to that of the visible tracers of structure is uncertain. The notion of a substantial *bias* in the galaxy distribution relative to that of dark matter was introduced in the 1980s to account for the fact that different samples of galaxies or clusters are not directly tracing the underlying matter distribution. Defined simply as the ratio of the clustering strengths, the "bias function" was also invoked to reconcile low dynamical estimates for the mass-to-light ratio of clusters with the high global value required in the theoretically preferred flat, $\Omega_{\rm dm} = 1$ universe. But because massive clusters must contain approximately the universal mix of dark matter and baryons (ordinary matter), bias uncertainties are neatly bypassed by comparing the measured baryon fraction in clusters with the universal fraction under the assumption that the mean baryon density, $\Omega_{\rm b}$, is the value inferred from Big Bang nucleosynthesis[104]. Applied to the Coma cluster, this simple argument gave $\Omega_{\rm dm} \leq 0.3$ where the inequality arises because some or all of the dark matter could be baryonic[104]. This was the first determination of $\Omega_{\rm dm} < 1$ that could not be explained away by invoking bias.

The mean baryon density implied by matching Big Bang nucleosynthesis to the observed abundances of the light elements is only $\Omega_{\rm b}h^2 \simeq 0.02$, where h denotes the Hubble constant in units of $100\,{\rm km\ s^{-1}Mpc^{-1}}$. Dynamical estimates, although subject to bias uncertainties, have long suggested that $\Omega_{\rm m} = \Omega_{\rm dm} + \Omega_{\rm b} \simeq 0.3$, implying that the dark matter cannot be baryonic. Plausibly it is made up of the hypothetical elementary particles postulated in the 1980s, for example axions or the lowest mass supersymmetric partner of the known particles. Such low estimates of the mean matter density $\Omega_{\rm m}$

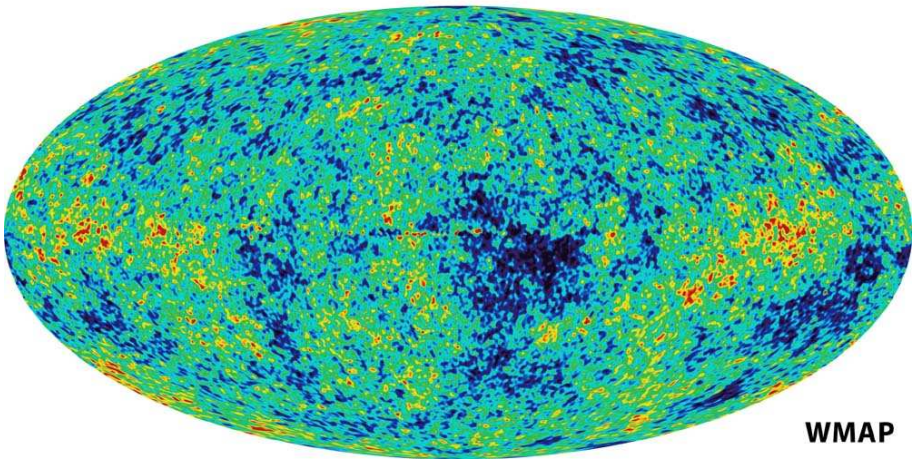

Figure 2.3: The map of CMB anisotropies as determined by the WMAP mission [105].

are incompatible with the flat geometry predicted by inflation unless the Universe contains an additional unclustered and dominant contribution to its energy density, for example a cosmological constant Λ such that $\Omega_{\rm m} + \Omega_\Lambda \simeq 1$. Two large-scale structure surveys carried out in the late 1980s, the APM (automated photographic measuring) photographic survey[106] and the QDOT redshift survey of infrared galaxies[107], showed that the power spectrum of the galaxy distribution, if it traces that of the mass on large scales, can be fitted by a simple CDM model only if the matter density is low, $\Omega_{\rm m} \simeq 0.3$. This independent confirmation of the dynamical arguments led many to adopt the now standard model of cosmology, ΛCDM.

It was therefore with a mixture of amazement and *déjà vu* that cosmologists greeted the discovery in 1998 of an accelerated cosmic expansion[108; 109]. Two independent teams used distant type Ia supernovae to perform a classical observational test. These "standard candles" can be observed out to redshifts beyond 1. Those at $z \geq 0.5$ are fainter than expected, apparently indicating that the cosmic expansion is currently speeding up. Within the standard Friedmann cosmology, there is only one agent that can produce an accelerating expansion: the cosmological constant first introduced by Einstein, or its possibly time- or space-dependent generalization, "dark energy". The supernova evidence is consistent with $\Omega_\Lambda \simeq 0.7$, just the value required for the flat universe predicted by inflation.

The other key prediction of inflation, a density fluctuation field consistent with amplified quantum noise, received empirical support from the discovery by the COsmic Background Explorer (COBE) satellite in 1992 of

small fluctuations in the temperature of the cosmic microwave background (CMB) radiation[110]. These reflect primordial density fluctuations, modified by damping processes in the early Universe which depend on the matter and radiation content of the Universe. More recent measurements of the CMB[111; 112] culminating with those by the WMAP (Wilkinson Microwave Anisotropy Probe) satellite[105] have provided a striking confirmation of the inflationary CDM model: the measured temperature fluctuation spectrum is nearly scale-invariant on large scales and has a series of "acoustic" peaks that reflect the coherent oscillations experienced by the photon-baryon fluid before the moment when the primordial plasma recombined and the radiation escaped. The fluctuation spectrum depends on the parameters that define the geometry and content of the Universe and the initial fluctuation distribution, so their values are constrained by the data. In practice, there are degeneracies among the parameters, and the strongest constraints come from combining the CMB data with other large-scale structure datasets. Present estimates[105; 113; 114] give a flat universe with $\Omega_{\rm dm} = 0.20 \pm 0.020$, $\Omega_{\rm b} = 0.042 \pm 0.002$, $\Omega_\Lambda = 0.76 \pm 0.020$, $h = 0.74 \pm 0.02$. The consistency of these values with other independent determinations and the close agreement of the CMB data with theoretical predictions formulated over 20 years earlier[115] belong amongst the most remarkable successes of modern cosmology.

2.2 The growth of large-scale structure

The microwave background radiation provides a clear picture of the young Universe, where weak ripples on an otherwise uniform sea display a pattern that convincingly supports our standard model for the cosmic mass/energy budget and for the process that initially imprinted cosmic structure. At that time there were no planets, no stars, no galaxies, none of the striking large-scale structures seen in Fig. 2.1. The richness of the observed astronomical world grew later in a complex and highly nonlinear process driven primarily by gravity. This evolution can be followed in detail only by direct numerical simulation. Early simulations were able to reproduce qualitatively the structure observed both in large galaxy surveys and in the intergalactic medium[116; 117]. They motivated the widespread adoption of the CDM model well before it gained support from microwave background observations. Many physical processes affect galaxy formation, however, and many aspects must be treated schematically within even the largest simulations. The resulting uncertainties are best estimated by exploring a wide range of plausible descriptions and checking results against observations of many

different types.

In a ΛCDM universe, quasi-equilibrium dark matter clumps or "haloes" grow by the collapse and hierarchical aggregation of ever more massive systems, a process described surprisingly well by the phenomenological model of Press and Schechter and its extensions[118; 119]. Galaxies form at the centres of these dark haloes by the cooling and condensation of gas which fragments into stars once it becomes sufficiently dense. Groups and clusters of galaxies form as haloes aggregate into larger systems. They are arranged in the "cosmic web", the larger-scale pattern of filaments and sheets which is a nonlinear gravitational "sharpening" of the pattern already present in the gaussian random field of initial fluctuations[93]. The first observable objects were probably massive stars collapsing in small haloes and switching on at redshifts of 50 and higher[120]. By a redshift of 15 these may have been sufficiently numerous for their radiation to re-ionize all the gas in the Universe. So far they have not been observed directly, but it is one of the main goals of the next generation of low-frequency radio telescopes to observe their effects directly in the strongly redshifted 21-cm transition of neutral hydrogen.

Detailed simulations from ΛCDM initial conditions have been used to study the formation of the first luminous objects and the re-ionization of the Universe, but these still await testing against observation[121]. In contrast, predictions for the structure, the ionization state and the heavy element content of intergalactic gas at redshifts below 6 can be checked in detail against absorption features observed in the spectra of distant quasars. These provide, in effect, a one-dimensional tomographic image of the intervening large-scale structure.

At lower redshift direct and quantitative measures of large-scale structure can be obtained from the weak, coherent distortions of the images of faint galaxies induced by gravitational lensing as their light travels through the intervening cosmic web[122]. The distortions depend only on the gravitational field in intergalactic space and so lensing data test predictions for the mass distribution in a way that is almost independent of the complex astrophysics that determines the observable properties of galaxies. The lensing effect is very weak, but can be measured statistically to high precision with large enough galaxy samples.

The Lyman-α forest and gravitational lensing provide windows onto the large-scale structure of the Universe that complement those obtained from galaxy surveys by extending the accessible redshift range and, more importantly, by measuring the structure in the diffuse gas and in the total mass distribution rather than in the distribution of galaxies. In principle, these measures should have different (and perhaps weaker) sensitivity to the many uncertain aspects of how galaxies form. Remarkably, all three measures are

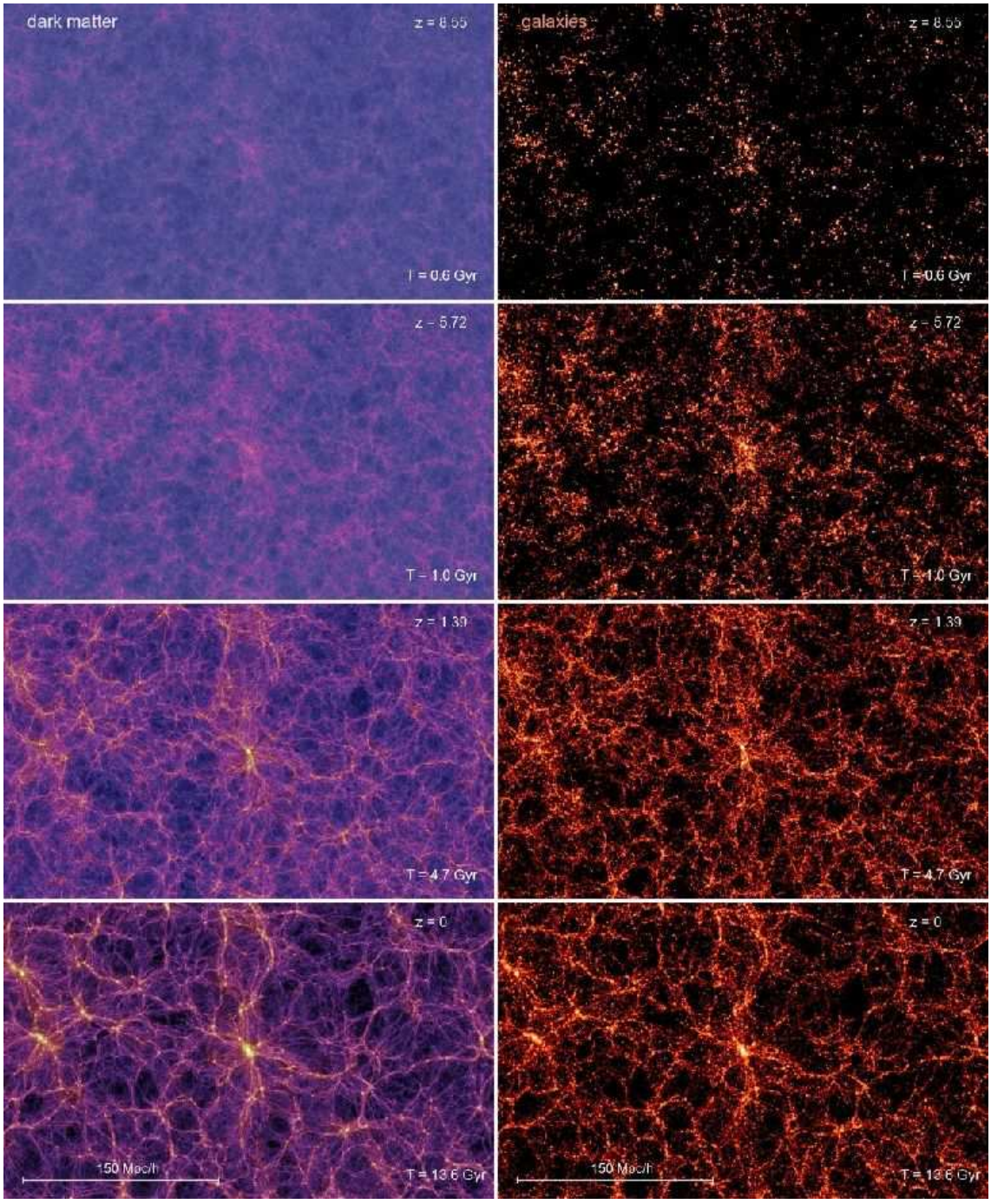
dark matter
z = 8.55
T = 0.6 Gyr
galaxies
z = 8.55
T = 0.6 Gyr
z = 5.72
T = 1.0 Gyr
z = 5.72
T = 1.0 Gyr
z = 1.39
T = 4.7 Gyr
z = 1.39
T = 4.7 Gyr
z = 0
150 Mpc/h
T = 13.6 Gyr
z = 0
150 Mpc/h
T = 13.6 Gyr

Figure 2.4: Time evolution of the cosmic large-scale structure in dark matter and galaxies, obtained from cosmological simulations of the ΛCDM model. The panels on the left show the projected dark matter distribution in slices of thickness $15\,h^{-1}$Mpc, extracted at redshifts $z = 8.55$, $z = 5.72$, $z = 1.39$ and $z = 0$ from the Millennium N-body simulation of structure formation[94]. These epochs correspond to times of 600 million, 1 billion, 4.7 billion and 13.6 billion years after the Big Bang, respectively. The colour hue from blue to red encodes the local velocity dispersion in the dark matter, and the brightness of each pixel is a logarithmic measure of the projected density. The panels on the right show the predicted distribution of galaxies in the same region at the corresponding times obtained by applying semi-analytic techniques to simulate galaxy formation in the Millennium simulation[94]. Each galaxy is weighted by its stellar mass, and the colour scale of the images is proportional to the logarithm of the projected total stellar mass. The dark matter evolves from a smooth, nearly uniform distribution into a highly clustered state, quite unlike the galaxies, which are strongly clustered from the start.

consistent both with each other and with the standard model at the level that quantitative comparison is currently possible[124; 114; 123].

Galaxy surveys such as those illustrated in Fig. 2.1 contain an enormous amount of information about large-scale structure. The strength of clustering is known to depend not only on galaxy luminosity, colour, morphology, gas content, star-formation activity, type and strength of nuclear activity and halo mass, but also on the spatial scale considered and on redshift. Such dependencies reflect relations between the formation histories of galaxies and their larger-scale environment. Some (for example, the dependence on halo or galaxy mass) are best thought of as deriving from the statistics of the initial conditions. Others (for example the dependence on nuclear or star-formation activity) seem more naturally associated with late-time environmental influences. Early studies attempted to describe the relation between the galaxy and mass distributions by a *bias function*. Recent data suggest that this concept is of limited value. Except, perhaps, on the largest scales; bias estimates depend not only on scale, redshift and galaxy properties, but also on the particular measure of clustering studied. Understanding the link between the mass and galaxy distributions requires realistic simulations of the galaxy formation process throughout large and representative regions of the Universe. Given the complexity of galaxy formation, such simulations must be tuned "by hand" to match as many of the observed properties of galaxies as possible. Only if clustering turns out to be insensitive to such tuning can we consider the portrayal of large-scale structure to be robust and realistic.

In Fig. 2.4 we show the time evolution of the mass and galaxy distributions in a small subregion of the largest simulation of this type yet[94]. The emergence of the cosmic web can be followed in stunning detail, producing a tight network of filaments and walls surrounding a foam of voids.

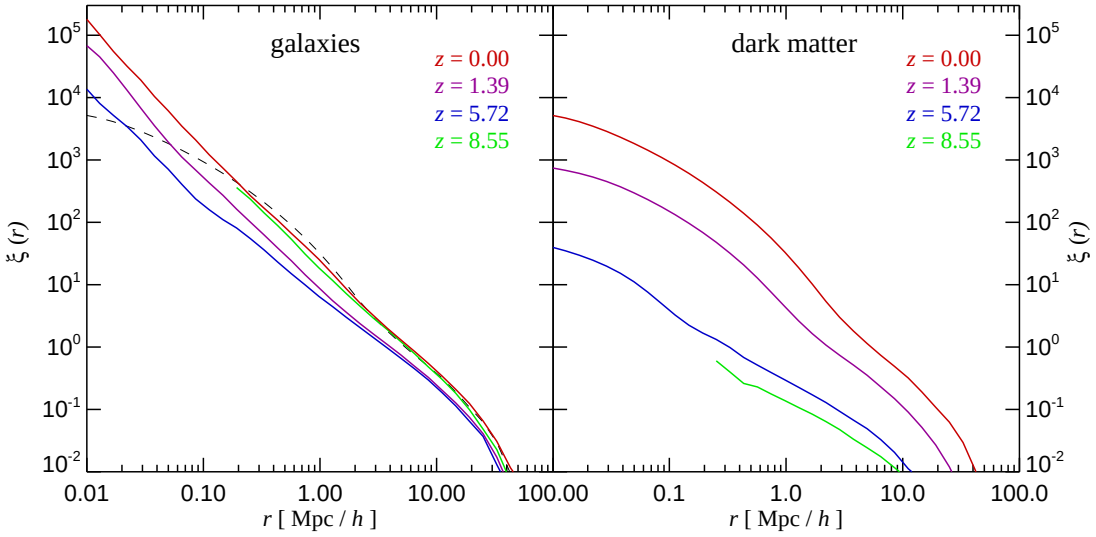

Figure 2.5: Two-point correlation function of galaxies and dark matter at different epochs, in the Millennium simulation of structure formation[94]. The panel on the left gives the I-band galaxy correlation function ξ (selected according to $M_{\rm I} - 5\log h < -20$ in the rest-frame) at redshifts $z = 8.55$, $z = 5.72$, $z = 1.39$ and $z = 0$ (corresponding to the epochs depicted in Fig. 4). The panel on the right shows the dark matter correlation functions at the same epochs. For comparison, the present-day dark matter correlation function is also drawn as a dashed line in the left panel. At $z = 8.55$, only data for $r > 200\,h^{-1}$kpc are shown because the finite numerical resolution of the simulation precludes an accurate representation of the mass distribution on smaller scales than this at early times. The galaxy correlation function has a near power-law behavior over several orders of magnitude and has almost equal strength at $z = 8.55$ and $z = 0$. By contrast, the dark matter correlation function grows by a large factor over this time span, and has a different shape from the galaxy correlation function.

This characteristic morphology was seen in the first generation of cold dark matter simulations carried out over 20 years ago[116], but the match was not perfect; the recipe adopted to relate the galaxy and mass distributions was too crude to reproduce in detail the clustering of galaxies. It has taken models like those of Fig. 2.4 to explain why the observed galaxy autocorrelation function is close to a power law whereas the simulated dark matter autocorrelation function shows significant features[125; 94].

Simulated autocorrelation functions for dark matter and for galaxies are shown in Fig. 2.5 for the same times imaged in Fig. 2.4. The shape difference between the two is very evident, and it is remarkable that at $z = 0$ the power-law behavior of the galaxy correlations extends all the way down to 10 kpc, the observed size of galaxies.

A striking feature of Fig. 2.4 is the fact that while the growth of large-

scale structure is very clear in the mass distribution, the galaxy distributions appear strongly clustered at all times. This difference shows up dramatically in the autocorrelation functions plotted in Fig. 2.5 and has been a prediction of CDM theories since the first simulations including crude bias recipes[116]. A decade later when direct measurements of galaxy clustering at redshifts as high as $z \sim 3-4$ found "surprisingly" large amplitudes, comparable to those found in the present-day Universe[126], the results turned out to be in good agreement with estimates based on more detailed modelling of galaxy formation in a CDM universe[127]. In effect, the galaxies already outline the pattern of the cosmic web at early times, and this pattern changes relatively little with the growth of structure in the underlying dark matter distribution.

2.3 Outlook

Very few of the important questions in cosmology and large-scale structure can be regarded as closed. The recent history of the subject provides a vivid reminder of how new theoretical insights and/or new observational datasets can quickly overturn conventional wisdom in rapidly advancing fields of science. At the present time, the two outstanding questions are the identity of the dark matter and the nature of the dark energy.

There is every reason to be optimistic about the prospects of detecting cold dark matter particles from the halo of our Galaxy, either directly in laboratory searches or indirectly through particle annihilation radiation. Additionally, if cold dark matter is indeed a supersymmetric particle, evidence for its existence may be forthcoming from experiments at CERN's large-hadron collider[128].

Unravelling the nature of the dark energy is a much more daunting task. A strategy that has gained momentum in recent years is to set tighter empirical constraints on the amount of dark energy and on its possible time evolution. Large projects such as the Joint Dark Energy Mission, currently at an early design phase, are being planned to measure the equation of state parameter, $w = P/(\rho c^2)$, of the dark energy, where P is the "dark pressure" of the vacuum, and its time evolution, $w' = \mathrm{d}w/\mathrm{d}z$. The hope is that such empirical constraints will clarify the nature of the dark energy and perhaps point to a field-theoretical explanation. The range of possibilities is large. We might find that the dark energy interacts with the dark matter, or that the dark energy is not a field at all but rather a manifestation of some nonlinear effect within general relativity or one of its extensions.

Progress towards constraining dark energy is likely to come both from refinements of classical cosmological probes and from entirely new ways to

study large-scale structure. Examples in the first category include measuring the abundance of galaxy clusters as a function of cosmic time. This probes the growth of the mass fluctuation spectrum and the variation of the cosmological volume element[129]. Extending such measurements to redshifts $z \gtrsim 1$ may set useful constraints on the dark energy equation of state, provided systematic effects can be kept under control. Also promising are observations of high-redshift type Ia supernovae for much larger samples than have been accumulated so far. Again, it will be crucial to control systematic effects. The PLANCK satellite mission and subsequent polarization-optimized experiments will make definitive measurements of the CMB and perhaps unlock some of its last secrets.

Examples of new tests of the large-scale structure include weak lensing tomography and the study of baryon oscillations in the matter distribution at late times. The physical mechanism that generated acoustic peaks in the CMB temperature power spectrum also imprinted an oscillatory feature in the linear power spectrum of the dark matter[130]. The Virgo consortium's Millennium simulation, illustrated in Fig. 2.1 and Fig. 2.4, demonstrated that the oscillations survive the destructive influence of nonlinear gravitational evolution even to the present day, albeit in distorted form[94]. Most importantly, this simulation also demonstrated that these "baryon wiggles" should be visible in suitably selected galaxy samples. Early indications suggest that the baryon oscillations in the galaxy distribution have, in fact, been detected in the 2dFGRS and SDSS[131], although at comparatively low statistical significance.

In the more distant future, there are hopes that one day we will be able to probe the inflationary epoch directly by detecting the predicted background of gravitational waves[132; 133]. In the meantime, astrophysical studies of large-scale structure will continue to grow and to diversify, focusing on new issues such as the nature and evolution of nonlinear structure during the first billion years where we currently have no direct observations. Today, through the joint mysteries of dark matter and dark energy, cosmology arguably poses some of the most fundamental and exciting challenges of contemporary science.

Chapter 3

The footprint of large scale cosmic structure on the ultra-high energy cosmic ray distribution

Current experiments collecting high statistics in ultra-high energy cosmic rays (UHECRs) are opening a new window on the universe. In this chapter we discuss a large scale structure model for the UHECR origin which evaluates the expected anisotropy in the UHECR arrival distribution starting from a given astronomical catalogue of the local universe. The model takes into account the main selection effects in the catalogue and the UHECR propagation effects. By applying this method to the IRAS PSCz catalogue, we derive the minimum statistics needed to significatively reject the hypothesis that UHECRs trace the baryonic distribution in the universe, in particular providing a forecast for the Auger experiment.

3.1 Introduction

For the study of UHECRs anisotropies in this chapter, we shall work under the (conservative) assumptions that UHE astronomy is possible, namely: i) proton primaries, for which $e\mathcal{R} = E$; ii) EGMF negligibly small; iii) extragalactic astrophysical sources are responsible for UHECR acceleration.

Beside the observation of small-scale clustering by AGASA [80] (however, not confirmed by other experiments with comparable or larger statistics [134; 135]), we will focus on looking for large scale anisotropies in the data, eventually correlating with some known configuration of astrophysical source candidates. In this context, the most natural scenario to be tested is that UHECRs correlate with the luminous matter in the "local" universe. This is particularly expected for candidates like gamma ray bursts (hosted more likely in star formation regions) or colliding galaxies, but it is also a sufficiently generic hypothesis to deserve an interest of its own.

Aims of this chapter are: i) to describe a method to evaluate the expected anisotropy in the UHECR sky starting from a given catalogue of the local universe, taking into account the selection function, the blind regions as well as the energy-loss effects; ii) to assess the minimum statistics needed to significatively reject the null hypothesis, in particular providing a forecast for the Auger experiment. Previous attempts to address a similar issue can be found in [136; 137; 138; 139]. Later in the chapter we will come back to a comparison with their approaches and results.

The catalogue we use is IRAS PSCz [140]. This has several limitations, mainly due to its intrinsic incompleteness, but it is good enough to illustrate the main features of the issue, while still providing some meaningful information.

The chapter is structured as follows: the catalogue and the related issues are discussed in Section 3.2. In Section 3.3 we describe the technique used for our analysis. The results are discussed in Section 3.4, where we compare our findings with those obtained in previous works. In Section 3.5 we give a brief overview on ongoing research and experimental activities, and draw our conclusions.

3.2 Astronomical Data

3.2.1 The Catalogue

Two properties are required to make a galaxy catalogue suitable for the type of analysis discussed here. First, a great sky coverage is critical for comparing the predictions with the fraction of sky observed by the UHECR experiments (the Auger experiment is observing all the Southern hemisphere and part of the Northern one). Second, the energy-loss effect in UHECR propagation requires a knowledge of the redshifts for at least a fair subsample of the galaxies in the catalogue. Selection effects both in fluxes and in redshifts play a crucial role in understanding the final outcome of the simulations.

Unfortunately, in practical terms this two requirements turn out to be almost complementary and no available catalogue matches both needs simultaneously. A fair compromise is offered by the IRAS PSCz catalogue [140] which contains about 15 000 galaxies and related redshifts with a well understood completeness function down to $z \sim 0.1$ —i.e. down to a redshift which is comparable to the attenuation length introduced by the GZK effect— and a sky coverage of about 84%. The incomplete sky coverage is mainly due to the so called zone of avoidance centered on the Galactic Plane and caused by the galactic extinction and to a few, narrow stripes which were not observed

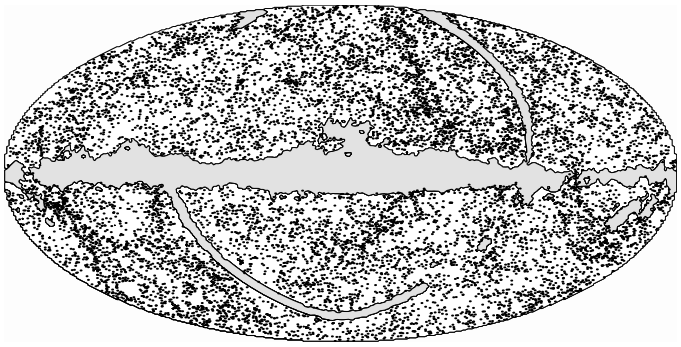

Figure 3.1: PSCz catalogue source distribution and related mask in galactic coordinates.

with enough sensitivity by the IRAS satellite (see Fig. 3.1). These regions are excluded from our analysis with the use of the binary mask available with the PSCz catalogue itself.

3.2.2 The Selection Function

No available galaxy catalogue is complete in volume and therefore completeness estimates derived from the selection effects in flux are needed. More in detail, the relevant quantity to be derived is the fraction of galaxies actually observed at the various redshifts, a quantity also known as the *redshift selection function* $\phi(z)$ [145]. A convenient way to express $\phi(z)$ is in terms of the galaxy luminosity function (i.e. the distribution of galaxy luminosities) $\Phi(L)$ as

$$\phi(z) = \frac{\int_{L_{\min}(z)}^{\infty} \mathrm{d}\, L\ \Phi(L)}{\int_{0}^{\infty} \mathrm{d}\, L\ \Phi(L)}. \tag{3.1}$$

Here $L_{\min}(z)$ is the minimum luminosity detected by the survey in function of redshift. By definition, for a flux-limited survey of limiting flux $f_{\lim}$, $L_{\min}(z)$ is given in terms of the luminosity distance $d_L(z)$ as

$$L_{\min}(z) = 4\pi d_L^2(z) f_{\lim}. \tag{3.2}$$

The luminosity distance depends on the cosmology assumed, though for small redshifts ($z \lesssim 0.1$) it can be approximated by $d_L(z) \simeq z/H_0$.

Generally $\phi(z)$ is inferred from the catalogue data itself in a self-consistent way, using the observational galaxy luminosity distribution to estimate $\Phi(L)$ [140; 146; 147]. The quantity $n(z)/\phi(z)$ represents the experimental distribution corrected for the selection effects, which must be used in the computations. A detailed discussion of this issue can be found in Ref. [148]. Furthermore, we

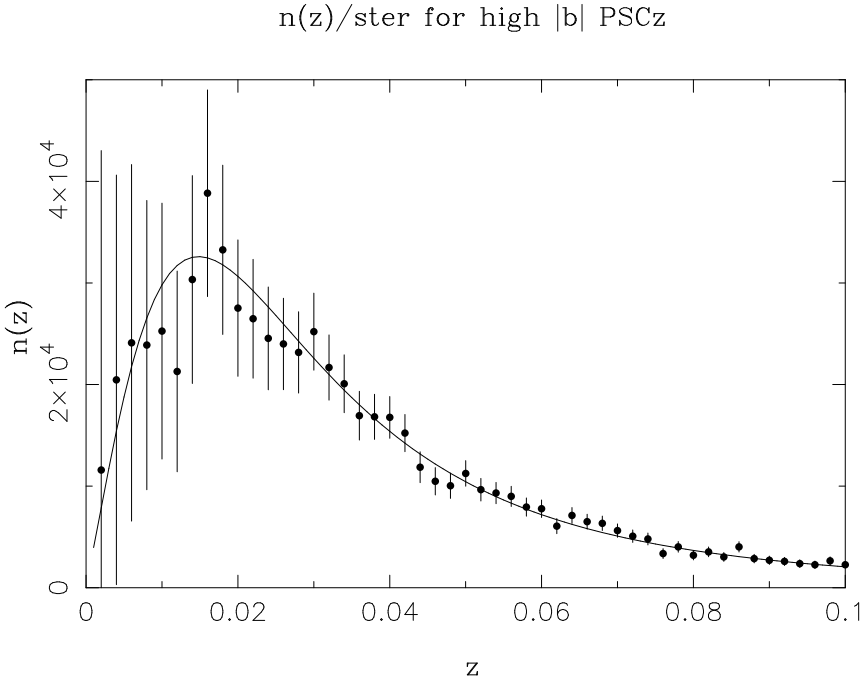

Figure 3.2: Experimental redshift distribution of the PSCz catalogue galaxies and prediction for an homogeneous universe from the selection function $\phi(z)$ (from [140]); both are normalized in order to represent the number of sources per unit of redshift per steradian.

wish to stress that up to $z \sim 0.1$ evolution effects are negligible and the local universe galaxy luminosity function can be safely used. In the case of deeper surveys like SDSS, cosmological effects cannot be neglected and our approach can still be employed even though a series of corrections, like evolutionary effects or scale-dependent luminosity, must be taken into account [149]. These corrections are needed since luminous galaxies, which dominate the sample at large scales, cluster more than faint ones [150]. In the case of the PSCz catalogue the selection function is given as [140]

$$\phi(r) = \phi_* \left(\frac{r}{r_*}\right)^{1-\alpha} \left[1 + \left(\frac{r}{r_*}\right)^{\gamma}\right]^{-\left(\frac{\beta}{\gamma}\right)}, \tag{3.3}$$

with the parameters $\phi_* = 0.0077, \alpha = 1.82, r_* = 86.4, \gamma = 1.56, \beta = 4.43$ that respectively describe the normalization, the nearby slope, the break distance in h^{-1}Mpc, its sharpness and the additional slope beyond the break (see also Fig. 3.2).

It is clear, however, that even taking into account the selection function we cannot use the catalogue up to the highest redshifts ($z \simeq 0.3$), due to the

rapid loss of statistics. At high z, in fact, the intrinsic statistical fluctuation due to the selection effect starts to dominate over the true matter fluctuations, producing artificial clusterings not corresponding to real structures ("shot noise" effect). This problem is generally treated constructing from the point sources catalogue a smoothed density field $\rho(\hat{\Omega}, z)$ with a variable smoothing length that effectively increases with redshift, remaining always of size comparable to the mean distance on the sphere of the sources of the catalogue. We minimize this effect by being conservative in setting the maximum redshift at $z = 0.06$ (corresponding to $180\,h^{-1}$Mpc) where we have still good statistics while keeping the shot noise effect under control. With this threshold we are left with $\sim 11,500$ sources of the catalogue. Furthermore, for the purposes of present analysis, the weight of the sources rapidly decreases with redshift due to the energy losses induced by the GZK effect. In the energy range $E \geq 5\times10^{19}$ eV, the contribution from sources beyond $z \simeq 0.06$ is sub-dominant, thus allowing to assume for the objects beyond $z = 0.06$ an effective isotropic source contribution.

3.3 The Formalism

In the following we describe in some detail the steps involved in our formalism. In Sec. 3.3.1 we summarize our treatment for energy losses, in Sec. 3.3.2 the way the "effective" UHECR map is constructed, and in Sec. 3.3.3 the statistical analysis we perform.

3.3.1 UHECRs Propagation

The first goal of our analysis is to obtain the underlying probability distribution $f_{\rm LSS}(\hat{\Omega}, E)$ to have a UHECR with energy higher than E from the direction $\hat{\Omega}$. For simplicity here and throughout the chapter we shall assume that each source of our catalogue has the same probability to emit a UHECR, according to some spectrum at the source $g(E_i)$. In principle, one would expect some correlation of this probability with one or more properties of the source, like its star formation rate, radio-emission, size, etc. The authors of Ref. [139] tested for a correlation $L_{\rm UHECR} \propto L_{\rm FIR}^{\kappa}$, $L_{\rm UHECR}$ being the luminosity in UHECRs and $L_{\rm FIR}$ the one in far-infrared region probed in IRAS catalogue. The results of their analysis do not change appreciably as long as $0 \lesssim \kappa \lesssim 1$. We can then expect that our limit of $\kappa = 0$ might well work for a broader range in parameter space, but this is not of much concern here, since we do not stick to specific models for UHECR sources. The method we discuss can be however easily generalized to such a case, and eventually also

to a multi-parametric modelling of the correlation.

In an ideal world where a volume-complete catalogue were available and no energy losses for UHECRs were present, each source should then be simply weighted by the geometrical flux suppression $\propto d_L^{-2}$. The selection function already implies the change of the weight into $\phi^{-1}d_L^{-2}$. Moreover, while propagating to us, high-energy protons lose energy as a result of the cosmological redshift and of the production of $e^{\pm}$ pairs and pions (the dominant process) caused by interactions with CMB. For simplicity, we shall work in the continuous loss approximation [151]. Then, a proton of energy E_i at the source at $z = z_i$ will be degraded at the Earth ($z = 0$) to an energy E_f given by the energy-loss equation*

$$\frac{1}{E}\frac{dE}{dz} = -\frac{dt}{dz}\times(\beta_{\rm rsh} + \beta_\pi + \beta_{e^\pm}). \tag{3.4}$$

Eq.(3.4) has to be integrated from z_i, where the initial Cauchy condition $E(z = z_i) = E_i$ is imposed, to $z = 0$. The different terms in Eq. (3.4) are explicitly shown below

$$\begin{aligned}
-\frac{dt}{dz} &= [(1+z)H_0\sqrt{(1+z)^3\Omega_M + \Omega_\Lambda}]^{-1}, && (3.5)\\
\beta_{\rm rsh}(z) &= H_0\sqrt{(1+z)^3\Omega_M + \Omega_\Lambda}, && (3.6)\\
\beta_\pi(z,E) &\simeq C_\pi(1+z)^3, \;\; E \geq E_{\rm match} && (3.7)\\
&\quad A_\pi(1+z)^3 e^{-\frac{B_\pi}{E(1+z)}}, \;\; E \leq E_{\rm match} && (3.8)\\
\beta_{e^\pm}(z,E) &\simeq \frac{\alpha^3 Z^2}{4\pi^2}\frac{m_e^2 m_p^2}{E^3}\int_2^\infty {\rm d}\xi \frac{\varphi(\xi)}{\exp[\frac{m_e m_p \xi}{2ET_0(1+z)}] - 1}, && (3.9)
\end{aligned}$$

where we assume for the Hubble constant $H_0 = 71^{+4}_{-3}$ km/s/Mpc, and $\Omega_M \simeq 0.27$ and $\Omega_\Lambda \simeq 0.73$ are the matter and cosmological constant densities in terms of the critical one [152]. In the previous formulae, m_e and m_p are respectively the electron and proton masses, T_0 is the CMB temperature, and α the fine-structure constant. Since we are probing the relatively near universe, the results will not depend much from the cosmological model adopted, but mainly on the value assumed for H_0. More quantitatively, the r.h.s of Eq. (3.4) changes linearly with H_0^{-1} (apart for the negligible term $\beta_{\rm rsh}$), while even an extreme change from the model ($\Omega_M = 0.27$; $\Omega_\Lambda = 0.73$) to ($\Omega_M = 1$; $\Omega_\Lambda = 0.0$) (the latter ruled out by present data) would only modify the energy loss term by 6% at $z \simeq 0.06$, the highest redshift we consider.

*We are neglecting diffuse backgrounds other than CMB and assuming straight-line trajectories, consistently with the hypothesis of weak EGMF.

The values $\{A_\pi, B_\pi, C_\pi\} = \{3.66\times10^{-8}\mathrm{yr}^{-1}, 2.87\times10^{20}\,\mathrm{eV}, 2.42\times10^{-8}\mathrm{yr}^{-1}\}$ as well as the parameterization for β_π as well as are taken from [153], and $E_{\rm match}(z) = 6.86\,e^{-0.807\,z}\times10^{20}\,\mathrm{eV}$ is used to ensure continuity to $\beta_\pi(z, E)$. An useful parameterization of the auxiliary function $\varphi(\xi)$ can be found in [154], which we follow for the treatment of the pair production energy loss. In practice, we have evolved cosmic rays over a logarithmic grid in E_i from 10^{19} to 10^{23} eV, and in z from 0.001 to 0.3. The values at a specific source site has been obtained by a smooth interpolation.

Note that in our calculation i) the propagation is performed to attribute an "energy-loss weight" to each z in order to derive a realistic probability distribution $f_{\rm LSS}(\hat{\Omega}, E)$; ii) we are going to "smooth" the results over regions of several degrees in the sky (see below), thus performing a sort of weighted average over redshifts as well. Since this smoothing effect is by far dominant over the single source stochastic fluctuation induced by pion production, the average effect accounted for by using a continuous energy-loss approach is a suitable approximation.

In summary, the propagation effects provide us a "final energy function" $E_f(E_i, z)$ giving the energy at Earth for a particle injected with energy E_i at a redshift z. Note that, being the energy-loss process obviously monotone, the inverse function $E_i(E_f, z)$ is also available.

3.3.2 Map Making

Given an arbitrary injection spectrum $g(E_i)$, the observed events at the Earth would distribute, apart for a normalization factor, according to the spectrum $g(E_i(E_f, z))dE_i/dE_f$. In particular we will consider in the following a typical power-law $g(E_i) \propto E_i^{-s}$, but this assumption may be easily generalized. Summing up on all the sources in the catalogue one obtains the expected differential flux map on Earth

$$F(\hat{\Omega}, E_f) \propto \sum_k \frac{1}{\phi(z_k)} \frac{\delta(\hat{\Omega} - \hat{\Omega}_k)}{4\pi d_L^2(z_k)} E_i^{-s}(E_f, z_k) \frac{dE_i}{dE_f}(E_f, z_k), \tag{3.10}$$

where the selection function and distance flux suppression factors have been taken into account. However, given the low statistics of events available at this high energies, a more useful quantity to employ is the integrated flux above some energy threshold $E_{\rm cut}$, that can be more easily compared with the integrated UHECR flux above the cut $E_{\rm cut}$. Integrating the previous

expression we have

$$f_{\rm LSS}(\hat{\Omega}, E_{\rm cut}) \propto \sum_k \frac{1}{\phi(z_k)} \frac{\delta(\hat{\Omega}-\hat{\Omega}_k)}{4\pi d_L^2(z_k)} \int_{E_i(E_{\rm cut},z_k)}^{\infty} E^{-s} {\rm d}E$$
$$= \sum_k f_{\rm LSS}(k)\ \delta(\hat{\Omega}-\hat{\Omega}_k), \qquad (3.11)$$

that can be effectively seen as if at every source k of the catalogue it is assigned a weight $f_{\rm LSS}(k)$ that takes into account geometrical effects (d_L^{-2}), selection effects (ϕ^{-1}), and physics of energy losses through the integral in ${\rm d}E$. In this "GZK integral" the upper limit of integration is taken to be infinite, though the result is practically independent from the upper cut used provided it is much larger than 10^{20} eV.

It is interesting to compare the similar result expected for an uniform source distribution with constant density; in this case we have (in the limit $z \ll 1$)

$$f_{\rm LSS}(\hat{\Omega}, E_{\rm cut}) \propto \int {\rm d}z \frac{[E_i(E_{\rm cut}, z)]^{-s+1}}{s-1} \equiv \int {\rm d}z\, p(z, E_{\rm cut}, s), \qquad (3.12)$$

where the integral in ${\rm d}E$ has been explicitly performed and the flux suppression weight is cancelled by the geometrical volume factor. The integrand $p(z, E_{\rm cut}, s)$ containing the details of the energy losses also provides an effective cut at high z. The integrand —when normalized to have unit area— can be interpreted as the distribution of the injection distances of CR observed at the Earth. It also suggests the definition of the so-called "GZK sphere" as the sphere from which originates most (say 99%) of the observed CR flux on Earth above an energy threshold $E_{\rm cut}$. In Fig. 3.3 we plot the distribution p for different values of $E_{\rm cut}$ and s. We see that around a particular threshold $z_{\rm GZK}$ the distribution falls to zero: the dependence of $z_{\rm GZK}$ on $E_{\rm cut}$ is quite critical as expected, while there is also a softer dependence on s. This suggests naturally the choice $E_{\rm cut} = 5{\times}10^{19}$ eV for the chosen value $z_{\rm GZK} \simeq 0.06$; at the same time, the energy cut chosen is not too restrictive, ensuring indeed that a significant statistics might be achieved in a few years. For this $E_{\rm cut}$ the isotropic contribution to the flux is sub-dominant; however we can take it exactly into account and the weight of the isotropic part is given by[†]

$$w_{\rm iso} \propto \int_{z_{\rm GZK}}^{\infty} {\rm d}z\, p(z, E_{\rm cut}). \qquad (3.13)$$

[†]The normalization factor is fixed consistently with Eqs. (3.11)-(3.12).

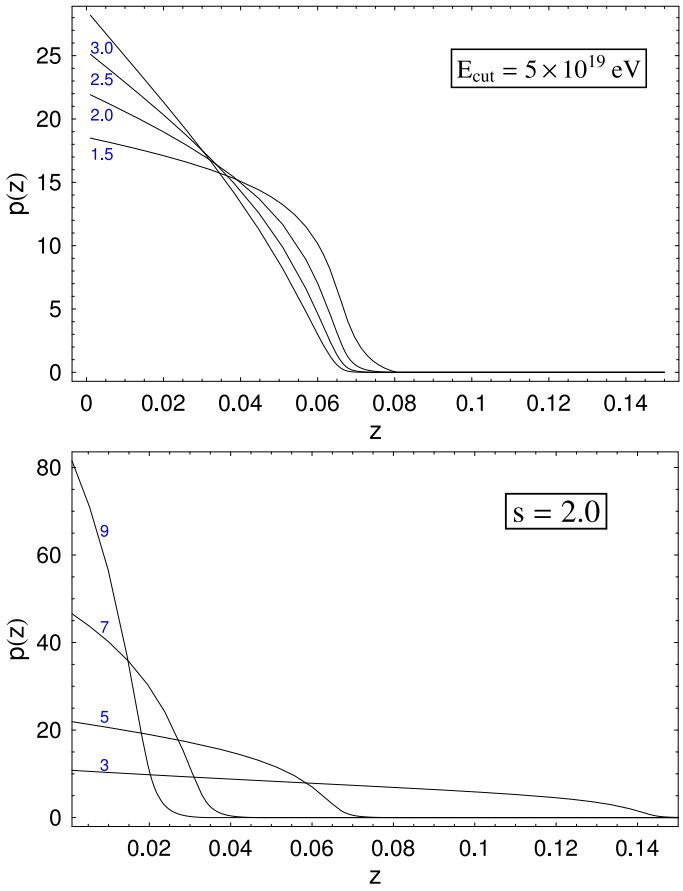

Figure 3.3: Distribution of the injection distances of CR observed at the Earth for fixed $E_{\rm cut} = 5{\times}10^{19}$ eV (top) and $s = 1.5, 2.0, 2.5, 3.0$ and for fixed spectral index $s = 2.0$ (bottom) and varying $E_{\rm cut} = 3, 5, 7, 9{\times}10^{19}$ eV. The area subtended by $p(z)$ has been normalized to unity.

Finally, to represent graphically the result, the spike-like map (3.11) is effectively smoothed through a gaussian filter as

$$f_{\rm LSS}(\hat{\Omega}, E_{\rm cut}) \propto \sum_k f_{\rm LSS}(k) \exp\left(-\frac{d_s^2[\hat{\Omega}, \hat{\Omega}_k]}{2\sigma^2}\right) + \frac{w_{\rm iso}}{4\pi} 2\pi\sigma^2 \mu(\hat{\Omega}). \qquad (3.14)$$

In the previous equation, σ is the width of the gaussian filter, d_s is the spherical distance between the coordinates $\hat{\Omega}$ and $\hat{\Omega}_k$, and $\mu(\hat{\Omega})$ is the catalogue mask (see Section 3.2.1) such that $\mu(\hat{\Omega}) = 0$ if $\hat{\Omega}$ belongs to the mask region and $\mu(\hat{\Omega}) = 1$ otherwise.

3.3.3 Statistical Analysis

Given the extremely poor UHECR statistics, we limit ourselves to address the basic issue of determining the minimum number of events needed to significatively reject "the null hypothesis". To this purpose, it is well known that a χ^2-test is an extremely good estimator. Notice that a χ^2-test needs a binning of the events, but differently from the K-S test performed in [139] or the Smirnov-Cramer-von Mises test of [138], it has no ambiguity due to the 2-dimensional nature of the problem, and indeed a similar approach was used in [136]. A criterion guiding in the choice of the bin size is the following: with N UHECRs events available and M bins, one would expect $\mathcal{O}(N/M)$ events per bin; to allow a reliable application of the χ^2-test, one has to impose $N/M \geq 10$. Each cell should then cover at least a solid angle of $\Delta_M \sim 10\times\Delta_{\rm tot}/N$, $\Delta_{\rm tot}$ being the solid angle accessible to the experiment. For $\Delta_{\rm tot} \sim 2\pi$ (50% of full sky coverage), one estimates a square window of side $454^\circ/\sqrt{N}$, i.e. 45° for 100 events, 14° for 1000 events. Since the former number is of the order of present world statistics, and the latter is the achievement expected by Auger in several years of operations, a binning in windows of size 15° represents quite a reasonable choice for our forecast. This choice is also suggested by the typical size of the observable structures, a point we will comment further at the end of this Section. Notice that the GMF, that induces at these energies typical deflections of about 4° [84], can be safely neglected for this kind of analysis. The same remark holds for the angular resolution of the experiment.

Obviously, for a specific experimental set-up one must include the proper exposure $\omega_{\rm exp}$, to convolve with the previously found $f_{\rm LSS}$. The function $\omega_{\rm exp}$ depends on the declination δ, right ascension RA, and, in general, also on the energy. For observations having uniform coverage in RA, like AGASA or Auger ground based arrays, one can easily parameterize the relative exposure as [155]

$$\omega_{\rm exp}(\delta) \propto \cos\theta_0 \sin\alpha_m \cos\delta + \alpha_m \sin\theta_0 \sin\delta, \tag{3.15}$$

where θ_0 is the latitude of the experiment ($\theta_0 \approx -35^\circ$ for Auger South), α_m is given by

$$\alpha_m = \begin{cases} 0\,, & \text{if } \xi > 1 \\ \pi\,, & \text{if } \xi < -1 \\ \cos^{-1}\xi\,, & \text{otherwise} \end{cases} \tag{3.16}$$

and

$$\xi \equiv \frac{\cos\theta_{\rm max} - \sin\theta_0 \ \sin\delta}{\cos\theta_0 \ \ \cos\delta}\ , \tag{3.17}$$

$\theta_{\rm max}$ being the maximal zenith angle cut applied (we assume $\theta_{\rm max} = 60^\circ$ for

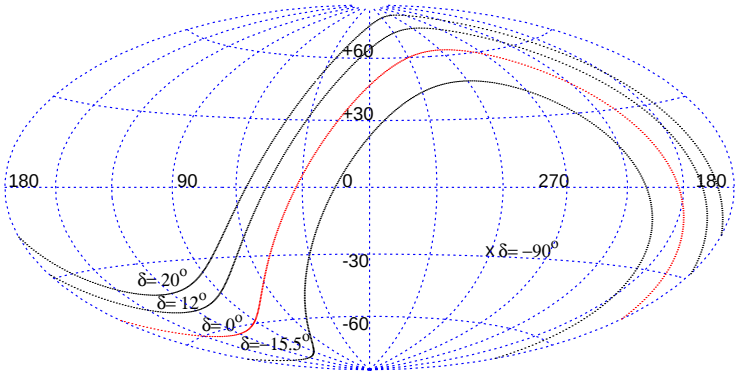

Figure 3.4: Galactic coordinate reference frame and contours enclosing 68%, 95% and 99% of the Auger exposure function, with the corresponding declinations. The celestial equator ($\delta = 0°$) and south pole ($\delta = -90°$) are also shown.

Auger). Contour plots for the Auger exposure function in galactic coordinates are shown in Fig. 3.4.

For a given experiment and catalogue, the null hypothesis we want to test is that the events observed are sampled —apart from a trivial geometrical factor— according to the distribution $f_{\rm LSS}\,\omega_{\rm exp}\,\mu$. Since we are performing a forecast analysis, we will consider test realizations of N events sampled according to a random distribution on the (accessible) sphere, i.e. according to $\omega_{\rm exp}\,\mu$, and determine the confidence level (C.L.) with which the hypothesis is rejected as a function of N. For each realization of N events we calculate the two functions

$$\mathcal{X}^2_{\rm iso}(N) = \frac{1}{M-1}\sum_{i=1}^{M}\frac{(o_i - \epsilon_i[f_{\rm iso}])^2}{\epsilon_i[f_{\rm iso}]}, \tag{3.18}$$

$$\mathcal{X}^2_{\rm LSS}(N) = \frac{1}{M-1}\sum_{i=1}^{M}\frac{(o_i - \epsilon_i[f_{\rm LSS}])^2}{\epsilon_i[f_{\rm LSS}]}, \tag{3.19}$$

where o_i is the number of "random" counts in the i-th bin Ω_i, and $\epsilon_i[f_{\rm LSS}]$ and $\epsilon_i[f_{\rm iso}]$ are the theoretically expected number of events in Ω_i respectively

for the LSS and isotropic distribution. In formulae (see Eq. (3.11)),

$$\epsilon_i[f_{\rm LSS}] = N\alpha \frac{\sum_{j\in\Omega_i} f_{\rm LSS}(j)\omega_{\rm exp}(\delta_j)\mu(j) + w_{\rm iso}/4\pi\, S[\Omega_i]}{\sum_j f_{\rm LSS}(j)\omega_{\rm exp}(\delta_j)\mu(j) + w_{\rm iso}/4\pi\, S_\omega}, \quad (3.20)$$

$$\epsilon_i[f_{\rm iso}] = N\alpha \frac{S[\Omega_i]}{S_\omega}, \quad (3.21)$$

where $S[\Omega_i] = \int_{\Omega_i} d\Omega\, \omega_{\rm exp}\mu$ is the spherical surface (exposure- and mask-corrected) subtended by the angular bin Ω_i, and similarly $S_\omega = \int_{4\pi} d\Omega\, \omega_{exp}\mu$. The mock data set is then sampled $\mathcal{N}$ times in order to establish empirically the distributions of $\mathcal{X}^2_{\rm LSS}$ and $\mathcal{X}^2_{\rm iso}$, and the resulting distribution is studied as function of N (plus eventually $s, E_{\rm cut}$, etc.). The parameter

$$\alpha \equiv \frac{\int d\Omega\ \omega_{exp}(\delta)\mu(\Omega)}{\int d\Omega\ \omega_{exp}(\delta)} \quad (3.22)$$

is a mask-correction factor that takes into account the number of points belonging to the mask region and excluded from the counts o_i. Note that the random distribution is generated with N events in all the sky view of the experiment, but, effectively, only the region outside the mask is included in the statistical analysis leaving us with effective $N\alpha$ events to study. This is a limiting factor due to quality of the catalogue: With a better sky coverage the statistics is improved and the number of events required to asses the model can be reduced.

As our last point, we return to the problem of choice of the bin size. To assess its importance we studied the dependence of the results on this parameter. For a cell side larger than about $\sim 25^\circ$ the analysis loses much of its power, and a very high N is required to distinguish the models and obtain meaningful conclusions. This is somewhat expected looking at the map results that we obtain, where typical structures have dimensions of the order $15^\circ - 20^\circ$. A greater cell size results effectively in a too large smoothing and a consequent lost of information. On the other hand, a cell size below $4^\circ - 6^\circ$ makes the use of a χ^2 analysis not very reliable, because of the low number of events in each bin expected for realistic exposure times. In the quite large interval $\sim 6^\circ - 20^\circ$ for the choice of the cell size, however, the result is almost independent of the bin size, that makes us confident on the reliability of our conclusions.

3.4 Results

In Fig. 3.5 we plot the smoothed maps in galactic coordinates of the expected integrated flux of UHECRs above the energy threshold $E_{\rm cut} = 3, 5, 7, 9\times10^{19}$ eV

and for slope parameter $s = 2.0$; the isotropic part has been taken into account and the ratio of the isotropic to anisotropic part $w_{\rm iso}/\sum_k f_{\rm LSS}(k)$ is respectively $83\%, 3.6\%, \ll 1\%, \ll 1\%$.

Only for $E_{\rm cut} = 3{\times}10^{19}\,{\rm eV}$ the isotropic background constitutes then a relevant fraction, since the GZK suppression of far sources is not yet present. For the case of interest $E_{\rm cut} = 5{\times}10^{19}\,{\rm eV}$ the contribution of $w_{\rm iso}$ is almost negligible, while it practically disappears for $E_{\rm cut} \gtrsim 7{\times}10^{19}\,{\rm eV}$. Varying the slope for $s = 1.5, 2.0, 2.5, 3.0$ while keeping $E_{\rm cut} = 5{\times}10^{19}\,{\rm eV}$ fixed produces respectively the relative weights $8.0\%, 3.6\%, 1.8\%, 0.9\%$, so that only for very hard spectra $w_{\rm iso}$ would play a non-negligible role (see also Fig. 3.3).

Due to the GZK-effect, as it was expected, the nearest structures are also the most prominent features in the maps. The most relevant structure present in every slide is the Local Supercluster. It extends along $l \simeq 140^\circ$ and $l \simeq 300^\circ$ and includes the Virgo cluster at $l = 284^\circ, b = +75^\circ$ and the Ursa Major cloud at $l = 145^\circ, b = +65^\circ$, both located at $z \simeq 0.01$. The lack of structures at latitudes from $l \simeq 0^\circ$ to $l \simeq 120^\circ$ corresponds to the Local Void. At higher redshifts the main contributions come from the Perseus-Pisces supercluster ($l = 160^\circ, b = -20^\circ$) and the Pavo-Indus supercluster ($l = 340^\circ, b = -40^\circ$), both at $z \sim 0.02$, and the very massive Shapley Concentration ($l = 250^\circ, b = +20^\circ$) at $z \sim 0.05$. For a more detailed list of features in the map, see the key in Fig. 3.6.

The $E_{\rm cut}$-dependence is clearly evident in the maps: as expected, increasing $E_{\rm cut}$ results in a map that closely reflects the very local universe (up to $z \sim 0.03 - 0.04$) and its large anisotropy; conversely, for $E_{\rm cut} \simeq 3,4{\times}10^{19}\,{\rm eV}$, the resulting flux is quite isotropic and the structures emerge as fluctuations from a background, since the GZK suppression is not yet effective. This can be seen also comparing the near structures with the most distant ones in the catalogue: while the Local Supercluster is well visible in all slides, the signal from the Perseus-Pisces super-cluster and the Shapley concentration is of comparable intensity only in the two top panels, while becoming highly attenuated for $E_{\rm cut} = 7{\times}10^{19}\,{\rm eV}$, and almost vanishing for $E_{\rm cut} = 9{\times}10^{19}\,{\rm eV}$. A similar trend is observed for increasing s at fixed $E_{\rm cut}$, though the dependence is almost one order of magnitude weaker. Looking at the contour levels in the maps we can have a precise idea of the absolute intensity of the "fluctuations" induced by the LSS; in particular, for the case of interest of $E_{\rm cut} = 5{\times}10^{19}\,{\rm eV}$ the structures emerge only at the level of 20%-30% of the total flux, the 68% of the flux actually enclosing almost all the sky. For $E_{\rm cut} = 7,9{\times}10^{19}\,{\rm eV}$, on the contrary, the local structures are significantly more pronounced, but in this case we have to face with the low statistics available at this energies. Then in a low-statistics regime it's not an easy task to disentangle the LSS and the isotropic distributions.

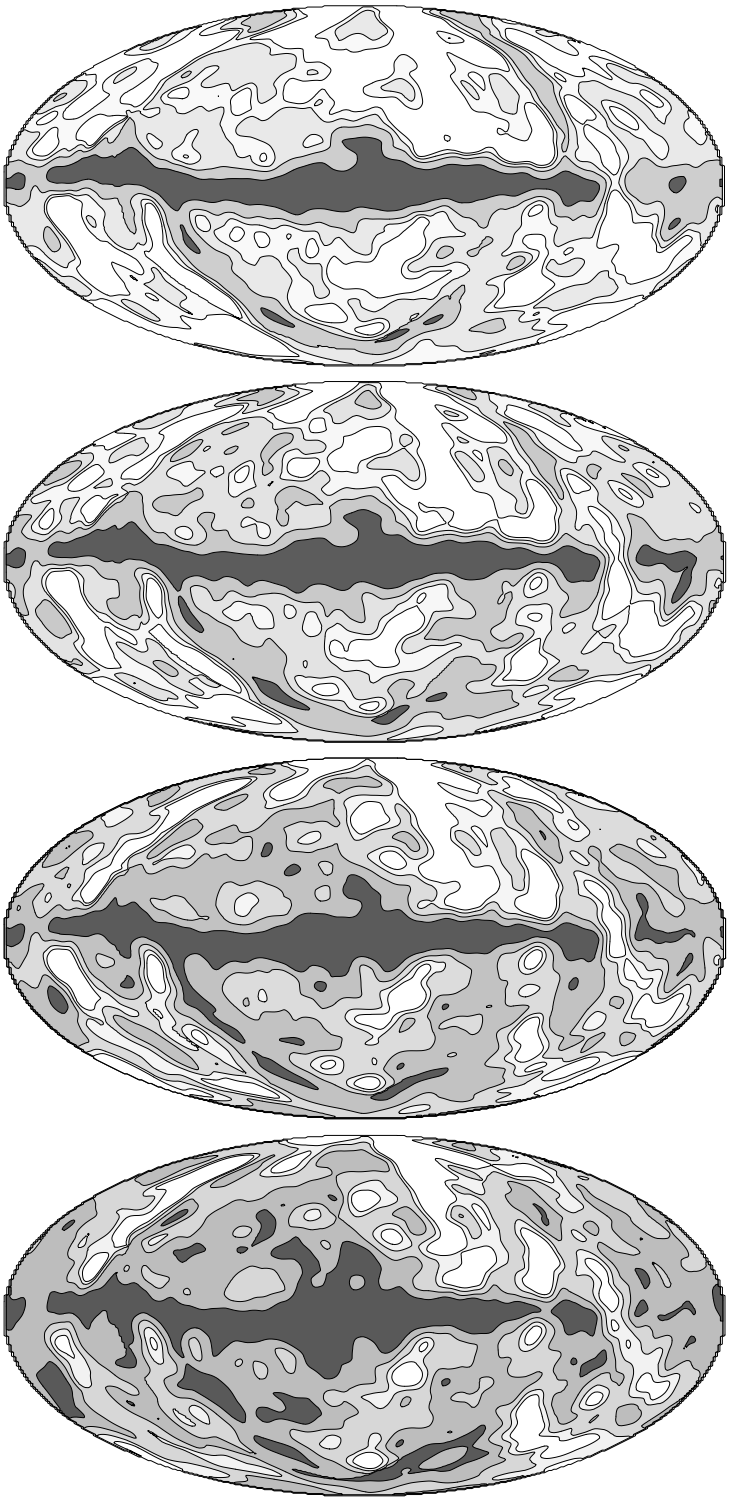

Figure 3.5: Equal area Hammer-Aitoff projections of the smoothed UHECRs arrival directions distribution (Eq. (3.14)) in galactic coordinates obtained for fixed $s = 2.0$ and, from the upper to the lower panel, for $E_{\rm cut} = 3, 5, 7, 9\times10^{19}$ eV. The smoothing angle is $\sigma = 3^\circ$. The contours enclose 95%, 68%, 38%, 20% of the corresponding distribution.

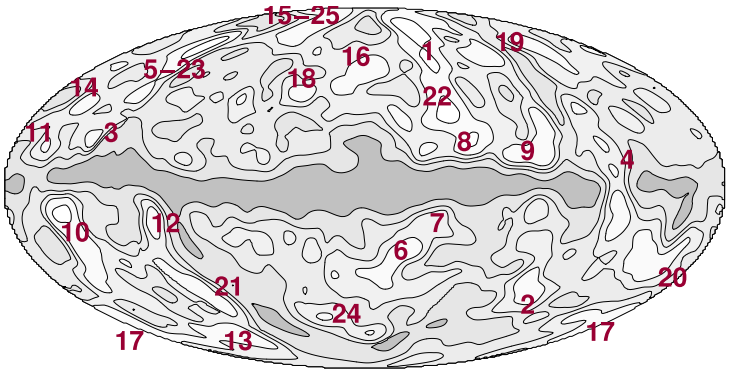

Figure 3.6: Detailed key of the structures visible in the UHECR maps; arbitrary contour levels. Labels correspond to: (1) Southern extension of Virgo and Local Supercluster; (2)Fornax-Eridani Cluster; (3) Cassiopea Cluster; (4) Puppis Cluster; (5) Ursa Major Cloud; (6-7) Pavo-Indus and "Great Attractor" region; (8) Centaurus Super-Cluster; (9) Hydra Super-Cluster; (10) Perseus Super-Cluster; (11) Abell 569; (12) Pegasus Cluster; (13-17) Pisces Cluster; (14) Abell 634; (15) Coma Cluster; (16-18) Hercules Supercluster; (19) Leo Supercluster; (20) Columba Cluster; (21) Cetus Cluster; (22) Shapley Concentration; (23) Ursa Major Supercluster; (24) Sculptor Supercluster; (25) Bootes Supercluster.

The structures which are more likely to be detected by Auger (see also Fig. 3.4) are the Shapley concentration, the Southern extension of the Virgo cluster, the Local Supercluster and the Pavo-Indus super-cluster. Other structures, such as the Perseus-Pisces supercluster and the full Virgo cluster are visible only from the Northern hemisphere and are therefore within the reach of experiments like Telescope Array [45], or the planned North extension of the Pierre Auger Observatory. Moreover, the sky region obscured by the heavy extinction in the direction of the Galactic Plane reflects a lack of information about features possibly “hidden” there. Unfortunately, this

$N \setminus s$	1.5	2.0	2.5	3.0
50	(42:6)	(47:8)	(52:10)	(52:10)
100	(55:9)	(60:12)	(66:14)	(69:16)
200	(72:27)	(78:33)	(84:40)	(86:43)
400	(92:61)	(95:72)	(97:80)	(98:83)
600	(98:85)	(99:91)	(100:96)	(100:97)
800	(100:95)	(100:98)	(100:99)	(100:100)
1000	(100:98)	(100:100)	(100:100)	(100:100)

Table 3.1: The probability (in %) to reject the isotropic hypothesis at (90%:99%) C.L. when UHECRs follow the LSS distribution, as a function of the injection spectral index and of the observed number of events, fixing $E_{\rm cut} = 5{\times}10^{19}$ eV.

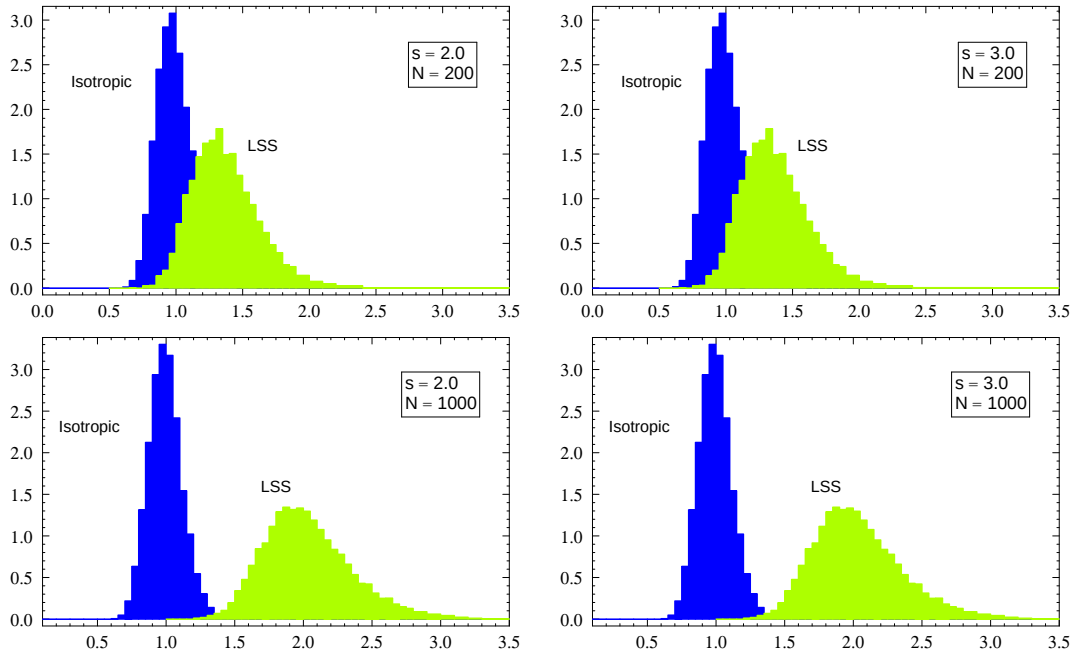

Figure 3.7: The probability distributions of the estimators $\mathcal{X}^2_{\rm iso}$ and $\mathcal{X}^2_{\rm LSS}$ for the cases $s = 2.0, 3.0$ and for $N = 200, 1000$ events, fixing $E_{\rm cut} = 5{\times}10^{19}$ eV. The distribution are the results of 10000 monte-carlo simulation like described in the text.

region falls just in the middle of the Auger field of view, thus reducing —for a given statistics N— the significance of the check of the null hypothesis. Numerically, this translates into a smaller value of the factor α of Eq. (3.22) with respect to an hypothetical "twin" Northern Auger experiment.

A quantitative statistical analysis confirms previous qualitative considerations. In Table 3.1 we report the probability to reject the isotropic hypothesis at 90% and 99% C.L. when UHECRs follow the LSS distribution, as a function of the injection spectral index and of the observed number of events, fixing $E_{\rm cut} = 5{\times}10^{19}$ eV. In Figure 3.7 we show the distributions of the functions $\mathcal{X}^2_{\rm iso}$ and $\mathcal{X}^2_{\rm LSS}$ introduced in the previous section for $s = 2.0, 3.0$ and $N = 200, 1000$, for the same cut $E_{\rm cut} = 5{\times}10^{19}$ eV. It is clear that a few hundreds events are hardly enough to reliably distinguish the two models, while $N = 800$–1000 should be more than enough to reject the hypothesis at 2-3 σ, independently of the injection spectrum. Steeper spectra however slightly reduce the number of events needed for a given C.L. discrimination. It is also interesting to note that, using different techniques and unconstrained LSS simulations, it was found that a comparable statistics is needed to probe a magnetized local universe [79]. It is worthwhile stressing that our conclusions

should be looked as conservative, since only proton primaries have been assumed, and constant source properties. Variations in individual source power and a mixed composition could increase the "cosmic variance" and make more difficult to distinguish among models for the source distribution [79].

With respect to previous literature on the subject, our analysis is the closest to the one of Ref. [136]. Apart for technical details, the greatest differences with respect to this work arise because of the improved determination of crucial parameters undergone in the last decade. Just to mention a few, the Hubble constant used in [136] was 100 km s^{-1} Mpc^{-1}, against the presently determined value of 71^{+4}_{-3} km s^{-1} Mpc^{-1}: this changes by a 30% the value of the quantity $z_{\rm GZK}$ (see Sec. 3.3.2). Moreover, the catalogue [156] that was used in [136] contains about 1/3 of the objects we are considering, has looser selection criteria and larger contaminations [140]. Finally, the specific location of the Southern Auger observatory was not taken into account. All together, when considering these factors, we find quite good agreement with their results.

Some discrepancy arises instead with the results of [139], whose maps appear to be dominated by statistical fluctuations, which mostly wash away physical structures. This has probably to be ascribed to two effects, the energy cut $E_{\rm cut} = 4{\times}10^{19}$ eV and the inclusion of high redshift object (up to $z \sim 0.3$) of the catalogue [140] in their analysis. Their choice of $E_{\rm cut} = 4{\times}10^{19}$ eV implies indeed $z_{\rm GZK} \simeq 0.1$, i.e. a cutoff in a redshift range where shot noise distortions are no longer negligible. The same remarks hold for Ref. [138], which also suffers of other missing corrections [139]. Also, in both cases, the emphasis is mainly in the analysis of the already existing AGASA data than in a forecast study. Our results however clearly show that AGASA statistics —only 32 data at $E \geq 5{\times}10^{19}$ eV in the published data set [157], some of which falling inside the mask— is too limited to draw any firm conclusion on the hypothesis considered.

3.5 Summary and conclusion

In this chapter we have summarized the technical steps needed to properly evaluate the expected anisotropy in the UHECR sky starting from a given catalogue of the local universe, taking into account the selection function, the blind regions, and the energy-loss effects. By applying this method to the catalogue [140], we have established the minimum statistics needed to significatively reject the null hypothesis, in particular providing a forecast for the Auger experiment. We showed with a χ^2 approach that several hundreds data are required to start testing the model at Auger South. The

most prominent structures eventually "visible" for this experiment were also identified.

Differently from other statistical tools based e.g. on auto-correlation analysis, the approach sketched above requires an Ansatz on the source candidates. The distribution of the luminous baryonic matter considered here can be thought as a quite generic expectation deserving interest of its own, but it is also expected to correlate with many sources proposed in the literature. In any case, if many astrophysical sources are involved in UHECR production, it is likely that they should better correlate with the local baryonic matter distribution than with an isotropic background.

Until now, the lack of UHECR statistics and the inadequacy of the astronomical catalogues has seriously limited the usefulness of such a kind of analysis. However, progresses are expected in both directions in forthcoming years. From the point of view of UHECR observatories, the Southern site of Auger is almost completed, and already taking data. Working from January 2004 to June 2005, Auger has reached a cumulative exposure of 1750 km^2 sr yr, observing 10 events over $10^{19.7}$ eV=5×10^{19} eV (see the URL: `www.auger.org/icrc2005/spectrum.html`), Notice that statistical and systematic errors are still quite large, and a down-shift in the $\log_{10} E$ scale of 0.1 would for example change the previous figure to 17 events. Once completed, the total area covered will be of 3000 km^2, thus improving by one order of magnitude present statistics in a couple of years [158]. The idea to build a Northern Auger site strongly depends on the possibility to perform UHECR astronomy, for which full sky coverage is of primary importance. In any case, the Japanese-American Telescope Array in the desert of Utah is expected to become operational by 2007 [159]. It should offer almost an order of magnitude larger aperture per year than AGASA in the Northern sky, with a better control over the systematics thanks to a hybrid technique similar to the one employed in Auger.

The other big step is expected in astronomical catalogues. The 2MASS survey [141] has resolved more than 1.5 million galaxies in the near-infrared, and has been explicitly designed to provide an accurate photometric and astrometric knowledge of the nearby Universe. The observation in the near IR is particularly sensitive to the stellar component, and as a consequence to the luminous baryons. Though the redshifts of the sources have to be obtained via photometric methods, the larger error on the distance estimates (about 20% from the 3-band 2MASS photometry [142]) is more than compensated by the larger statistics. An analysis of this catalogue for UHECR purposes is in progress. Independently of large sky coverage, deep surveys like SDSS [144] undoubtedly have an important role in mapping the local universe as well. For example, the information encoded in such catalogues

can be used to validate methods —like the neural networks [160; 161; 162]— used to obtain photometric redshifts. An even better situation is expected from future projects like SDSS II (see the URL: `www.sdss.org`). Finally, a by-product of these surveys is the discovery and characterization of active galactic nuclei [163; 164], which in turn could have interesting applications in the search for the sources of UHECRs.

Chapter 4

First hints of large scale structures in the ultra-high energy sky?

The result of the recent publication [165] of a broad maximum around 25 degrees in the two-point autocorrelation function of ultra-high energy cosmic ray arrival directions has been intriguingly interpreted as the first imprint of the large scale structures (LSS) of baryonic matter in the near universe. We analyze this suggestion in light of the clustering properties expected from the PSCz astronomical catalogue of LSS. The chance probability of the signal is consistent within 2 σ with our expectations. No evidence for a significant cross-correlation of the observed events with known overdensities in the LSS is found, which may be due to the role of the galactic and extragalactic magnetic fields, and is however consistent with the limited statistics. The larger statistics to be collected by the Pierre Auger Observatory is needed to answer definitely the question.

4.1 Introduction

As summarized in sec.1.5 at the present, two different classes of models compete to explain the most energetic CR events observed. In "bottom-up" mechanisms the acceleration up to extreme energy occurs in suitable astrophysical environments, whereas in "top-down" scenarios UHECRs are produced by the decay or annihilation of super-massive relic particles in the halo of our Galaxy or by cosmological diffuse topological defects. The observation that UHECR arrival directions (in particular at energies $E \gtrsim 8 \times 10^{19}$ eV) may cluster according to the underlying large scale structure (LSS) of the universe would represent a clear evidence in favor of the "bottom-up" mechanisms, and should co-exist with the well known GZK flux suppression . The challenging and fascinating problem of determining at which energy (if any) astronomy with charged particles becomes possible is thus strictly related to the identification of the sources of UHECRs, which in turn would constrain

the galactic and extragalactic magnetic fields as well as the chemical composition of the primaries. The latter point is an important prerequisite to use UHECR data to study particle interactions at energy scales otherwise inaccessible to laboratory experiments.

Until now, the experiments of the previous generation have collected $\mathcal{O}(100)$ events above $E \gtrsim 4 - 5 \times 10^{19}$ eV, and one may wonder if any useful hint of the UHECR sources already hides in the available catalogues. In the recent publication [165], the authors found some evidence of a broad maximum of the two-point autocorrelation function of UHECR arrival directions around 25 degrees. The evidence was obtained combining the data with energies above 4×10^{19} eV (in the HiRes energy scale) of the HiRes stereo, AGASA, Yakutsk and SUGAR experiments. The different scales were adjusted *a priori* in order for the fluxes around 10^{19} eV to agree with each other, and according to the known systematics of the different experiments. This signal is not or only marginally present analyzing events of a single experiment, but becomes significant when data from several experiments are added. Both the signal itself and the exact value of the chance probability have to be interpreted with care, since the authors did not fix a priori the search and cut criteria. Although the nominal value of the chance probability for the signal to arise from random fluctuations is around 0.01%, when taking into account a penalty factor of 30 they estimated the "*true chance probability*" of the signal to be of the order of $P \sim 0.3\%$. Also, the autocorrelation signal disappears lowering the energy threshold, indicating that it is not caused solely by an incorrect combination of the exposure of different experiments. The authors suggest that, given the energy dependence of the signal and its angular scale, it might be interpreted as a first signature of the large-scale structure of UHECR sources and of intervening magnetic fields.

The aim of this chapter is to test their qualitative interpretation of the result on the light of the signal expected if UHECR data reflect the large scale structure distribution of galaxies in the nearby universe. In Ref. [166] (summarizedin the previous chapter), we have performed a forecast analysis for the Pierre Auger Observatory, to derive the minimum statistics needed to test the hypothesis that UHECRs trace the baryonic distribution in the universe. Assuming proton primaries, we found that a few hundred events at $E \gtrsim 5 \times 10^{19}$ eV are necessary at Auger to have reasonably high chances to identify the signature, independently of the details on the injection spectrum. In this chapter we calculate the expected signal in terms of the autocorrelation function as in [165] for the presently available statistics, and discuss quantitatively how well predictions based on the LSS distribution can reproduce their findings.

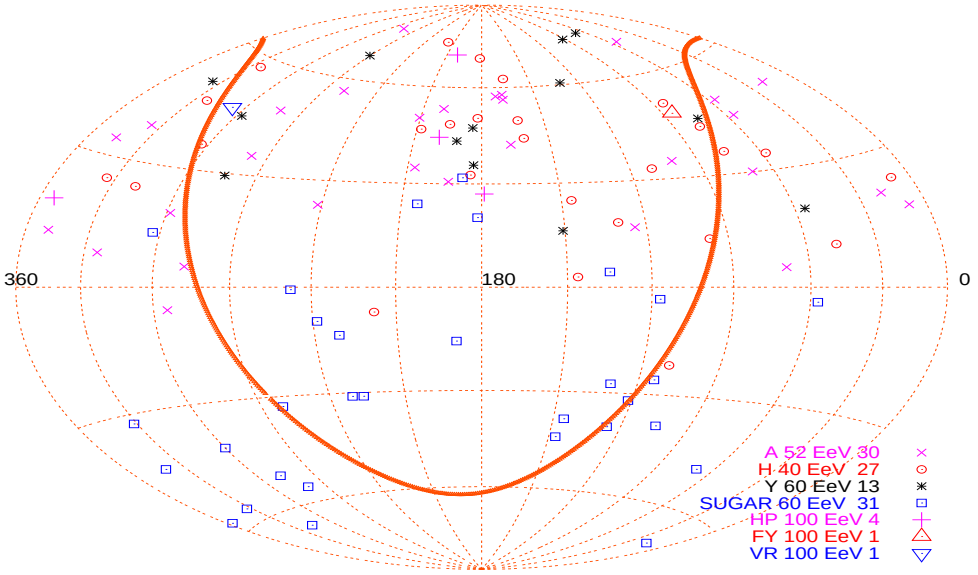

Figure 4.1: Skymap of the UHECR arrival directions of events with rescaled energy $E' > 4 \times 10^{19}$ eV in equatorial coordinates [165]; magenta crosses–30 Agasa (A) events with $E > 5.2 \times 10^{19}$ eV, red circles–27 HiRes (H) events with $E > 4 \times 10^{19}$ eV, black stars–13 Yakutsk (Y) events with $E > 6 \times 10^{19}$ eV, blue boxes–31 Sugar (S) events with $E > 6 \times 10^{19}$ eV, magenta crosses–4 Haverah Park (HP) events with $E > 10^{20}$ eV, red triangle–one Flye's Eye (FY) event with $E > 10^{20}$ eV, blue triangle–Volcano Ranch (VR) event with $E > 10^{20}$ eV.

4.2 UHECR data sets and their energy scale

In our analysis, we closely follow the approach reported in [165], which we briefly summarize here. In particular, we use: (i) the publicly available AGASA data set until May 2000, consisting of 57 events with $E > 4 \times 10^{19}$ eV and zenith angle $\vartheta < 45°$ [157]; (ii) the Yakutsk data as presented at the ICRC 2005 [167], including 34 events with energy $E > 4 \times 10^{19}$ eV and zenith angle $\vartheta < 60°$. We limit to the events within zenith angle $\vartheta < 45°$; (iii) the SUGAR data with energy above $E > 1 \times 10^{19}$ eV and zenith angle $\vartheta < 70°$ [42]; (iv) the HiRes stereo data set, with the arrival directions of the events with energy $E > 1 \times 10^{19}$ eV taken from [169], and the data set divided into events with energy $E = 1 - 2 \times 10^{19}$ eV, $E = 2 - 4 \times 10^{19}$ eV, and $E > 4 \times 10^{19}$ eV according to [170].

In order to match the flux normalization of HiRes, the energies of the AGASA data must be rescaled downwards by $\sim 30\%$, while the energies of Yakutsk and SUGAR data by $\sim 50\%$.

In Fig. 4.1, we show a skymap in equatorial coordinates of the arrival

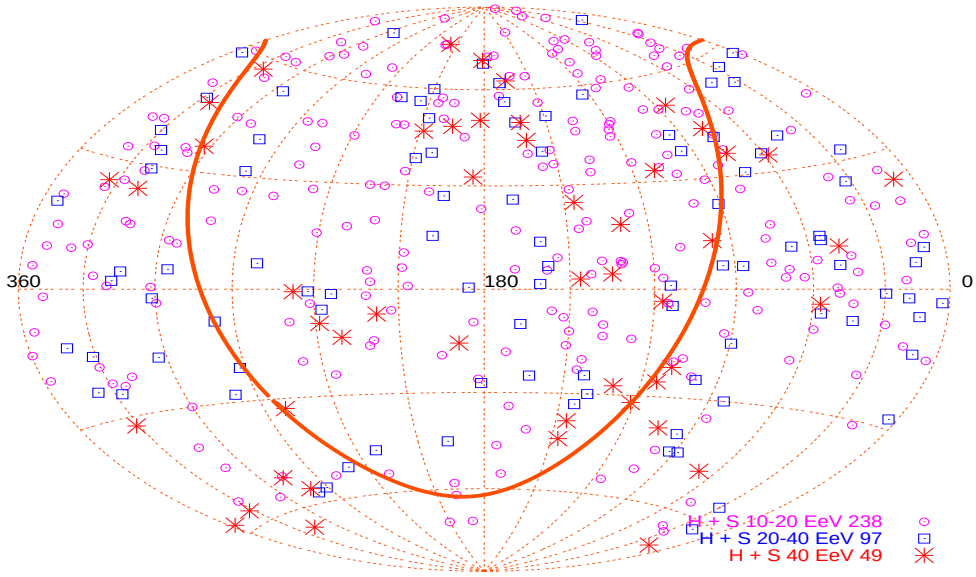

Figure 4.2: Skymap of the UHECR arrival directions in equatorial coordinates [165] from Hires and SUGAR in three different energy bins, $E = (1-2) \times 10^{19}$ (magenta, small circles), $E = (2-4) \times 10^{19}$ (blue, medium box) and $E \geq 4 \times 10^{19}$ eV (red, large stars).

directions of the UHECR used in the analysis below. An inspection by eye indicates an overdense region around and south the AGASA triplet as well as several underdense regions or voids. In Fig. 4.2, we show for comparison a skymap with events from those two experiments (Hires and SUGAR) which published also arrival directions below $E' = 4 \times 10^{19}$ eV. Again an inspection by eye indicates that the addition of low-energy data appears to make the sky map more isotropic. In the next section, we perform a statistical analysis to deduce the typical angular scales of excess correlations visible for $E' = 4 \times 10^{19}$ eV.

4.3 UHECR clustering on medium scales and LSS

We define the (cumulative) autocorrelation function w as a function of the separation angle δ as

$$w(\delta) = \sum_{i=2}^{N} \sum_{j=1}^{i-1} \Theta(\delta - \delta_{ij}), \tag{4.1}$$

where Θ is the step function, N the number of CRs considered and $\delta_{ij} = \arccos(\cos\rho_i \cos\rho_j + \sin\rho_i \sin\rho_j \cos(\phi_i - \phi_j))$ is the angular distance between the two cosmic rays i and j with coordinates (ρ, ϕ) on the sphere. We perform a large number $M \simeq 10^5$ of Monte Carlo simulations of N data sampled from an uniform distribution on the sky and for each realization j we calculate the autocorrelation function $w_j^{\rm iso}(\delta)$. The sets of random data match the number of data for the different experiments passing the cuts after rescaling, and are spatially distributed according to the exposures of the experiments. The formal probability $P(\delta)$ to observe an equal or larger value of the autocorrelation function by chance is

$$P(\delta) = \frac{1}{M} \sum_{j=1}^{M} \Theta[w_j^{\rm iso}(\delta) - w_\star(\delta)], \tag{4.2}$$

where $w_\star(\delta)$ is the observed value for the cosmic ray dataset and the convention $\Theta(0) = 1$ is being used. Relatively high values of P *and* $1 - P$ indicate that the data are consistent with the null hypothesis being used to generate the comparison samples, while low values of P *and* $1 - P$ indicates that the model is inappropriate to explain the data. Note also that by construction the values at different δ of the function $P(\delta)$ are not independent. Nonetheless, studying the cumulative distribution function (as opposed to the differential one) is the only realistic way to extract information in a low statistics "noisy" sample. In addition, an autocorrelation study—differently from the approach of Ref. [166] where a χ^2-analysis was used—only relies on the clustering probability in the data, while any directionality in the signal is lost. Although providing less compelling evidence, this method has the advantage of being more robust towards large magnetic deflections. As long as the energy and the charge of primaries from the same source are similar, their relative displacement should be small compared with the absolute displacement with respect to their sources. Thus it is natural to expect that the first (although more ambiguous) hints of a signal may come from the study of $w(\delta)$.

In Fig.4.3 the results of the correlation analysis of [165] is showed. Figure 4.4 summarizes our main results. The solid, black curve shows that under the same assumptions of Ref. [165], we obtain the same behavior for the chance probability of $w(\delta)$. To proceed further, we have to compare the previous signature with the one expected from a model of the LSS. As in [166], we use the IRAS PSCz galaxy catalogue [140]. We address to our previous work [166] as well as to the original paper [140] for technical details about the catalogue and about the calculation of the UHECR sky map—which takes into account energy losses as well—that we use in the following.

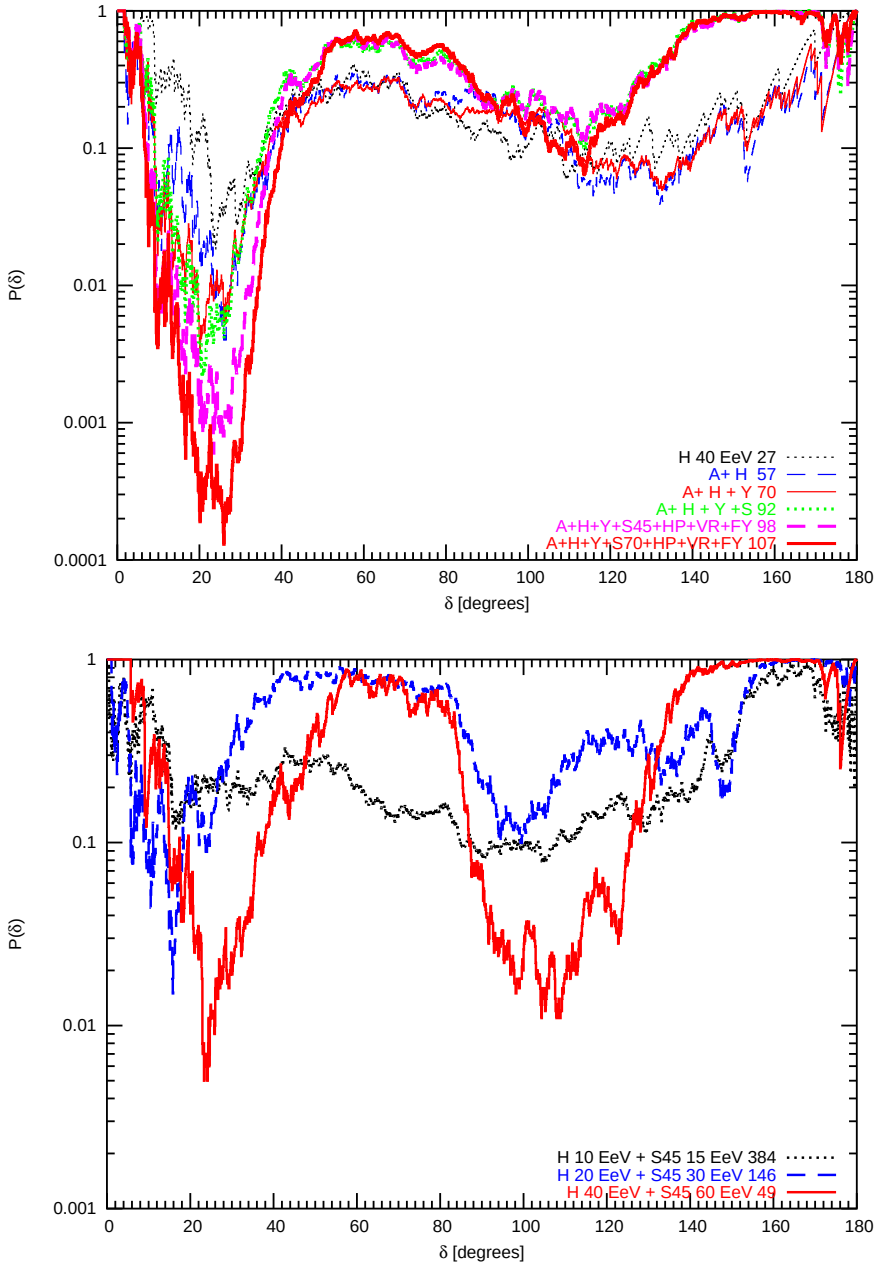

Figure 4.3: (Top) Chance probability $P(\delta)$ to observe a larger value of the autocorrelation function as function of the angular scale δ for different combinations of experimental data [165]; label of experiments as in Fig. 4.1. (Bottom) Chance probability $P(\delta)$ to observe a larger value of the autocorrelation function as function of the angular scale δ for different cuts of the rescaled energy E' [165]: black $E' \geq 1 \times 10^{19}$ eV, blue $E' \geq 2 \times 10^{19}$ eV and red line $E' \geq 4 \times 10^{19}$ eV.

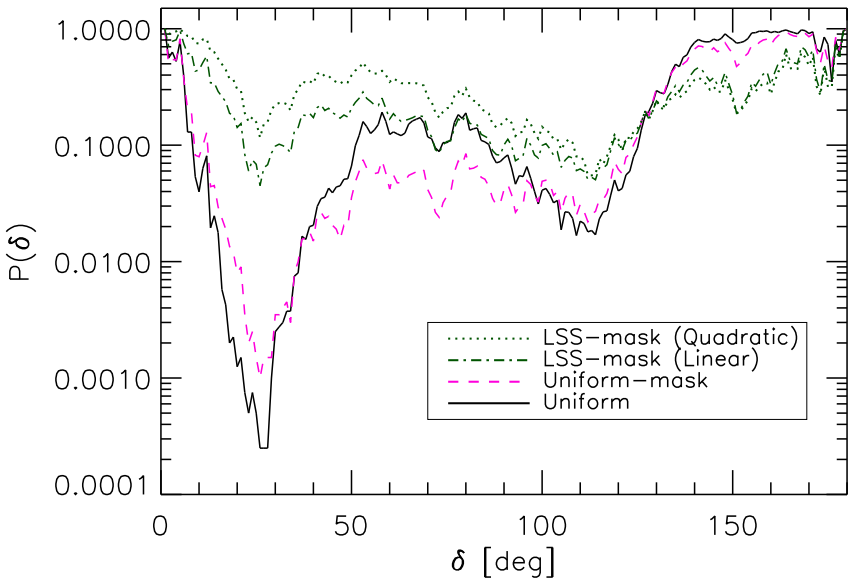

Figure 4.4: The solid line shows the chance probability $P(\delta)$ (in %) to observe a larger value of the autocorrelation function as function of the angular scale δ for the combination of experimental data of Hires+AGASA+Yakutsk+SUGAR as described in the text. The dashed purple line is the same signal, when cosmic rays falling in the PSCz catalogue mask are disregarded. The dot-dashed green line is the same quantity, if the random events are sampled according to the LSS distribution, instead of an uniform one.

It is important reminding that the catalogue suffers of an incomplete sky coverage. This includes a zone centered on the galactic plane and caused by the galactic extinction and a few, narrow stripes which were not observed with enough sensitivity by the IRAS satellite. These regions are excluded from our analysis with the use of the binary mask available with the PSCz catalogue itself. This reduces the available sample (by about 10%) to 93 events and the nominal chance probability to 0.1% (Fig. 4.4, dashed–purple line). Note that this is a quality factor of the catalogue, not an intrinsic problem of the data or theoretical prediction. The green/dot–dashed line in Fig. 4.4 shows the chance probability of the signature found in [165], if the random events are sampled according to the LSS distribution (obviously convolved with the experimental exposures), rather than from an uniform one. Finally, the dotted line shows the same result if the random events are sampled according to *the square* of the LSS distribution, as one would expect e.g. for a strongly biased population of sources.

The prominent minimum of [165] is greatly reduced when using as null hypothesis the LSS model instead of the uniform one; this effect is even

more prominent in the quadratic map. Also, the data are less clustered than expected from an uniform distribution at $\delta \sim 160^\circ$ ($P(w > w_\star) \sim 100\%$). This additional puzzling feature disappears when using the LSS null hypothesis, as it appears clearly in Fig. 4.5, where we plot the function $P(\delta) \times [1 - P(\delta)]$ for the same cases of Fig. 4.4. This function vanishes if any of P or $1 - P$ vanishes and has the theorethical maximum value of $1/4$. So, the higher its value is the more consistent the data are with the underlying hypothesis. Apart for the very small scales, where our results are unrealistic since we did not include magnetic smearing or detector angular resolution, the much better concordance of the UHECR distribution with the LSS distribution than with the uniform one is evident at any scale. Taken at face value, our result implies a nominal probability $P \sim 5\%$ that the main signature found in Ref. [165] arises as a chance fluctuation from the LSS distribution. This result suggests that the clustering properties of LSS are in much better agreement with the experimental data than a pure isotropic distribution. This is not an unexpected feature given that, as found in [166], the typical size on the sky of the clusters of structures lie in the range 15°-30°.

The absolute scale of the result in Fig. 4.4 is affected by an uncertainty due to the true energy scale: we calculated the map assuming that the HiRes energy scale is the correct one, in agreement with Berezinsky et al.'s fit of the dip due to pair production of protons on CMB [171]. But if the true energy is higher, as a compromise solution with the other experiments may require, the chance probability is slightly higher. In this respect, one may look at our result as a conservative one. Hence, the largest sample of [165] which we chose on the basis of the strongest signal is consistent within "2σ" with the clustering properties expected from LSS distribution*. Also given the fact that the "*true probability*" is higher than the nominal one (due to the penalty factor of the search a posteriori performed in [165]), this may be considered as an argument in favor of their interpretation.

In order to understand why their result is consistent with our sampled catalogue, it is useful to look at the chance probability of the autocorrelation signal of events sampled from the LSS according to the experimental exposures. We show it in Fig. 4.6 for two samples of 93 and 279 data, respectively the same statistics of the dashed and dot–dashed curves in Fig. 4.4, and a factor 3 higher. The curves are obtained as follows: a large number $M(\simeq 10^4)$ Montecarlo realization of N events is sampled according to the LSS probability distribution, and for each realization i we calculate the function $w_i^{\rm LSS}(\delta)$. We generate analogously M random datasets from an uni-

*Consistent within "2σ" means here at least in 5% of the cases. The distribution is indeed far from gaussian, and the number of σ can be used in its loose sense only.

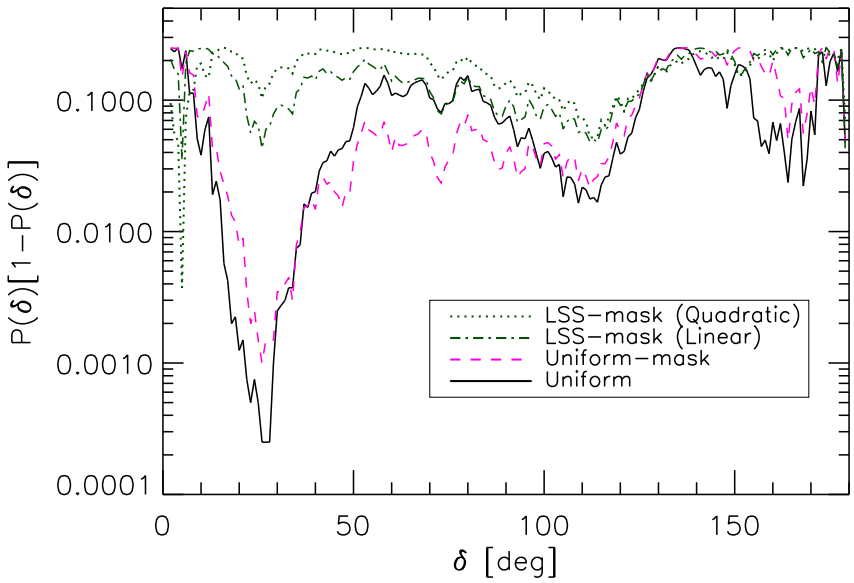

Figure 4.5: The function $P(\delta) \times [1 - P(\delta)]$ for the same cases shown in Fig. 4.4. See text for details

form distribution, and calculate $w_j^{\rm iso}(\delta)$. The fraction of the M^2 simulations where the condition $w_j^{\rm iso}(\delta) \geq w_i^{\rm LSS}(\delta)$ is fulfilled is the probability

$$P_{\rm LSS}(\delta) = \frac{1}{M^2} \sum_{i=1}^{M} \sum_{j=1}^{M} \Theta[w_j^{\rm iso}(\delta) - w_i^{\rm LSS}(\delta)], \tag{4.3}$$

which is the function shown in Fig. 4.6.

An important qualitative feature is that the shape of the curve presents indeed a broad minimum at scales of $\delta \lesssim 30^\circ$, and a moderate plateau at scales of $70^\circ \lesssim \delta \lesssim 130^\circ$. As shown by the $N = 279$ case, in particular the first feature is intrinsic to the data: the more data are sampled, the more enhanced it appears. This is also the trend shown in [165] when enlarging the experimental statistics considered. Also, the higher the energy cut in the map, the stronger the signature, since the local structures are more and more prominent. Finally, the LSS data samples are typically less clustered than the uniform ones at $\delta \gtrsim 150^\circ$ ($P > 50\%$).

On the other hand, the minimum found in Fig. 4.6 for the sample of 93 data is much less prominent than the one shown by the dashed curve in Fig. 4.4. This explains why the consistency is "only" at the level of $\sim 5\%$. This fact is not unexpected, given the predictions of Ref. [166]: ~ 100 events are too few *to guarantee* a detection of the imprint of the

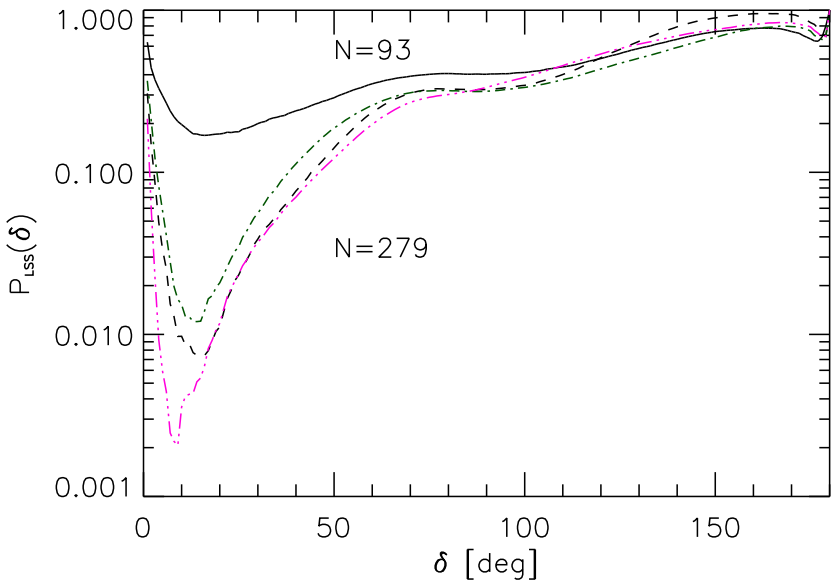

Figure 4.6: Chance probability $P(\delta)$ (in %) to observe a larger value of the autocorrelation function as function of the angular scale δ for two samples of 93 and 279 data according to the LSS map cutted at 4×10^{19} eV. The three lower curves for the $N = 279$ case show the signature when the map cutted at $E > 2, 4, 5 \times 10^{19}$ eV—from top to bottom—is used, while the upper solid curve refers to the case $N = 93$, $E > 4 \times 10^{19}$ eV.

LSS with a high significance. Consistently with the results of Fig. 4.4, we checked that the dip in Fig. 4.6 becomes more pronounced if we use a quadratic bias with LSS. Although not statistically significant at the moment, a confirmation of a highly clustered signal at intermediate scales may suggest thus a more than linear correlation of UHECR sources with the galaxy density field. Alternatively, this may be due to the magnetic smearing of a few relatively strong point-sources.

Clearly, a smoking gun in favor of the LSS-origin would be a correlation between the data and the expected excess in the LSS map. By performing an analysis similar to the previous one, but in terms of the cross-correlation function between simulated data and sampled ones, we did not find any evidence favoring a LSS origin with respect to the uniform case. Actually this is not unexpected within the model considered in [166], since ~ 100 data at energy $\gtrsim 4 \times 10^{19}$ eV is still a too low statistics to draw a firm conclusion in this sense. However, the lack of this signature may also be related to the role of intervening magnetic fields. Acting on an energetically (and possibly chemically) inhomogeneous sample, magnetic fields may displace the observed positions with respect to the original ones in a non trivial way, with-

out evidence for a characteristic scale, at least in a poor statistics regime. A possible hint towards a non-negligible role of magnetic fields is given also by the fact that the dip in the LSS signal is already present at relatively small angles. This feature may have disappeared in the UHECR sample due to a smearing effect of the magnetic fields.

4.4 Discussion and Conclusions

We have analyzed the hypothesis that the broad maximum of the two-point autocorrelation function of the UHECRs arrival directions around 25° found in Ref. [165] may be due to the imprint of the LSS. We have concluded that this suggestion is at least partially supported by the UHECR sky map constructed starting from a LSS catalogue. Even their nominal (non penalty factor-corrected) result for the autocorrelation function is consistent within 2 σ with our expectations. A stronger correlation with source luminosity or a more-than-linear bias with overdensity may improve the agreement. Also, the correlation may not be directly with the LSS themselves: any class of sources which is numerous enough is expected to show some indication in favor of this correlation. The low statistics and the role of the magnetic field deflections may explain why no significant *cross-correlation* between data and LSS overdensities is found.

The authors of Ref. [165] also claim that the if the signal found is real, a heavy composition of the UHECRs is disfavored. However, we note that a heavy or mixed composition of the UHECRs may well be consistent with the signature. If we limit to the role of the (relatively well known) galactic magnetic field, a naive extrapolation of the simulations performed in [84] would indicate in the linear regime deflections for iron nuclei of about 130° with respect to the incoming direction. UHE iron nuclei would then be in a transition from diffusive to ballistic regime. Nonetheless, the signal is sensitive to the *relative* deflections of "bunches" of cosmic rays originating from a similar region of the extragalactic sky, for which typical models of the regular galactic magnetic field predict a smearing $\lesssim 40°$ even for iron nuclei, as long as their energies do not differ by more than about 30%. One may even speculate that the second dip at large angles (arising from cross-correlation of different groups of overdensities) might originate from primaries of different rigidity coming from the same few sources, splitted apart by intervening fields. Also, the consideration in [165] that accounting for the medium scale structure in UHECRs may change the significance of claims of small-scale clustering should be carefully examined. If the picture emerging from Ref. [165] and this chapter is consistent, *both* LSS and magnetic fields play a role in

shaping the signal, otherwise it is hard to explain the lack of cross-correlation with known overdensities of LSS. “Filaments and voids" in the observed data do not match the position of filaments and voids in the LSS. But if they are nonetheless connected, this difference must be rigidity-dependent. Thus, a cluster of events with high rigidity may well arise in a void of the presently known UHECR filamentary structure, which may sit closer to an overdensity of the LSS. Indeed, the clustered component of the AGASA data favoring small-scale clustering *does show* a different energy spectrum than the non-clustered component. This discussion emphasizes that, unfortunately, it is virtually impossible to draw strong conclusions at present, even assuming that the clustering at intermediate scales is physical.

In conclusion, the analysis performed in this chapter does not exclude that the signal found in [165] may be due to the imprint of the LSS, and indeed gives some support in this sense. Definitely, the larger statistics that the Auger Observatory is going to collect in the next years is needed to tell us finally if astronomy is possible with UHECRs or, equivalently, if we will be ever able to look at the sky with new and “ultra-energetic” eyes.

Chapter 5

Overview of Gamma Ray Astronomy

Gamma Ray Astronomy, as cosmic rays physics, is a very wide field comprising many different aspects both theoretical and experimental. In this chapter we review only some of the fundamental issues involved, with the aim of giving a basic understanding of the field in particular illustrating the experimental difficulties and related techniques on one hand and the recent results and future capabilities on the other. For extensive reviews of the field we address the reader to the papers [172; 173; 174]. Also for the most updated reports in the current experimental status we address to the biannual proceedings of the International Cosmic Ray conferences [176].

5.1 Introduction

Gamma-ray astronomy is a rapidly developing subject. The first source detections were made in the 1960s, but it has only been in the last fifteen years that the field has been put on a solid foundation.

Two important developments have happened in this time. First, discoveries made by satellite experiments on the Compton Gamma Ray Observatory have revolutionized our understanding of the high-energy universe. Observations have shown that there are many more astrophysical sources of high-energy radiation than had been previously suspected. Second, ground-based experiments using the atmospheric Cherenkov technique have unambiguously detected gamma rays from a handful of sources at very high energies (10^{12} eV and beyond). These detections confirm the belief that gamma-ray astronomy can be done from the ground and indicate a great potential for future scientific discovery.

Although gamma-ray astronomy is still in an exploratory phase, the goals for the field are lofty. We would like to learn as much as we can about the highest energy astrophysical accelerators. This knowledge may help us understand the origin of the cosmic rays. In addition, by studying sources of very

high-energy radiation, we glimpse astrophysical situations in which conventional physics operates under extreme conditions (e.g. intense gravitational or magnetic fields), or in which new physics may be required. High-energy gamma rays represent one of the last remaining regions of the electromagnetic window to be systematically explored. As with any new energy band, we expect to encounter new phenomena not seen at other wavelengths.

5.2 Experimental techniques

Gamma rays encompass a very wide range of energies (MeV to 10^{20} eV). Therefore, we cannot expect that a single type of detector will work at all gamma-ray energies. The three principal detectors are satellite experiments, atmospheric Cherenkov telescopes, and air shower arrays. As shown in Fig. 5.1, current satellite experiments operate at MeV and GeV energies, atmospheric Cherenkov telescopes operate between 250 GeV and 50 TeV, and air shower arrays operate above 1-10 TeV. In this section, we discuss the various techniques and the actual experiments using it.

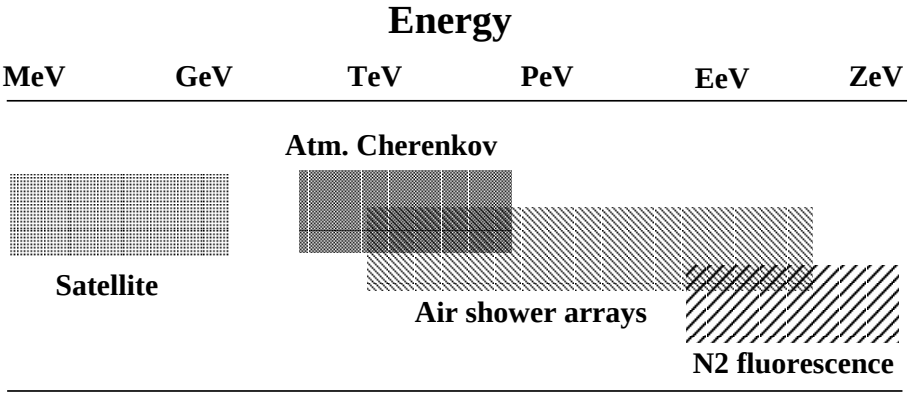

Figure 5.1: Gamma-ray detection methods [176]. The ranges in energy covered by current gamma-ray detectors are shown. The horizontal axis is $\log(E)$ where E is the energy in eV.

5.2.1 Satellite telescopes

The spectrum of high-energy photons is divided into the X-ray and γ-ray bands, which typically overlap at photon energies of 100-200 keV. The major X-ray satellite instruments operating at the present time are RXTE, ASCA, Chandra, and XMM-Newton. In the γ-ray band between 100 keV and 100

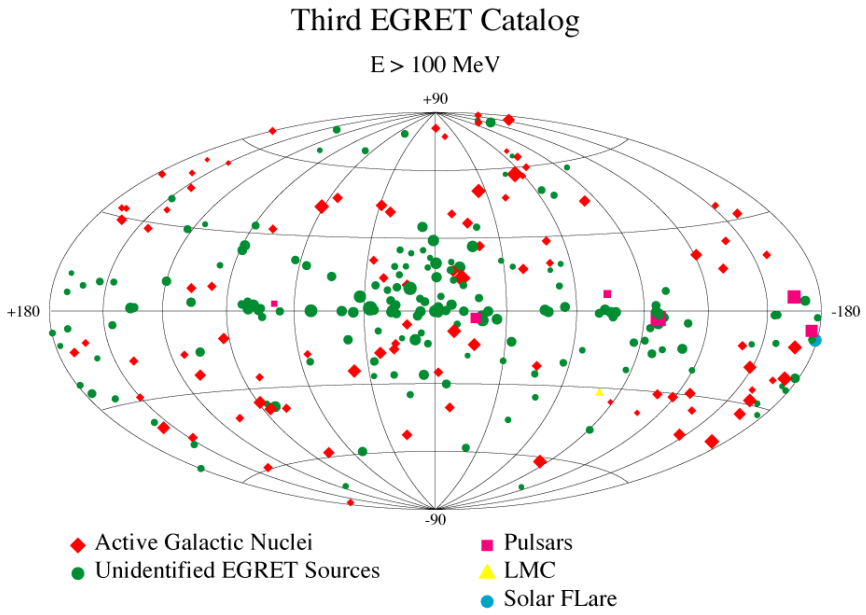

Figure 5.2: The Third EGRET Catalog consists of 271 sources: 5 pulsars, 1 solar flare, 66 high-confidence blazar identifications, 27 possible blazar identifications, 1 likely radio galaxy (Cen A), 1 normal galaxy (LMC), and 170 unidentified sources.

MeV, the operating satellite telescopes are HETE-2, Swift, and INTEGRAL. There is currently no operating space-based telescope with significant sensitivity to high-energy γ-rays above 100 MeV. The last major telescope in this band was EGRET on the Compton Gamma Ray Observatory (CGRO) which operated between 1991 and 2000.

EGRET and the Cosmic Gamma Background

The Compton Gamma Ray Observatory (CGRO) started the observations in 1991. Aboard the satellite there were four gamma-ray experiments: BATSE, OSSE, COMPTEL, and EGRET [177]. EGRET (Energetic Gamma Ray Experiment Telescope) detects high-energy gamma rays via their conversion to electron-positron pairs. EGRET was made up of a spark chamber system to track the electron-positron pairs and a total absorption calorimeter (TASC) to measure the track energies.

In the 9 years of operation the physics outcomes have been lofty. In Fig. 5.2 is shown the final catalogue of VHE gamma sources detected by EGRET. Various galactic sources among which pulsars, but for the most unidentified, have been established as gamma emitters; more interestingly a lot of extragalactic sources have been discovered, mainly AGN of Blazar-

type class. Most of these sources are looked for their TeV counterpart by the ground-based telescopes.

Perhaps among the most interesting results there is the detection of a diffuse isotropic radiation that could result from many unresolved extra-galactic point sources or from the injection of very high energy radiation from processes in the early universe. EGRET has measured the isotropic diffuse radiation at energies from 30 MeV to 100 GeV [178]. New measurements of this radiation in the GeV (and possibly TeV) energy bands will likely have to wait until the launch of GLAST. The high-energy counterpart of this emission will be the main topic of the next chapter.

GLAST

The motivations for a next generation satellite telescope for gamma-ray astronomy are clear. Only a space telescope can monitor the gamma-ray sky at energies below 10 GeV. With advances in technology, it is probable that a new telescope could extend all-sky coverage to at least 100 GeV. The scientific objectives of high energy gamma-ray astronomy clearly require a combination of both space and ground-based detectors. A number of detector concepts for a new satellite gamma-ray telescope have been put forward. GLAST is a future, major high-energy γ-ray mission that is being developed by an international consortium and currently scheduled for launch in Fall 2007. The mission consists of two instruments, the Large Area Telescope (LAT) and the GLAST Burst Monitor (GBM) [180]. The LAT will have greatly superior performance relative to EGRET (i.e. an order of magnitude improvement in sensitivity). Of particular importance for VHE astronomy, the LAT will have a relatively constant effective area up to energies of 300 GeV, implying that many

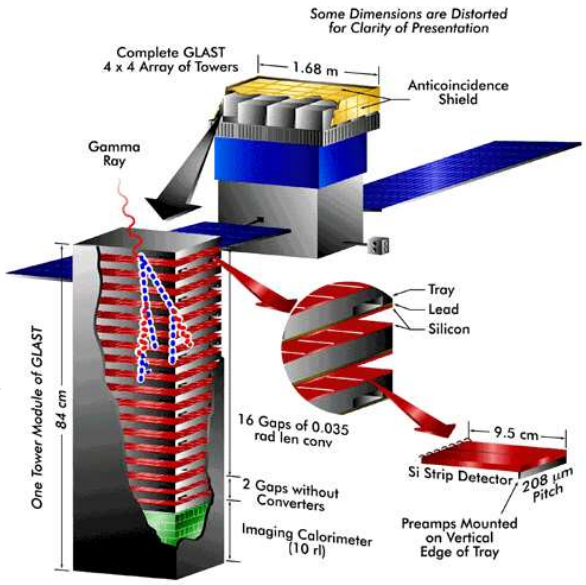

Figure 5.3: Artist's conception of GLAST, the next major satellite γ-ray telescope [179]. The main GLAST instrument will consist of interleaved Si-strip/absorber layers for tracking and an imaging CsI calorimeter for energy and position measurement.

sources detected by GLAST will have measured spectra that overlap with ground-based instruments. The GBM is a gamma-ray burst detector that will detect and localize bursts in a similar manner to BATSE on the CGRO. The GBM performance will be similar to BATSE but will cover a wider energy range with a smaller collection area. The major science goals of GLAST are to discover new sources of high-energy γ-rays (e.g. AGN, pulsars, SNRs, GRBs, and new objects), to more accurately measure spectra and positions of sources to understand the mechanisms of high-energy particle acceleration, and to probe dark matter and the early universe via observations of possible neutralino signatures and of distant AGN and GRBs.

In addition to GLAST, the AGILE mission aims to study gamma-ray and X-ray sources in the 30 MeV - 30 GeV and 10-40 keV energy ranges, respectively. AGILE is being developed by a group of Italian institutions for a launch in the 2006-2007 time frame. Details on the mission can be found at their website [181].

5.2.2 Extensive gamma air showers detectors

At very high energies where satellite experiments are limited by rapidly falling gamma-ray fluxes, astronomy can only be done by ground-based instruments using the Earth's atmosphere as the detection medium. For most wavelengths, the atmosphere poses significant challenges for astronomy. The quality of optical and infrared astronomy is compromised by observations made through the atmosphere. For ultraviolet, X-ray, and gamma rays, direct detection by ground-based instruments is impossible. At very high energies (VHE), however, indirect gamma-ray detection is possible. VHE gamma rays initiate cascades, or extensive air showers (EAS), of particles which propagate down through the atmosphere. The secondary charged particles and photons produced in the EAS can be detected by ground-level instruments. Ground-based gamma-ray telescopes turn the possible disadvantage of atmospheric absorption into an advantage.

We have already widely reviewed the properties of EAS in the chapter devoted to cosmic rays. Here we only underline some other particular features that is relevant for gamma showers. The structure of gamma EAS is reasonably well understood. A very high-energy gamma ray interacts with an air molecule in the upper atmosphere at altitudes between 10 and 15 km. The electron-positron pair produced from this interaction initiates an electromagnetic cascade. Photons are generated via bremsstrahlung and subsequent pairs are created from the photons. The number of particles in the cascade increases geometrically until the mean electron (e^+ and e^-) energy falls below the critical energy (85 MeV) where energy loss by ionization exceeds

that of bremsstrahlung. At this point, the shower has reached its maximum development and as it subsequently propagates lower in the atmosphere the number of charged particles decreases exponentially. The size of an EAS refers to the number of charged secondary particles (mostly electrons) in the cascade. For vertical showers initiated by 100 TeV gamma rays, the size at shower maximum is typically 100 000, and 25 000 particles reach mountain level heights.

The radiation length of air is 37 g cm^{-2} at STP. At sea level, the atmospheric depth is 1033 g cm^{-2} which corresponds to nearly 28 radiation lengths. Even at very high mountain sites (e.g. Tibet), there is >600 g cm^{-2} of atmospheric overburden. Shower maximum thus generally occurs well above ground level for showers initiated by all but the most energetic primaries. For example, shower maximum for vertical 1 TeV gamma-ray showers occurs at an average altitude of 8 km. Altitude is then a fundamental element for the site experiment in order to optimize the detection performances.

Gamma-ray astronomy is possible using EAS for a number of important reasons. The high energy of the incident photon leads to shower particles at relativistic energies. As a result, the particles are beamed to the ground and their trajectories retain the directionality of the incident gamma ray. The shower wavefront is narrow and can be thought of as a "pancake" of particles with a thickness of 1 m at the center. The tight longitudinal structure means that fast timing (1 ns) can be used to measure the orientation of the shower wavefront and hence estimate the primary direction. In addition, the fast time scale allows the signal produced by the shower front particles to be separated from random background processes. Finally, and most importantly, the lateral distribution of air showers allows detectors spread out on the ground to be sensitive to particles whose initial trajectory would not have intersected a detector in the absence of the atmosphere. The effective area of an air shower detector is much larger than its physical area. Detector arrays can be constructed which sample only a fraction of the particles in the lateral distribution.

Air shower arrays are detectors which sample the charged particles of an air shower. Fast timing between detector elements is used to estimate the primary particle direction. The shower core is approximated by the location of greatest particle density and the lateral distribution is reconstructed from measurements of the particle density at different radii from the core. The primary energy is inferred from the calculated shower size.

The relativistic charged particles in EAS are moving faster than the speed of light in air and emit Cherenkov radiation [182]. At sea level, the index of refraction of air is 1.000283 which leads to a Cherenkov threshold energy of

22 MeV for electrons and 4.4 GeV for muons. Most of the charged particles in EAS have energies exceeding these threshold values and thus a copious amount of Cherenkov radiation is generated. The Cherenkov production spectrum varies as λ^{-2}, where λ is the photon wavelength. Since the atmosphere is largely transparent to light between 300 and 600 nm, most of the produced Cherenkov radiation reaches the ground under good atmospheric conditions. For example, a 1 TeV gamma-ray shower produces an average of 3×10^6 Cherenkov photons at ground level.

The Cherenkov radiation is calorimetric in the sense that most of it is produced from particles near shower maximum. Similarly, since the lateral distribution of Cherenkov light is determined largely by the altitude of shower maximum and the Cherenkov opening angle, the light pool on the ground is relatively uniform in density out to a distance of 125 m from the core, beyond which the density falls off rapidly. The generic *atmospheric Cherenkov telescope* uses a mirror to concentrate EAS Cherenkov light onto a single photomultiplier tube or onto a camera of tubes.

5.2.3 Cosmic ray rejection

Extensive air showers initiated by hadronic cosmic rays are similar in many respects to those initiated by gamma rays. Therefore, because of their high flux, cosmic rays constitute a formidable background for ground-based telescopes seeking to detect gamma rays. The initial interactions of a cosmic ray in the atmosphere produce primarily hadronic particles (nuclei, pions, etc.). Charged pions feed the hadronic cascade but neutral pions decay to photons which initiate electromagnetic sub-showers. Cosmic ray showers evolve into predominantly electromagnetic cascades with cores of hadronic particles. Most of the hadrons are absorbed in the atmosphere. Approximately, 10% of the shower energy is carried in the form of GeV muons produced by charged meson decay. The muons that do not decay in flight reach the ground.

The integral flux of cosmic ray particles above 1 TeV is $1.7\times10^{-5}\mathrm{cm}^{-2}\mathrm{s}^{-1}\mathrm{sr}^{-1}$. In a circular angular bin of radius 0.5°, the cosmic ray rate is 4.1×10^{-9} particles $\mathrm{cm}^{-2}\mathrm{s}^{-1}$ which is 400 times higher than the integral gamma-ray flux from the Crab Nebula above 1 TeV. Without some means to discriminate against the overwhelming background of cosmic rays, very high-energy gamma-ray astronomy would be extremely difficult. Fortunately, there are significant differences in the properties of showers initiated by gamma-ray and cosmic ray primaries that can be exploited to achieve background rejection which are manifested in differences in the observed Cherenkov light pattern on the ground for the cherenkov experiment or in the number of particles and their later profile for EAS arrays.

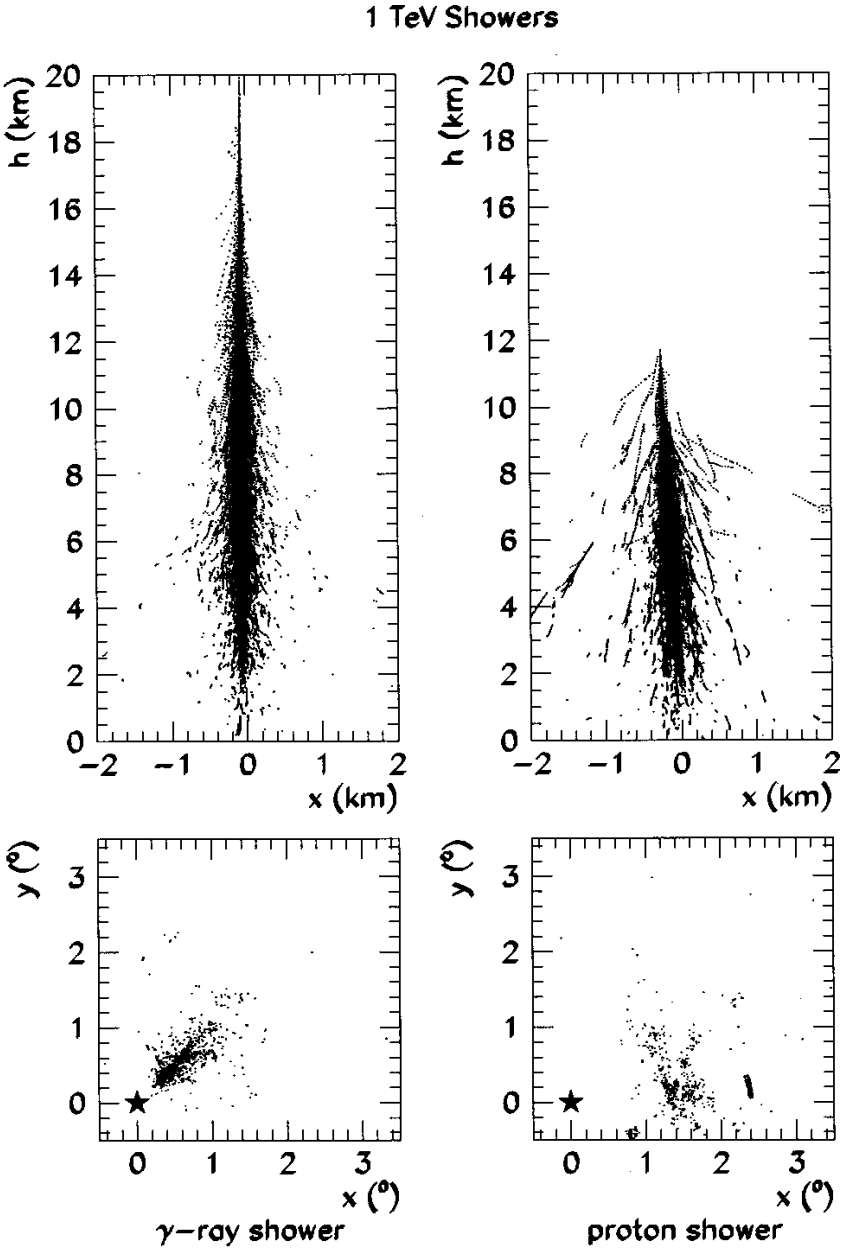

Figure 5.4: Development of vertical 1-TeV proton and γ-ray showers in the atmosphere [174]. The upper panels show the positions in the atmosphere of all shower electrons above the Cherenkov threshold; the lower panels show the resulting Cherenkov images in the focal plane of a 10-m reflecting mirror when the showers fall 100 m from the detector. (Note that the center of the focal plane is situated at the bottom left of the bottom panels.)

Figure 5.4 illustrates the main differences that are exploited in gamma and hadronic showers separation. Due to higher content of muons, an hadronic showers generally produces a more irregular pattern of cherenkov photon in the mirror while a gamma shower is typically more compact and regular in shape. The same is true for EAS array where a proton shower results in various isolated detected spots of muons near a central core of particles while a only a compact core is seen in a gamma EAS. The separation, however, can be achieved only on a statistical basis, given that the pattern distributions of gamma and proton EAS always overlap in some amount. Comprehensive reviews of the techniques for rejecting cosmic rays with atmospheric Cherenkov telescopes can be found in [183; 184].

The amount of Cherenkov radiation produced is also an useful mean to gamma-proton separation in cherenkov telescopes. The Cherenkov photon yield in EAS initiated by cosmic ray primaries is significantly smaller than it is in EAS initiated by gamma rays. In cosmic ray showers, a large fraction of the energy is carried by hadrons and neutrinos which produce little or no amounts of Cherenkov radiation. For primary energies between 0.2 and 10 TeV, the ratio of the Cherenkov light intensity found in a gamma-ray shower to that found in a proton shower is between two and three. Experiments operating at these energies achieve a certain degree of hadronic suppression.

Finally, for point sources, also used is the fact that cosmic rays arrive isotropically whereas gamma rays arrive from the source direction. The angular resolution $\delta\vartheta$ becomes then a powerful mean to reduce the background. If the angular resolution increases the gamma flux from the source remains constant while the hadron background decreases as $\delta\vartheta^2$.

5.2.4 Atmospheric Cherenkov technique

Atmospheric Cherenkov Telescopes detect VHE γ-rays by capturing the rapid ($\sim$ 5 ns) Cherenkov flashes amidst the background of night sky photons. These telescopes use large optical mirrors to focus the mostly blue Cherenkov radiation onto fast photomultiplier tubes (PMTs). The primary advantages of the atmospheric Cherenkov technique are high sensitivity, excellent angular resolution and energy resolution, and relatively low energy threshold. The disadvantages are moderate duty-cycle ($\sim$ 10%) and small field-of-view (FOV) ($\sim$ 5°). The Cherenkov telescopes operating today include CACTUS, CANGAROO-III, HESS, MAGIC, PACT, SHALON, STACEE, TACTIC, VERITAS. and Whipple. CACTUS, PACT, and STACEE are examples of wavefront-sampling telescopes that use an array of mirrors to gather the Cherenkov radiation, measuring the arrival time and amplitude of the Cherenkov pulse at many distributed locations on the ground. The other

Experiment	Type	Location	Altitude	Specifications	Ref.
CACTUS	AC-Sampling	USA	640 m	144 x 42 m^2	
CANGAROO-III	AC-Imaging	Australia	165 m	4 x 78 m^2	[185]
HESS	AC-Imaging	Namibia	1800 m	4 x 110 m^2	[186]
MAGIC	AC-Imaging	Spain	2250 m	1 x 226 m^2	[187]
PACT	AC-Sampling	India	1075 m	25 x 4.5 m^2	[188]
SHALON	AC-Imaging	Kazakhstan	3338 m	1 x 11 m^2	[189]
STACEE	AC-Sampling	USA	1700 m	64 x 37 m^2	[190]
TACTIC	AC-Imaging	India	1400 m	1 x 9.5 m^2	[191]
VERITAS	AC-Imaging	USA	1275 m	2 x 110 m^2	[192]
Whipple	AC-Imaging	USA	2250 m	1 x 78 m^2	[193]
ARGO-YBJ	Air Shower	Tibet	4300 m	4000 m^2	[194]
GRAPES-III	Air Shower	India	2200 m	288 x 1 m^2	[195]
Milagro	Air Shower	USA	2630 m	4800 m^2	[196]
Tibet	Air Shower	Tibet	4300 m	761 x 0.5 m^2	[197]

Table 5.1: Currently operating VHE gamma-ray telescopes. The name of each telescope is given, along with its type (AC=Atmospheric Cherenkov), location, altitude, specifications, and reference at ICRC05. The specifications list the currently installed detector area (mirror area for atmospheric Cherenkov and instrumented detector area for air shower). Adapted from [176]

telescopes are examples of the more established imaging Cherenkov technique where the Cherenkov radiation is focused onto an imaging camera at one or more locations on the ground. See Table 5.1 for a summary of the atmospheric Cherenkov telescopes.

Atmospheric Cherenkov telescopes are typically composed of one or more individual mirrors. The mirrors commonly have a parabolic or spherical shape, vary in size from 2 to 10 m in diameter, and are composed of multiple facets for ease of construction. The requirements on the mirror specifications are not nearly as severe as large optical telescopes because the angular structure of the Cherenkov light is relatively coarse (3 arcmin). Larger mirrors generally result in lower energy thresholds. With mirror size limited primarily by cost, energy thresholds have likewise been limited.

The success of the imaging Cherenkov technique has naturally led to a vigorous discussion regarding future experiments using this technique. A lower-energy threshold can be achieved either by building single large reflectors or arrays of multiple reflectors. The concept of a very large reflector with a high-resolution imaging camera is the basis of the MAGIC project whose original baseline incorporates a 17 m diameter mirror. MAGIC is now in the

process of an upgrade to the original instrument. The major component of MAGIC Phase II will be a second 17 m diameter reflector. Other various improvements should lower the energy threshold of MAGIC and improve its sensitivity, especially at energies below 100 GeV.

The alternative is to build and deploy multiple telescope units each consisting of a large mirror (e.g. 10m diameter) and imaging camera system. To avoid the problem of the large costs required an useful approach is to make use of large mirror facilities that already exist; in particular large solar mirrors (heliostats) could be used as the primary collector in an atmospheric Cherenkov telescope [198]. The basic idea is to use secondary mirrors on a central tower to image the Cherenkov light reflected from the heliostat field onto photomultiplier tube elements. In the last few years, this technique was employed by various groups. The CELESTE experiment, located at the site of the Themis solar plant in the eastern Pyrenees, France [199], uses 40 heliostats comprising a total mirror area of 2100 m^2. Actually, CELESTE is just concluded its operation obtaining interesting results on few sources at low energy threshold [200]. STACEE is located at the Sandia National Laboratories in Albuquerque, New Mexico and uses 48 heliostats, comprising a mirror collection area of 1900 m^2 [201]. The experiments PACT and CACTUS also enters in the category of Atmospheric Cherenkov sampling telescopes. However, Solar towers arrays present a series of technical problems like, mainly, that of forming a reliable experimental trigger that takes into account the differen times of arrival of the photon from each different heliostat. More promising is the technique of array of cherenkov telescopes. The power of stereoscopic measurements of Cherenkov showers to improve gamma/hadron separation and energy resolution has been demonstrated by the HEGRA CT system at energies near 1 TeV [202].

The technical motivations for imaging telescope arrays are clear. The increased area of multiple reflectors lowers the energy threshold and expands the dynamic range. A trigger system using information from more than one mirror effectively eliminates the low-energy background of local penetrating muons. Simultaneous measurement of the shower parameters by a number of reflectors constrains the geometry of the shower. This leads to better angular resolution and rejection of cosmic ray background, and to significantly improved flux sensitivity. Multiple measurements of the Cherenkov wave front permit better determination of the shower core and the total shower energy. Good energy resolution is crucial for detailed spectral measurements. A number of groups are actively developing telescopes with multiple imaging elements. The VERITAS array will consist of four 12 m diameter imaging atmospheric Cherenkov telescopes, to be deployed at a mountain site in southern Arizona, USA [192]. Two telescopes have been constructed and

deployed at the Base Camp of the Whipple Observatory on Mt. Hopkins, Arizona [203]. VERITAS is currently scheduled for full operation in late 2006. When operational, VERITAS will be an important complement to MAGIC in the northern hemisphere and to HESS and CANGAROO in the southern. The HESS project, initially working in mono mode is actually working in stereo mode with four 12 m telescopes installed. Planning is underway to construct HESS Phase II [204]; the major component of the upgrade will be a very large 28 m diamter telescope that will be deployed at the center of the HESS-I array in Namibia.

5.2.5 Air shower array technique

Some fraction of the charged particles and photons in VHE air showers reach the ground level and can be detected by *Air Shower Telescopes*. These telescopes typically consist of charged particle detectors (scintillators or resistive plate counters) spread out on a grid and often covered by a lead layer to convert the photons in the shower, or water Cherenkov detectors in which a large tank of water is viewed by a number of fast PMTs. The primary advantages of the air shower technique are high duty-cycle and very wide FOV. Disadvantages are moderate sensitivity, energy resolution and angular resolution, and relatively high energy threshold. Thus, the two major ground-based techniques for detecting VHE γ-rays are fully complementary – both techniques have proven essential in exploring the VHE sky.

After the early pioneering works in 70's and 80's the air shower array technique reached a new phase with the development of a number of new experiments such as Cygnus, CASA-MIA, Tibet, EAS-TOP, and HEGRA in 90's. These detectors had typical energy thresholds near or below 100 TeV. Lower thresholds were achieved by a combination of better instrumentation and higher altitude operation with the most recent experiments. The air shower telescopes operating today include ARGO-YBJ, GRAPES-III, Milagro, and Tibet (see Table 5.1).

Milagro-Argo

The motivation for a detector using the air shower technique at the lowest energies possible is clear. Near 1 TeV, atmospheric Cherenkov telescopes operate with duty cycles of 10% and with relatively narrow fields of view. Air shower arrays are wide aperture and high duty cycle instruments, but conventional air shower arrays with energy thresholds above 10TeV sample only a small fraction (1%) of the charged particles in EAS. There is a need to extend the air shower technique down to 1 TeV. The MILAGRO experiment,

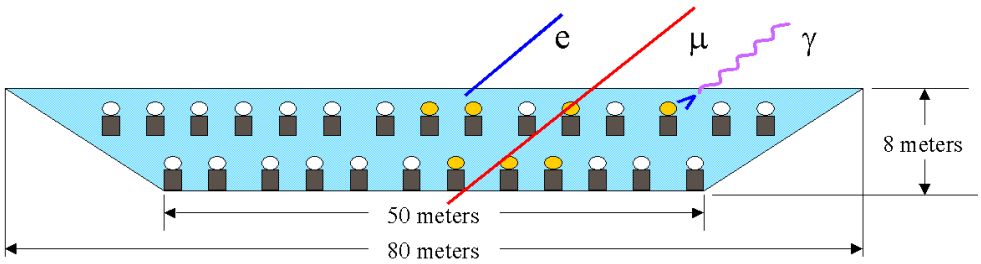

Figure 5.5: Schematic diagram of the Milagro detector

near Los Alamos NM, USA, samples nearly 100% of the air shower particles (electrons and photons) over its active area [205]. MILAGRO consists of 790 photomultiplier tubes submerged in a covered pond of water. The PMTs detect the Cherenkov light created by the interaction of shower particles with the water. The tubes are arranged in three layers. The first layer views the upper 2 m of water to provide a measurement of the time of arrival of the air shower wave front. The second layer is located at depth of 6.5 and provides measurement of the total shower energy and hadronic content. A third layer of optically isolated tubes is located at the bottom of the pond to provide an estimate of the muon content of the shower. The MILAGRO detector is fully efficient near TeV with an effective collection area of 5000 m(i.e. the geometric area of the top surface of the pond). MILAGRO will retain some sensitivity at lower energies, but with lower effective area. The angular resolution near TeV is about 0.5°. The sides of the MILAGRO pool are slanted and the bottom layer for muon detection will have an active area of 1500 m^2. Proton air showers at TeV will produce muon in the detector for 50% of the events. This enables modest degree of cosmic ray background rejection. More efficient rejection may come from estimating the hadronic component of air showers using the middle layer of PMTs. At higher energies (10 TeV and above) the angular resolution and background rejection improve substantially. MILAGRO has limited background rejection capabilities near threshold, and for pointed observations of known gamma-ray sources its sensitivity is poorer than atmospheric Cherenkov telescopes using the imaging technique. For the discovery of new, relatively bright sources and for general survey of the overhead sky, MILAGRO has, instead, unique capabilities. Gamma-ray bursts (GRB) are one of the most promising candidate sources. For hard GRB spectra, MILAGRO should have fluence sensitivity comparable to BATSE and lower than EGRET. If GRB are distributed in non-cosmological manner and their spectra continue to very high energies, they should be detectable by MILAGRO.

As shown in Table 5.1, the ARGO-YBJ experiment is an air shower ar-

ray deployed at the high altitude site of Yangbajing, Tibet. The experiment will eventually consist of a large carpet of resistive plate chambers (RPCs) covering a total area of $6400\,m^2$ [206]. The experiment is still under construction, but a large portion ($> 50\,\%$) is already installed and operational. ARGO-YBJ has already presented early physics results on a variety of topics, including a sky-survey and a GRB search [207].

A future air shower array using the water Cherenkov technique was also proposed [208]. The HAWC experiment would consist of a 300 m x 300 m pond of water that would be instrumented by a large number of PMTs. A key attribute of HAWC would be its high altitude location (> 4000 m elevation) to permit a substantial lowering of the energy threshold relative to Milagro. Detector and sensitivity studies are underway to characterize HAWC. The design of an earlier version of the experiment, called mini-HAWC, that could utilize the existing 900 PMTs from Milagro, is also being actively pursued.

5.3 Gamma Astronomy observations and Astrophysical insights

In this section some of the recent observations are discussed with the aim to illustrate the capabilities of modern gamma detectors and their astrophysical implication for the understanding of very high-energy acceleration mechanisms. In particular we focuss the attention on the ground based observation, from which the latest results come. A brief description of the EGRET satellite results has been discussed in sec. 5.2.1. In sec. 5.3.1 we discuss some basic results regarding the Crab nebula, while in sec. 5.3.2 and 5.3.3 are presented some results regarding galactic and extragalactic sources respectively. Gamma astronomy is now in a situation of flourishing activity and, as a consequence, the observational status rapidly changes and receives updates. The most recent report refers to ICRC05 [176] to which we address the reader, though, in the meanwhile, new results have already come (for example [209],[210]).

5.3.1 The Crab

The Crab Nebula has played a critical role in the development of very high-energy gamma astronomy. It was the first gamma-ray point source to be unambiguously detected by ground-based telescopes. It has now been detected with high significance by almost all the instruments on four different continents. The VHE flux from the Crab does not appear to vary with time.

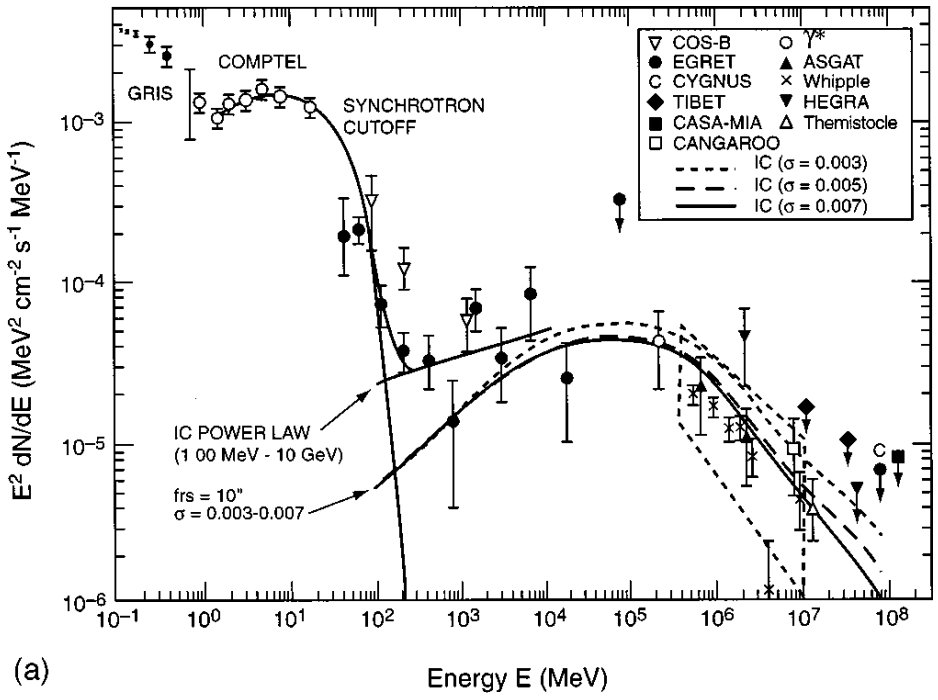

Figure 5.6: The observed energy spectrum from the Crab [174]: A comparison of space and ground-based results and the synchrotron self-Compton model of de Jager and Harding [211]

Thus, for northern hemisphere detectors, the Crab is the long sought-after "standard candle" of astronomy at these energies. As a standard candle, the Crab has allowed the various atmospheric Cerenkov techniques to be compared and data-analysis methods for the rejection of the cosmic-ray background and the localization of a source's position to be refined. The Crab is an unique object in that it is one of the brightest sources in the sky at most wavelengths. A supernova explosion in the year 1054 left behind a very bright radio pulsar and an expanding shell of debris that has traveled approximately three light years from the center in the 944 years since the explosion. The intense, broad-band (radio to X-ray) synchrotron emission seen from the Crab is assumed to result from the acceleration of charged particles to relativistic energies by the pulsar. The slowly expanding supernova shell confines the wind of charged particles resulting in a filled nebula, or *plerion*. The Crab is the brightest plerion in the galaxy. Numerous experiments searched for VHE emission with mixed, and often contradictory, results until a clear steady signal was detected in 1989 by the Whipple Observatory [212]. This detection relied on the use of the imaging Cherenkov technique in which a substantial

fraction (∼97%) of the hadronic back-ground events were rejected based on the properties of gamma-ray and cosmic ray air showers. In addition, there was no evidence for modulation of the signal by the 33 ms pulsar period, indicating that the emission emanates from the nebula rather than the pulsar itself. With this detection, the Crab Nebula became the first true VHE gamma-ray source.

The VHE flux is much higher than expected from an extrapolation of the spectrum given by space-based detectors at lower energies. This can be reconciled using the synchrotron self-Compton (SSC) model [211], in which the VHE emission is produced by the inverse Compton interaction of high energy electrons primarily with their own synchrotron emission. This produces a TeV inverse Comptom bump in the spectrum that is a boosted image of the synchrotron bump (∼10 MeV) seen by the space-based detectors [see Fig. 5.6]. The fit of the data to the model yields the maximum electron energy in the pulsar magnetosphere ($\sim 23\times10^{15}$eV), and the nebular magnetic field (1.63×10^{24}G [213]).

5.3.2 Galactic Sources

Probably, among the latest results, the most striking is the reported HESS survey of the central region of the Galactic plane [215]. The survey was carried out in 2004 with the completed four-telescope array, and it covered a region in Galactic longitude from l = -30° to l = 30°. The coverage in Galactic latitude was approximately b = ±3°. HESS used ∼ 230 hrs to carry out the survey. The average flux sensitivity of the survey was 3% of the Crab Nebula at energies above 200 GeV. Eleven sources were detected with a post-trials statistical significance greater than six standard deviations ($> 6\sigma$). Of these sources, only two (Galactic Center and RX J1713) had been reported previously at very high energies. In addition, HESS reported seven new sources with a post-trials statistical significance greater than four standard deviations [214]. Figure 5.7 shows the significance map for the HESS survey.

This survey is actively under study. For example we can gain insight on the possible acceleration mechanisms in the astrophysical sources. We expect VHE γ-rays to be produced as a result of extreme non-thermal particle acceleration. In principle, the observed γ-ray emission can come from non-thermal bremsstrahlung or inverse-Compton scattering processes involving relativistic electrons or from the decays of neutral pions produced from the interactions of protons and nuclei with ambient material. Potential sources in our Galaxy include pulsars and pulsar wind nebulae (PWN), supernova remnants (SNRs), microquasars, and regions associated with massive star formation. A possibility is to correlate the VHE sources detected in the

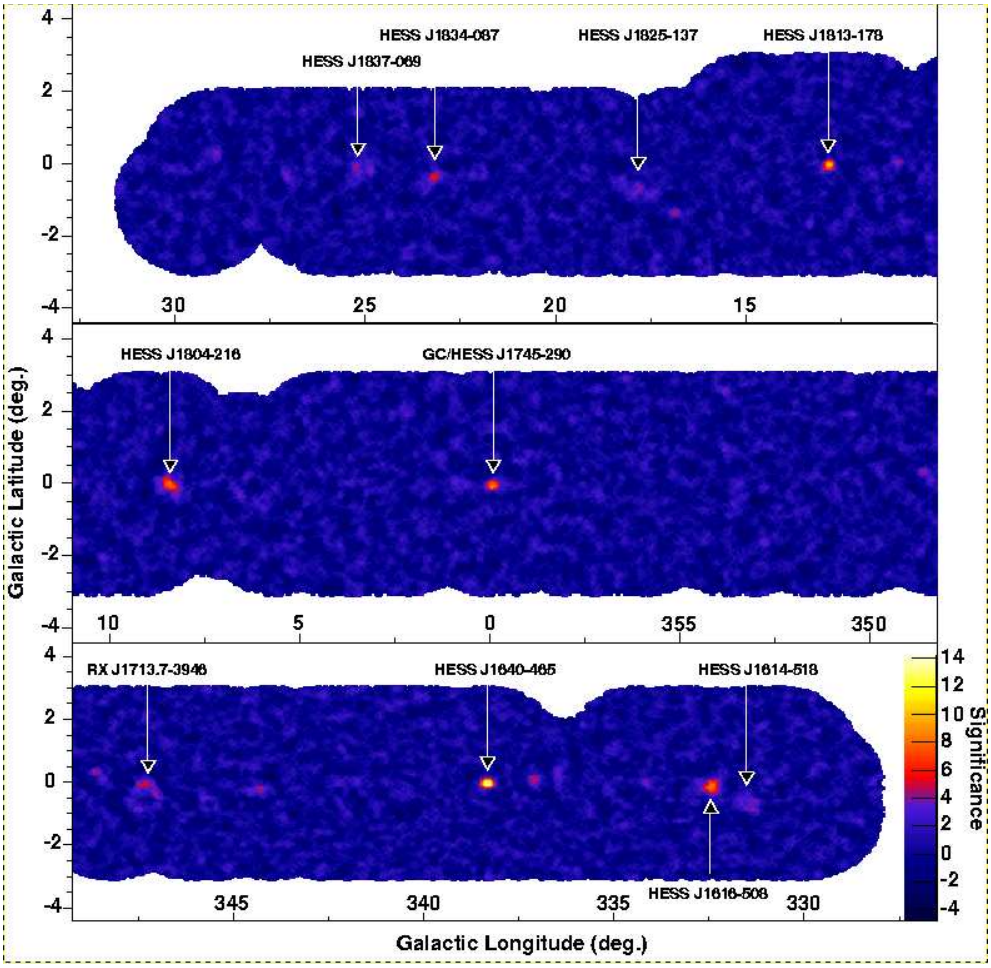

Figure 5.7: Significance map of the HESS Galactic plane survey carried out in 2004 [215]. The survey covered 60° in Galactic longitude (horizontal axis) and approximately ±3° in Galactic latitude (vertical axis). Eleven sources were detected in the survey with a statistical significance greater than six standard deviations, as labeled in the figure. More complete results on additional data, including more discovered sources, have been recently reported [214].

Galactic plane with known objects in order to establish the various source classes, though HESS group has identified in this way only few sources [214]. Another possibility is the correlation both in energy spectra and spazial distribution with maps of atomic and molecular constituents, like CO and HI maps that could indicate possible association with molecular clouds along the line of sight. This kind of studies confirms that, although there certainly may be additional point sources that are not yet resolved in the survey, a significant diffuse of γ contribution is present deriving from interactions of

cosmic rays with molecular material.

The detection of diffuse emission from the galactic plane has been reported also by Milagro. As an instrument with a wide-FOV, Milagro is well-suited to making a survey for γ-ray emission over the entire overhead sky and the search for extended sources is an extension of the general survey. The observations refer to a three year period of two regions in the Galactic plane: 1) Galactic longitude l = 40° to l = 100° and 2) Galactic longitude l= 140° to l = 200° [216; 217]. Both region encompass Galactic latitudes |b| < 5°. In the first region (inner Galaxy), a detection of a signal with a statistical significance of 4.5 standard deviations is reported, corresponding to an integral flux of $\Phi(E > 3.5\,\mathrm{TeV}) = 6.4 \pm 1.4 \pm 2.1 \times 10^{-11}$ photons $\mathrm{cm}^{-2}\,\mathrm{s}^{-1}\,\mathrm{sr}^{-1}$. This result is consistent with an extrapolation from the 1-30 GeV flux measured by EGRET to 3.5 TeV using a differential spectral index of approximately $\alpha \sim 2.6$. The observed flux could be due to both unresolved point sources and true diffuse emission from the Galactic plane. In the second region (outer Galaxy), however, no evidence for a signal is obtained by Milagro and a limit on the integral γ-ray flux is obtained $\Phi(E > 3.5\,\mathrm{TeV}) < 5.0 \times 10^{-11}$ photons $\mathrm{cm}^{-2}\,\mathrm{s}^{-1}\,\mathrm{sr}^{-1}$ (99% CL). Figure 5.8 shows the significance map resulting from the Milagro observations.

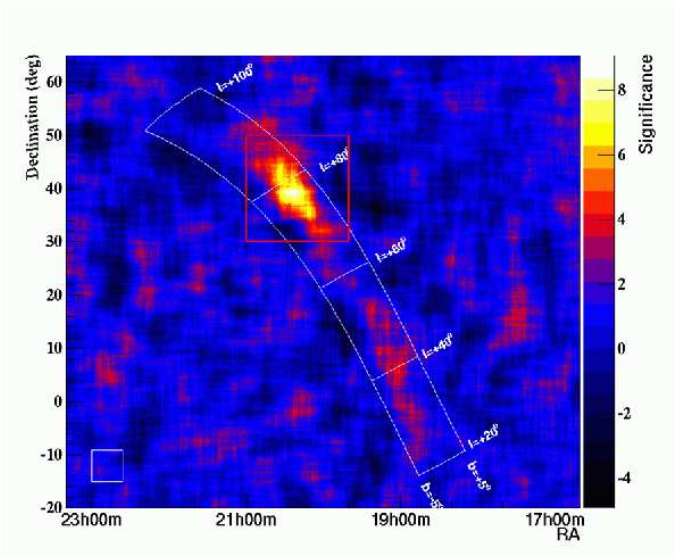

Figure 5.8: Significance map of Milagro extended source survey in the Cygnus arm region [218]. The color scale shows the excess event significance as a function of right ascension (horizontal axis) and declination (vertical axis). Data are binned in 5.9° bins, so neighboring points are highly correlated. The white boxes indicate ranges of Galactic coordinates. The red box is 20° x 20° region around the bin with the greatest significance.

Implications for Galactic CRs

We have already widely reviewed in the first chapter the actual difficulties in interpreting the CR data both in the region $E < 10^{14}$eV and in the UHE regime. VHE γ-rays, conserving their directional information, are the most direct probe of extreme, non-thermal astrophysical sources that could be the production sites of the cosmic rays. The other messengers that could eventually further clarify the issue are the astrophysical neutrinos, and significant progresses are expected also in this field in the next years with the planned km^3 telescopes.

Conventional wisdom holds that the bulk of the cosmic rays up to an energy of 10^{14} eV are produced in supernova remnants (SNRs) in our Galaxy. This wisdom comes in part from the issue of energetics – SNRs are perhaps the only Galactic source with sufficient luminosity to power and replenish the cosmic rays – and in part from the fact that we see strong evidence in X-ray data for non-thermal acceleration of particles to TeV energies in SNR shocks. By 2003, evidence for VHE γ-ray emission from a small number of SNRs had been presented, but the significances for these detections were marginal. After ICRC05, strong detections of numerous SNRs were reported by several instruments, most notably HESS, and it now appears unambiguous that SNRs are important sources of VHE γ-radiation. A very significant step forward has been taken towards demonstrating that SNRs are in fact the primary sites of high-energy cosmic ray production.

The numerous X-ray and VHE γ-ray measurements clearly show that supernova remnants accelerate particles to energies of 50 TeV and possibly higher. The question remains what fraction of the energetic particles are electrons and what fraction are protons and at the moment the two model remains untangled. The evidence for strong magnetic field amplification in young SNRs from the observation of steep synchrotron spectra and sharp features observed in X-rays supports the scenario that electrons could in principle be the source of the VHE γ-ray emission, but this scenario would required magnetic fields that are generally not supported by the X-ray data or the models. Then, despidte the numerous progresses more accurate gamma data (or, possibly the detection of the neutrino contribution) are required to clarify the issue.

An intriguing possibility resides also in the possible production of VHE γ-rays from dark matter in the form of supersymmetric WIMPs through the neutralino annihilation process. The galactic center, where dark matter is expected to cluster significantly is a natural candidate to search for DM emission. Unluckily, just its strong matter density accompanies a strong astrophysical emission that form an heavy background for dark matter searches.

We will return on this issue in the next chapter suggesting an alternative DM emission search based on the anisotropies expected in extragalactic gamma-ray background.

5.3.3 Extragalactic Sources

Extragalactic sources have been key components of the observing program for VHE γ-ray telescopes for many years. In fact, it is fair to say that until 2004, most of the exciting developments in the field came from observations of extragalactic sources, especially active galactic nuclei (AGN) of the blazar variety.

Blazars (quasars and BL Lacertae, or BL Lac, objects) are important objects that have strong and variable emission at most wavelengths where they are detected. Relativistic jets can be seen, or inferred, in many blazars and the sources often exhibit optical polarization and superluminal motion. The general model for a blazar is one involving a supermassive (10^6–$10^9\,M_\odot$) black hole surrounded by an accretion disk. Matter falling towards the black hole powers the hot accretion disk and perpendicular, highly collimated jets. Blazars are thought to be those AGN whose jets are aligned towards the direction of Earth, and the VHE γ-rays are presumably produced from acceleration processes involving protons and electrons in the jets. The nature of jets (how they form, their composition, their zones of emission, etc.) are a key astrophysical puzzle. In particular, a key question is whether the dominant beam particles are electrons, that produce X-rays via synchrotron radiation and TeV γ-rays via inverse-Compton processes, or protons, that produce TeV γ-rays in cascades resulting from the interactions of protons with ambient radiation fields or material. Previous VHE observations have established that blazars have strong and highly variable γ-ray emission,

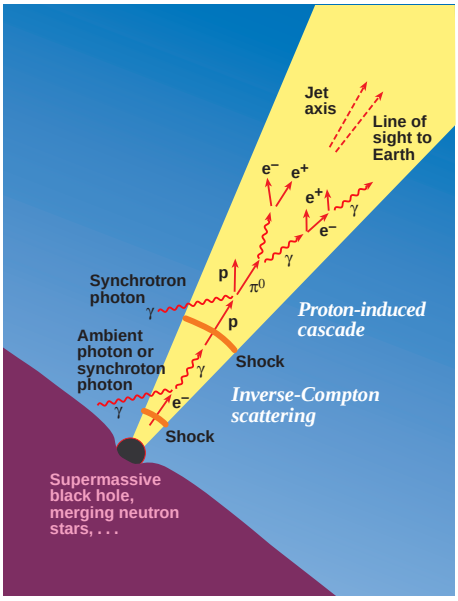

Figure 5.9: Artist's conception of the acceleration processes in a blazar [175]. Black hole accretion powers relativistic jets of aterial. In the jets, electrons or protons are accelerated to high energies via shocks. High energy γ-rays are produced from the inverse-Compton scattering of electrons or from cascades initiated by protons.

that their emitted power is dominated by their high-energy emission, that changes in the TeV emission are often directly correlated with changes in the X-ray emission, and that the sources generally have power-law spectra extending out to 10 TeV (with possible curvature at the higher energies).

Other potential extragalactic VHE γ-ray sources include AGN other than blazars (i.e. radio galaxies such as FR1 and FR2 and radio-quiet spirals such as Seyferts), gamma-ray bursts (GRBs), galaxy clusters, dwarf galaxies, and starburst galaxies.

An important consideration for extragalactic observations is the potential impact on the detected γ-ray flux from interaction with the extragalactic background light (EBL). The EBL is the total radiation from normal star formation and radiation from dust in the infrared(IR)/optical/ultraviolet(UV) bands, integrated over the luminosity history of the universe. Gamma rays in the 50 - 5000 GeV range will interact with EBL photons via the pair-production process. Since the EBL density is poorly known at the present time, there is promise that spectral measurements of extragalactic sources at a number of redshifts could better determine the density and perhaps constrain cosmological models that impact on the evolution of the EBL. Possible absorption effects in the VHE γ-ray spectra from the sources Markarian 421 (Mrk 421), Markarian 501 (Mrk 501), and H 1426+428 have been previously discussed, but a general interpretation has not yet been established.

The VHE source catalog of extragalactic objects is shown in Table 5.2. There are currently 11 reasonably well-established sources; ten of these are blazars and one is the radio galaxy M87. Four the blazars, PKS 2005-489, H 2356-309, 1ES 1218+304, and 1ES 1101-232, were discovered in the last year and presented at ICRC 2005. Three of these sources are the most distant objects yet detected at very high energies.

Gamma Ray Bursts

Gamma Ray Bursts (GRBs), discovered serendipitously in the 1960's, are among the most fascinating and enigmatic objects in all of high-energy astrophysics. By demonstrating that GRBs were isotropic in their arrival distribution, BATSE, onboard the Compton Gamma Ray Observatory, gave credence to the idea that GRBs were cosmological in origin. However, the wide non-uniformity of GRBs, in terms of their fluxes, light curves, and spectra, have made their characterization difficult. A key breakthrough was achieved later by the Beppo-SAX satellite which produced accurate GRB positions and carried out X-ray follow-up observations that enabled multi-wavelength observations of the afterglow emission from the class of longer (and softer) GRBs. Redshift measurements of the optical counterparts of GRBs indicate

Source Type	2003 Sources	2005 Sources	Redshift
Starburst Galaxy	NGC 253		0.002
Radio Galaxy	M87	M87	0.004
Blazar	Markarian 421	Markarian 421	0.031
	Markarian 501	Markarian 501	0.034
	1ES 2344+514	1ES 2344+514	0.044
	1ES 1959+650	1ES 1959+650	0.047
		PKS 2005-489	0.071
	PKS 2155-304	PKS 2155-304	0.116
	H 1426+428	H 1426+428	0.129
		H 2356-309	0.165
		1ES 1218+304	0.182
		1ES 1101-232	0.186

Table 5.2: Extragalactic VHE sources [176]. A comparison between the VHE extragalactic sources established in 2003 and in 2005. All blazars are of the BL Lac type. The sources are ordered by their redshift values. There are a total of 11 extragalactic sources in the current VHE γ-ray catalog.

that the longer ones are indeed cosmological with a typical redshift value of $z \sim 1$. Indeed, it is now realized these GRBs are likely the most energetic explosions in the universe, with inferred outputs between 10^{51} to 10^{54} ergs. It is now generally accepted that GRBs are a strongly beamed phenomena, and that when beaming is taken into account their outputs generally cluster near 10^{51}ergs.

Although a great deal is uncertain about the mechanisms behind GRBs, a general paradigm regarding the long bursts has emerged that starts with the explosion of a massive star (collapsar), followed by the rapid formation of a highly relativistic jet. Particle acceleration is carried out by relativistic shocks in the jet, whereby internal shocks produce the prompt emission and then, as the jet collides with the surrounding medium, external shocks produce the afterglow radiation. Many questions regarding GRBs still remain unanswered, including whether they produce significant amounts of very high-energy γ-ray emission. Numerous models predict strong emission at energies up to hundreds of GeV and beyond, however, so far there has only been one detection by EGRET of a photon above 10 GeV.

Searches for VHE emission from GRBs or their afterglows have been made by numerous ground-based instruments. To date, there has been no convincing evidence for such emission. The main satellite instruments that currently

detect GRBs are HETE-2, INTEGRAL, and Swift. Launched in November 2004, the Swift GRB mission is detecting an unprecedented number of bursts with excellent positional information. Ground-based instruments searching for VHE emission include atmospheric Cherenkov telescopes, air shower arrays, and neutrino telescopes.

Air shower arrays have a high duty cycle and wide FOV that enable them to observe GRBs during their phase of prompt emission. However, the current instruments have substantial collection areas above 1 TeV, reducing the likelihood that they would detect signals from most of the long GRBs that are at cosmological distances.

Atmospheric Cherenkov telescopes have relatively low energy thresholds and high sensitivity, but small fields of view. They are thus well suited for follow-up observations of the afterglows of triggered GRBs. Various groups like MAGIC and STACEE reported on the observations of satellite triggered GRB, starting typically few minutes after the alert. No evidence for VHE γ-ray emission has been reported till now, though these efforts indicate the significant potential of this new generation of Cherenkov telescopes.

Chapter 6

The Signature of the Large Scale Structures on the very-high energy gamma-ray sky

If the diffuse extragalactic gamma ray emission traces the large scale structures of the universe peculiar anisotropy patterns are expected in the gamma ray sky. We use mock N-body catalogues of of large scale structure complemented with the halo model to predict the statistical features of the expected signatures. Interestingly, at very high-energy and large angular scales, correlations with local structures should be prominent. We provide detailed predictions of the signal based on the PSCz map of the local universe. The results are largely independent from cosmological details because of the cutoff distance introduced by the absorption of 0.1-10 TeV photons on the infrared/optical background. The chances to unveil the nature of the sources of the diffuse gamma ray emission and to shed light on the optical/infrared background is discussed, on the light of present and future space and ground based observatories.

6.1 Introduction

Gamma ray astronomy is a flourishing field in astroparticle physics as we have briefly reviewed in previous chapter. At TeV energies, a few dozen sources have been detected mainly by air Cherenkov experiments, most of which are high energy counterparts of MeV-GeV sources in the EGRET catalog. The 0.1–10 TeV range represents one of the "last" photonic windows yet to be explored at large distances. Starting from an energy of about 100 GeV (which we shall refer to as very-high energy, VHE), the absorption of high energy photons onto the extragalactic background light (EBL) via pair-production introduces an energy-loss horizon of the order of a few hundreds Mpc or smaller, well below the size of the observable Universe. This horizon drops

down to ∼10 kpc at PeV energies, basically precluding deep space astronomy with photons above about 10 TeV. Far from being only a limitation, this phenomenon also allows the use of γ-ray astronomy to probe the EBL, which is otherwise difficult to study directly.

Besides single sources, wide field of view instruments and satellite-based observations are sensitive to diffuse γ-ray emissions. A particularly interesting emission is the extragalactic diffuse γ-ray background (in the following, cosmic gamma background, or CGB). The CGB is a superposition of all unresolved sources emitting γ-rays in the Universe and provides an interesting signature of energetic phenomena over cosmological time-scales. While a clear detection of this background has been reported by the EGRET mission [178], its origin is still uncertain, despite the fact that many models have been proposed. The most likely contribution is the one from unresolved blazars, i.e. beamed population of active galactic nuclei [219], with (probably sub-leading) components from ordinary galaxies [220], clusters of galaxies [221], and gamma ray bursts [222]. However, exotic possibilities like dark matter annihilation have been proposed, that are compatible with existing data and constraints [223; 224; 225; 226]. It is extremely difficult to test such models as long as the only observable is the energy spectrum. Recently, it was proposed to use the peculiar small-scale anisotropy encoded in the MeV-GeV gamma sky to probe dark matter [227] or astrophysical [228; 229] contributions to the CGB. In this work, we further study this topic, with particular emphasis on the large scale anisotropy in the energy range 0.1-10 TeV. The lower part of this range will be probed by the GLAST telescope [230; 231], while the energy window above the TeV is in principle accessible to EAS detectors. Different candidates to explain the CGB predict distinctive large scale features, even when similar energy spectra are expected. This is a consequence of the combined effect of a cutoff distance after which VHE γ can travel undamped to us, and of the anisotropic distribution of matter in the local universe (i.e., within a few hundred Mpc from us). A similar anisotropy pattern in the the ultra-high energy cosmic ray sky has been analyzed in chapter 3. The main goal of this chapter is to characterize various features of the CGB which may be used for diagnostics at VHE. In particular, the energy dependence and angular power spectra are analyzed in detail vs. energy for two typical diffuse background models in which underlying gamma emitters correlate linearly with large scale structures (as possibly for unresolved astrophysical sources) and quadratically with the cosmic structures density anisotropies (like in the case of dark matter annihilation emission or a strongly biased astrophysical population of sources).

The paper is structured as follows. The parametrization we use for the

CGB, based on EGRET data, is summarized in Sec. 6.2. In Sec. 6.4 we introduce our treatment of cosmic large scale structures: a mock catalogue derived from a dark matter N-body simulation and the 3D power spectrum derived from the Halo Model of non-linear clustering [232; 233; 234; 245], . With these tools, we shall argue that in the VHE range, especially at the largest angular scales, the predictions mostly depend on the large scale structure in the local neighborhood of the Universe. We shall then use the PSCz astronomical catalogue as tracer of the real structures in the nearby universe, thus producing maps of the VHE gamma sky (Sec. 6.5). In Section 6.6 we analyze the prospects for detection of these features of the forthcoming satellite GLAST, and for EAS observatories like MILAGRO. In Sec. 6.7 we summarize our findings, and conclude. In Sec. 6.3 we provide some details on the parametrization of the EBL, and on the method we use to propagate of gamma rays to calculate attenuation effects. Appendix 6.8 reviews some statistical properties of a discrete poisson process on the sphere, relevant for our estimates of the errors of the multipole maps.

6.2 The cosmic gamma background

Experimentally, the CGB is the most difficult component of the diffuse emission to study. Indeed, it is not correct to assume that the isotropic component after extracting point-like sources plus the galactic diffuse emission is entirely extragalactic: even in the pole direction, the CGB is comparable to the Galactic contribution. The deduced CGB thus depends on the adopted model of the Galactic background. The analysis undertaken to derive the spectrum of the CGB based on EGRET data provided the intensity spectrum [178]

$$I(E_\gamma) = k_0 \left(\frac{E}{0.451\mathrm{GeV}} \right)^{-2.10\pm0.03} \tag{6.1}$$

valid from $E \sim 10$ MeV to $E \sim 100$ GeV, where $k_0 = (7.32 \pm 0.34) \times 10^{-6}\mathrm{cm}^{-2}\mathrm{s}^{-1}\mathrm{sr}^{-1}\mathrm{GeV}^{-1}$. Interestingly, it shows a spectral index remarkably close to the average one of γ-ray blazars detected by EGRET, -2.1 ± 0.3 [235]. EGRET experimental points and the best fit curve are shown in Fig. 6.1.

It is worthwhile to comment that the foreground subtraction remains a delicate issue, as can be appreciated by the reanalysis of the data performed in [236], based on a revised model for the galactic propagation of cosmic rays. The deduced extragalactic spectrum is significantly lowered with respect to Eq. (6.1) at intermediate energies, while closer to the original result of Eq. (6.1) at the lowest and highest energy points. Since the

removal of the isotropic galactic emission from the diffuse gamma background is an open problem, and we still lack a complete understanding of the sources of the CGB, we shall simply base our following analysis on the extrapolation of the spectrum of Eq. (6.1) by one to two orders of magnitude. Actually, the anisotropy pattern in the CGB sky itself may help in the foreground removal. Recently, it was proposed to use the cosmological Compton-Getting effect (whose dipole direction and amplitude are basically energy-independent) to discriminate the truly extragalactic fraction from the galactic foreground [237].

When extrapolating the EGRET flux to higher energy attenuation effects must be taken into account. It is well known that the propagation of photons in the extragalactic background light (EBL) is a crucial issue for gamma astronomy in the VHE range. Absorption of VHE photons through pair-production on CMB or infrared/optical photons distorts an initial source spectrum, in particular by steepening its high energy tail. Astronomy of gamma ray emitters like blazars and active galaxies requires then an accurate modelling of photon propagation and of the background frequency distribution. In the next section we provide a detailed description of the model of the EBL used, and on the treatment of absorption effects. For an overview of the knowledge of the EBL we refer the reader to the review [238]. The expression for the flux intensity in a generic cosmology is given by (see e.g. [239])

$$I(E_\gamma, \hat{n}) \propto \int_0^\infty \mathrm{d}z \, \frac{\rho^\alpha(z, \hat{n})\, g[E_\gamma(1+z)]\, e^{-\tau(E_\gamma, z)}}{H(z)\,(1+z)^3}, \tag{6.2}$$

where we assumed an universal spectrum for the source, $g(E)$, E_γ is the energy we observe today, $\rho(z, \hat{n})$ is the density of sources in the direction $\hat{n}$ at the redshift z, and the Hubble function is written in terms of the present value of the Hubble constant H_0 and of the matter and cosmological constant energy densities as $H(z) \equiv H_0 \sqrt{\Omega_M (1+z)^3 + \Omega_\Lambda}$. The quantity $\tau(E_\gamma, z)$ is the optical depth of photons to absorptions via pair production on the EBL (see appendix 6.3). For most of the following considerations the normalization in the spectrum is irrelevant. Wherever needed (e.g. to estimate the statistics which can be collected by a given experiment) we shall fix the normalization of Eq. (6.2) so that it matches the EGRET fit of Eq. (6.1) at 10 GeV.

For most of what follows it is important to realize that, by looking at VHE, most of the dependence on the cosmology, the source evolution, etc. in Eq. (6.2) cancel out, independently of the index of correlation with density, because of the cutoff at $z \ll 1$ existing for VHE gammas. This important

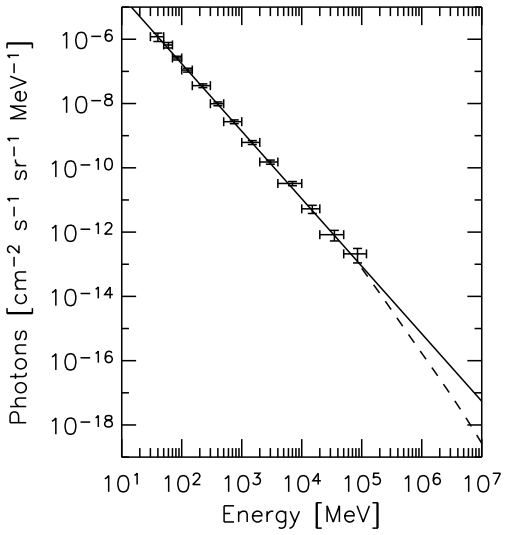

Figure 6.1: EGRET spectrum from [178] and extrapolation up to 10 TeV. The dashed line shows the expected effect of the pair-production attenuation.

property dramatically reduces the model-dependence of the following considerations, differently e.g. from the scenario considered in [227].

It is also worth commenting that the γ-rays of the CGB constitute only a tiny fraction, f_γ, of the cosmic ray flux. When compared with the flux of cosmic rays around the TeV ($I_{\rm CR} = 2.582 \times 10^{-8} (E/{\rm TeV})^{-2.7}$ [240]) and neglecting gamma attenuation effects one gets the upper limit

$$f_\gamma \equiv \frac{I_\gamma}{I_{\rm CR}} \lesssim 2.7 \times 10^{-5} \left(\frac{E}{\rm TeV}\right)^{0.6} . \tag{6.3}$$

Actually, the attenuation of γ's on the EGB cuts the growth of f_γ, which never exceeds 10^{-5}. Note finally that our extrapolation is consistent with existing observational bounds on f_γ at the TeV scale [240].

6.3 Gamma Propagation

Here we report some details on the models used for the extragalactic background light, and on the technique to account for absorption effects in the propagation of photons. The main component of the EBL is the microwave background, which is well known to obey a black-body spectrum

$$n_{\rm CMB}(\epsilon) = \frac{1}{\pi^2 (\hbar c)^3} \frac{\epsilon^2}{\exp\left(\epsilon / T^0_{\rm CMB}\right) - 1} \tag{6.4}$$

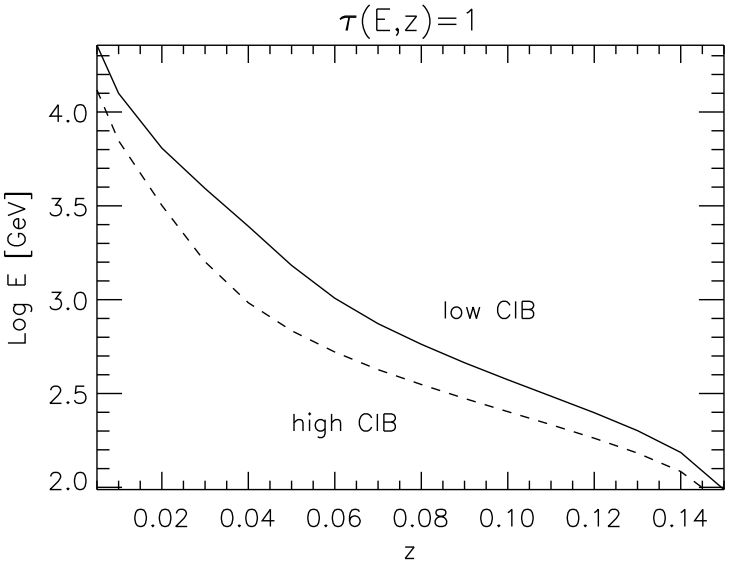

Figure 6.2: Critical optical depth $\tau = 1$ in function of γ-ray energy and redshift. The low CIB case (dashed line) corresponds to Eq. (6.5), while the high CIB case corresponds to twice that value.

where $T^0_{\rm CMB} = 2.73\,{\rm K}{=}2.35{\times}10^{-4}{\rm eV}$ is its present temperature. For the Infrared/Optical Background (CIB), which is the main source of gamma absorption, we use the simple parametrization

$$n_{\rm CIB}(\epsilon) = \begin{cases} 5.42{\times}10^{11}{\rm eV}^{-1}{\rm cm}^{-3}\frac{\epsilon^{3.4}}{\exp(\epsilon/T_F)-1} & \lambda \in 200 \div 2000\,\mu{\rm m}, \\ 7.4{\times}10^{-4}{\rm eV}^{-1}{\rm cm}^{-3}\epsilon^{-2.295} & \lambda \in 6.0 \div 200\,\mu{\rm m}, \\ 7{\times}10^{-3}{\rm eV}^{-1}{\rm cm}^{-3}\frac{e^{-\epsilon}}{\epsilon} & \lambda < 6.0\,\mu{\rm m}, \end{cases} \tag{6.5}$$

where $T_F = 13.6\,{\rm K}$; and the $\lambda - \epsilon$ conversion factor is given by $\lambda(\mu{\rm m}) = 1.24/\epsilon({\rm eV})$. This is a conservative estimate of the CIB consistent with data and constraints reported in [238].

The time evolution of the backgrounds is obtained simply by redshifting, so that:

$$n(\epsilon, z) = (1+z)^2 n_0 \left[\frac{\epsilon}{1+z}\right]. \tag{6.6}$$

This result is exact for the CMB that can is a truly primordial background, while for CIB one should in principle perform a simulation of the star formation and dust clustering that produced this background in the recent past. However accurate modelling of this process suggests that most of the background formed in a burst at $z \simeq 4-5$ near the peak of star formation rate

so that for our purposes (propagation till $z \simeq 0.2$) simple redshifting is quite accurate [238].

In principle, the interaction of high energy photons with the EBL is a complex process in which the e^-e^+ created through pair production interact again with background photons via inverse Compton scattering producing new high energy γ's. We have developed our own code for calculating the evolution of gamma cascades, along the lines of Ref. [259] (which we address to for the details, including the general formalism of cascade propagation). Fortunately, we find that the complicated regime where the cascade of high energy e^+, e^-, and γ has to be followed in details for calculating the final energy distribution is only attained for energies $> 10^{15}$ eV. In the TeV range relevant for gamma astronomy the development of the shower via secondary particle dynamics can be safely neglected, and the observed flux can be calculated simply considering an energy-dependent depletion factor for the spectrum in addition to the effect of the redshift. Thus, if the spectrum at the source is of the form $g(E)$, the observed spectral shape of the signal will be

$$g(E_\gamma) \propto g[E_\gamma(1+z)]\mathcal{P}(E_\gamma, z), \tag{6.7}$$

where E_γ is the energy we observe today and $\mathcal{P}(E_\gamma, z)$ is the probability for a photon emitted at redshift z to survive without interacting till now, when it reaches us with energy E_γ. This probability is written as

$$\mathcal{P}(E_\gamma, z) \equiv e^{-\tau(E_\gamma, z)}, \tag{6.8}$$

where the optical depth τ is

$$\tau(E_\gamma, z) \equiv \int_0^z \mathrm{d}z' \frac{c}{(1+z')H(z')} \int \mathrm{d}\epsilon\, n(\epsilon, z') \int \mathrm{d}\mu \frac{1-\mu}{2} \sigma_{\mathrm{PP}}(E_\gamma(1+z'), \epsilon, \mu), \tag{6.9}$$

that is the rate of pair production of photons on the EBL integrated over the time while propagating from redshift z to 0. The function $\sigma_{\mathrm{PP}}(E, \epsilon, \mu)$ is the theoretically and experimentally well-known pair production cross section of a photon of energy E impinging over a background photon of energy ϵ with a cosinus of the impact angle given by μ. In Fig. 6.2 we show the derived critical $\tau(E_\gamma, z) = 1$ contour that represents the gamma redshift horizon as a function of the energy. We find a satisfactory agreement of the function τ we computed with more detailed studies including the CIB distribution and evolution from simulations of star and galaxy formation [260].

6.4 Tracers of the large scale structure

Since the sources of the CGB are unknown (this is especially true for its high energy component of interest here) to predict the anisotropy pattern in the VHE sky we must start from some assumption on the distribution of the sources. In the following, we shall assume that the sources of the CGB follow the LSS distribution of the matter. Starting from Eq. (6.2), the integral flux above the energy $E_{\rm cut}$ at Earth is simply written as

$$F(E_{\rm cut}, \hat{n}) \propto \int_0^\infty {\rm d}z \, \frac{\rho^\alpha(z, \hat{n})}{H(z)\,(1+z)^3} W(E_{\rm cut}, z)\,, \tag{6.10}$$

where we have defined the window function

$$W(E_{\rm cut}, z) \equiv \int_{E_{\rm cut}}^\infty {\rm d}E \, g[E(1+z)]\, e^{-\tau(E_\gamma, z)}. \tag{6.11}$$

In the limit where the effective cutoff $z_c \ll 1$, the integrals become almost independent on the cosmology, and the previous expressions simplify considerably into

$$W(E_{\rm cut}, z) \simeq \int_{E_{\rm cut}}^\infty {\rm d}E \, g(E)\, e^{-\tau(E_\gamma, z)} \tag{6.12}$$

$$F(E_{\rm cut}, \hat{n}) \propto \int {\rm d}z \, \rho^\alpha(z, \hat{n})\, W(E_{\rm cut}, z)\,, \tag{6.13}$$

where z is directly proportional to the distance, $r \simeq c\,z/H_0$. In particular we shall assume in the following the power-law $g(E) \propto E^{-2.1}$, which on the theoretical side is consistent with a Fermi-shock acceleration mechanism, and observationally matches both the average spectral index of blazar and the spectra of the CGB measured by EGRET, see Eq. (6.1). In the next section, we shall motivate quantitatively that only objects within a few hundred Mpc contribute significantly to the anisotropy pattern in the VHE sky, especially at the large angular scales most relevant for observations. This will allow us to use an astronomical catalogue of objects to predict the pattern in the sky to look for, going beyond the level of statistical predictions only.

N-Body Simulations – Our primary tool to compute the statistical properties of the matter density distribution is a N-body catalogue. This offers the advantage compared to observations of being virtually free of most of the bias affecting astronomical catalogues (no extinction regions, no selection effects, no galaxy morphology and color bias, etc). On the other hand, to obtain reliable results one should carefully consider the types of bias introduced

by the simulation, like the algorithm used, the minimum scale resolved, and the physical content and processes treated in the numerical experiment.

We have performed a set of pure dark matter N-body simulations with a standard ΛCDM universe, a periodic box size of 800 Mpc h^{-1}, and resolutions of 512^3 and 768^3 particles using the GADGET2 code [241; 242]. The initial conditions were computed using second order Lagrangian perturbation theory [243]. Placing the observer at an arbitrary point in the box, we have computed the density on logaritmically spaced spherical shells. A smoothed density field $\rho(z, \hat{n})$ is reconstructed with an adaptive algorithm whose smoothing length varies depending on the local number density of dark matter particles. After obtaining the window functions for different energy cuts and different models of the CIB, the sky map of the integral gamma ray flux above the cut is calculated by integration along radial lines of sight, both considering a source density proportional to ρ or ρ^2. We have checked that the resolution used in the simulation is sufficient to suppress shot noise from undersampling and other numerical artifacts, by comparing the power spectrum extracted at different resolutions. The resulting maps $F(E_{\rm cut}, \hat{n})$ are obtained on a Healpix grid, facilitating the use of standard tools from CMB physics to compute the final power spectrum and multipole coefficients C_l [244].

Halo Model – In order to check the results of the N-body simulations, we compared the C_l's obtained in the case of linear correlations with the predictions of the Halo model [232; 233; 234]. This model is known to provide a fast and efficient semi-analytical recipe for describing the LSS clustering and of its evolution. Comprehensive reviews of the model can be found in [245; 246]. Basically, starting from the 3D power spectra $P(k)$ provided by the model, where k is the wavenumber, the observable angular power spectrum of the gamma sky is obtained by a weighted projection along the line of sight, where the window function of Eq. (6.11) is used as weight. In the Limber approximation the angular power spectrum simply reads

$$C_l = \frac{1}{N_w^2} \int \frac{dr}{r^2}\, W^2(E_{\rm cut}, r)\; P\left(k = \frac{l}{r}, r\right) \tag{6.14}$$

where the factor $N_w = \int \mathrm{d}r\, W(E_{\rm cut}, r)$ represents then the contribution from the mean intensity $\langle F(E_{\rm cut})\rangle$, where an additional dependence from the distance r is added in $P(k, r)$ to take into account redshift evolution. The C_l's can be interpreted as the angular power spectrum of the adimensional gamma intensity emission $\left[F(E_{\rm cut}, \hat{n}) - \langle F(E_{\rm cut})\rangle\right] / \langle F(E_{\rm cut})\rangle$, provided that we retain the normalization $W(E_{\rm cut}, 0) = 1$ and calibrate $P(k, r)$ to the value given by galaxy survey or N-body simulations.

Results

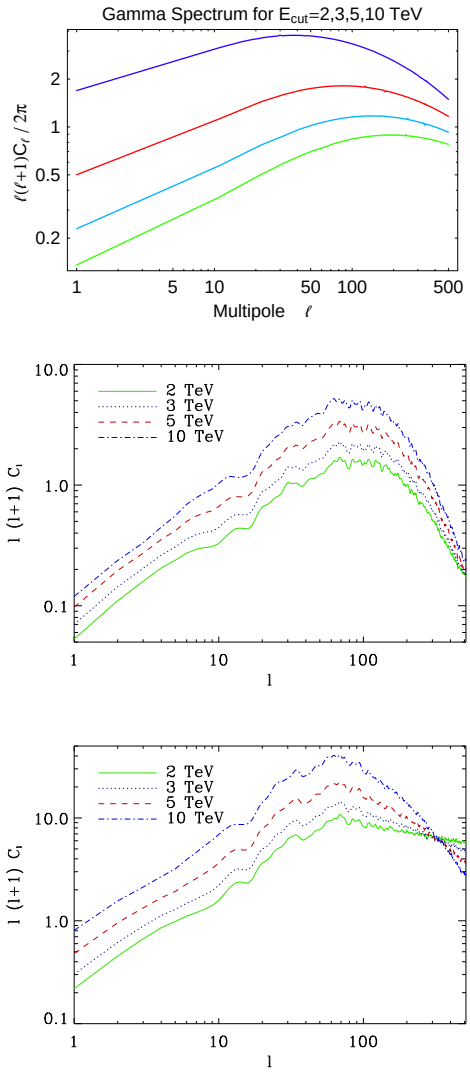

Figure 6.3: Analytical linear (a) and N-body linear (b) and quadratic (c) angular spectra for energy cut $E_{\rm cut} = 2, 3, 5, 10$ TeV.

A comparison of Halo Model spectra with the ones obtained for various energy cuts from the N-body catalogue is shown in in the two top panels in Fig. 6.3. We see that the agreement is generally good, apart discrepancies at very low and large l, which are due to the the break of validity of the Limber approximation and/or to the inadequacy of the Halo Model for predictions on very large scales . In the lower panel, we present the angular spectrum for the hypothesis of a quadratic correlation with density. Both in the linear

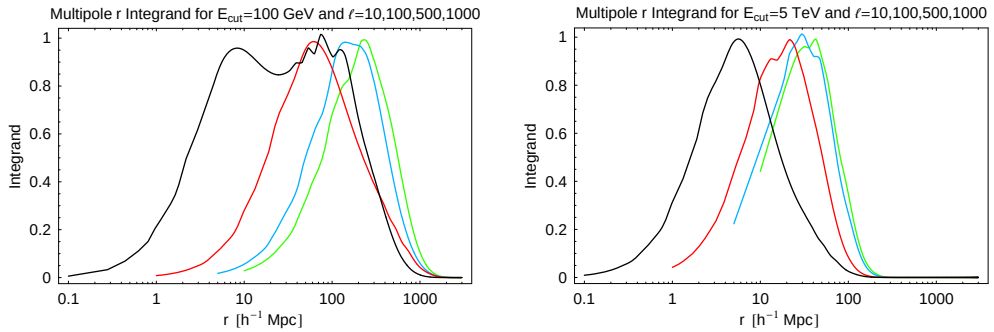

Figure 6.4: Integrand contributions (linear in $\log r$) for the multipoles $l = 10, 100, 500, 1000$ (respectively, black, red, blue, green) and $E_{\rm cut} = 100$ GeV, 5 TeV. Normalization is arbitrary.

and quadratic case, the two most interesting features are the presence of a peak (deriving from the peak of the 3D power spectrum) and of growing normalization of the anisotropies with growing energy cut. At relatively large scales, the anisotropies are contributed by the near structures, which are therefore poorly affected by the shrinking of the pair-production energy loss horizon. The isotropic or small-scale varying component of the flux has instead a significant contribution from far objects, which are cutted away at high energies. The main difference between the linear and the quadratic cases is clearly in the normalization of the spectrum. In the latter scenario the intensity of the anisotropies is enhanced, due to the effect of the clumpiness. Also, note a difference in the shape and position of the peak in the spectrum in practice, the sensitivity to the square of the density restricts further the effective horizon for gammas with an effect similar to the increasing of the energy cut.

We turn now to study how shells at different distances r contribute to the various multipoles. Using the predictions of the halo model, in Fig. 6.4 we plot the integrand $r^{-2}\ W^2(E_{\rm cut}, r)\ P(k = l/r)$ vs. r for the two energy cuts $E_{\rm cut}$ =100 GeV, 5 TeV and for different l. Note that even for $E_{\rm cut} =$ 100 GeV, the C_l's at $l = 10 - 100$ mostly depend from the contribution of structures within a radius of $\simeq 600$ Mpc so that the finite size of the N-body simulation box does not affect our conclusions, and we can use it to confirm this expectation. Even more interestingly, the dominant contribution to the first multipoles at $l = 1 - 10$ comes from within a distance of only ~ 300 Mpc. Within such distances astronomical catalogues with a large field of view exist, providing the actual distribution of matter in the universe, and not only a statistical information on the density field. Thus, one may aim at the study of the pattern of the first few multipoles a_{lm}'s or, equivalently,

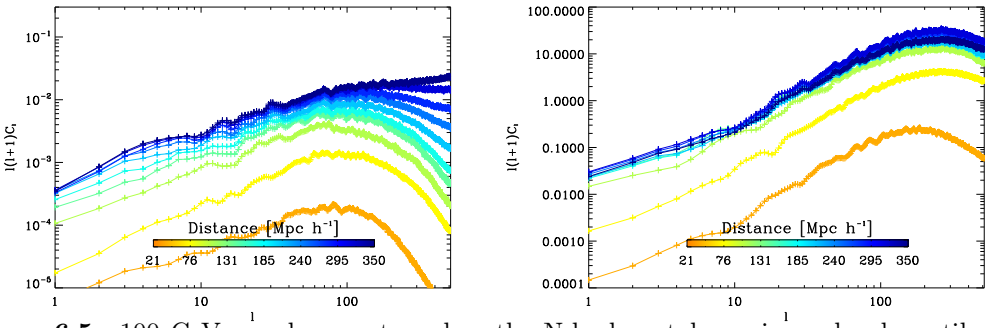

Figure 6.5: 100 GeV angular spectra when the N-body catalogue is used only until a maximum distance R as function of R. Shown are the linear (top) and quadratic (bottom) density correlation case.

of the anisotropy map smoothed to the appropriate resolution. This point is further illustrated with the help of the N-body simulation. In Fig. 6.5 we plot the cumulative contribution to the C_l's in function of the maximum distance used in the catalogue, i.e. derived from Eq. (6.13) when cutting the integral defining $F(E_{\rm cut}, \hat{n})$ to a distance R. The linear and quadratic cases are shown, assuming $E_{\rm cut}$=100 GeV (at higher energies, the effect is even more pronounced). Indeed, the simulation confirms that the convergence to the asymptotic value is faster at low l's than at the higher ones. Effectively, for $l \lesssim 10 - 20$ one can look for correlations between the gamma sky and known structures in the local large scale structures.

6.5 Sky maps

In the recent years, modern galaxies surveys like the Sloan Digital Sky Survey [143; 144] have greatly improved our knowledge of the distribution of galaxies at large scales, revealing a typical foam-like pattern of "filaments and walls" of galaxies around large cosmological voids. These very high quality data are not well suited for our analysis due to the tiny fraction of sky surveyed, while we need to perform comparisons with the large sky field of view of GLAST and of EAS instruments. In this respect, a fair compromise is offered by the IRAS PSCz catalogue [140].

The PSCz catalogue contains about 15,000 galaxies and related *spectroscopic* redshifts with a well understood completeness function out to $z \sim 0.1$. In the limit of uniform emission, above $E = 100\,\mathrm{GeV}$ the majority of the CGB flux is expected to come from within this distance. The sky coverage of the catalogue is about 84%; the incompleteness is mainly due to the so called zone of avoidance centered on the galactic plane and caused by the galactic

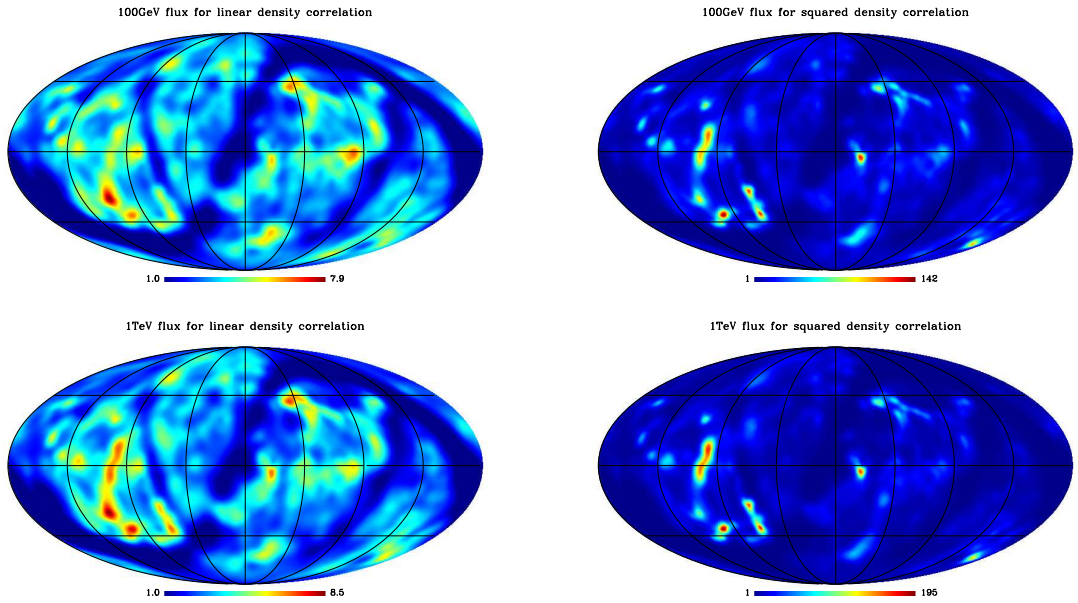

Figure 6.6: Equatorial sky maps for the linear (left) and quadratic (right) density correlation and for $E_{\rm cut} = 100$ GeV and 1 TeV. The color scale is linear. The maps represents the gamma contribution only until z=0.1 (the PSCz contribution). The normalization is arbitrary but consistent among the various maps; the global minimum outside the mask is set to 1 in each plot.

extinction and to a few, narrow stripes which were not observed with enough sensitivity by the IRAS satellite. These regions are excluded from our analysis with the use of the binary mask available with the PSCz catalogue itself. However, the mask region does not represent a major limitation for present analysis, since the galactic emission at low galactic latitudes outshines the CGB anyway, prohibiting any CGB analysis in this region.

We closely follow Ref. [166] for the treatment of the selection effects of the catalogue, parameterized via the selection function $\phi(z)$. Differently from Ref. [166], we do not sum source by source to obtain the final gamma sky map; instead, we use the approach of constructing a smoothed density field $\rho(z, \hat{n})$ through the same adaptive algorithm we employed in the analysis of the N-body simulation. This method has the advantage of efficiently suppressing the intrinsic catalogue shot noise at high redshifts allowing us to use the catalogue sources until $z = 0.1 \simeq 300$ Mpc h^{-1}. Given the low redshift, we can safely use Eqs. (6.12, 6.13), with the only caveat of replacing $W(E_{\rm cut}, z) \to W(E_{\rm cut}, z)/\phi(z)$, to take into account selection effects. To study the sensitivity to the bias of the gamma sources with respect to the

baryonic density, we shall consider both values $\alpha = 1$ and $\alpha = 2$, i.e. a linear and quadratic correlations. The latter is in particular expected for dark-matter annihilation models [247; 248; 249; 250; 224; 251]

In Fig. 6.6 we plot the resulting maps from the PSCz catalogue in equatorial coordinates for the linear and quadratic density correlation and for $E_{\rm cut} = 100$ GeV and 1 TeV. Let's discuss first the linear case. For the case of the map with $E_{\rm cut} = 100$ GeV, modulo the "hole" due to the mask the pattern is quite isotropic, with some hot spots like e.g. from the Virgo and Perseus Clusters. Other structures which appear are the Shapley concentration and the Columba cluster (for a key of the local cosmological structures see [166] or [252]). The intensity of anisotropies is of the order of % (see next). Given the limited statistics of GLAST at high energies, the TeV map is only of interest for the EAS gamma detectors like MILAGRO. We see in this case that the nearest structures, forming the Super-galactic Plane, dominate. Of course, from the Northern emisphere (where all the present or planned EAS instruments are located) only the upper part of the map is visible. Here, the Virgo Cluster and the Perseus cluster offer the strongest anisotropy, greater than 10%(see next).

For the quadratic case the change in quite evident: the effect of the quadratic correlation, as already observed for the power spectra, is to give more power to the nearest structures (the Virgo and Centaurus cluster) that, in fact, are almost dominating the map. It is instructive to look at the case of Shapley concentration at $z \simeq 0.04$ that gives an important contribution in all the linear cases but that almost disappears in the quadratic maps. The anisotropy in the quadratic case is quite pronounced (100%, as it is clear from the scale near the map) and should be easily detectable. Provided that the dark matter is responsible for a relevant fraction of the CGB (see e.g. [225; 226]), this is an important signature for indirect dark matter searches.

6.6 The potential of forthcoming instruments

In order to estimate the chances of detection of the structures previously described by the current or next generation of instruments, one may proceed as follows. First, given the specifics of an experiment (in particular its field of view, effective area and background rejection capability) one calculates the expected number of events and of misidentified cosmic ray background events $(N_\gamma, N_{\rm CR})$ under different assumptions for the $E_{\rm cut}$ and the EBL. The events falling in the mask region must be subtracted from the $(N_\gamma, N_{\rm CR})$ data used for the analysis, so that the incomplete sky coverage is taken into account. One then generates $\mathcal{N}$ samples of N_γ events from the VHE γ map

and $N_{\rm CR}$ from an isotropic one. These $\mathcal{N}$ realizations may then be used to perform quantitative statements, like for example the confidence level with which a given instrument is expected to distinguish between the structured sky we predict and an isotropic one, or between linear and quadratic correlation scenarios, or between scenarios characterized by a different model of CIB. This would be essentially the generalization of the approach followed in [166]. Here, however, for the sake of clarity we prefer to develop a simplified analysis in terms of the multipole coefficients, a_{lm}, with an analytic estimate of the expected errors due to shot noise effects (see Appendix 6.8). Performing full Monte Carlo analyses for a few relevant cases we checked that the errors thus estimated basically agree with the ones correctly calculated. In this approach, first we fit the sky maps obtained outside the mask via the harmonic expansion

$$F_{10}(E_{\rm cut},\hat{n}) = \sum_{lm}^{l_{\rm max}=10} a_{lm} Y_{lm}(\hat{n}). \tag{6.15}$$

As a second step, by knowing the statistics and the characteristics of the detector one can estimate the expected errors on the a_{lm} and eventually on the derived coefficients C_l's (see Appendix 6.8 for details).

We limit the fit to $l \leq l_{\rm max} = 10$ for several reasons: (i) we have shown that the large scales are mainly sensitive to the local universe, for which our predictions are robust and deterministic; (ii) the lower the l, the higher the signal to noise ratio is, which increases the chances of detection (see below); (iii) the incomplete sky coverage due to the mask is affecting our results, and should be taken into account; however, as long as we restrict the analysis to the large structures (compared with the size of the mask cut) the bias is small. Quantitatively, the method is robust against variations in $l_{\rm max}$ as long as the related angular scale $\vartheta_{\rm min} = \pi/l_{\rm max}$ is greater than the typical angular extension of the mask cut. More important, the purpose of the harmonic analysis is to reliably assess the sensitivity of a given experiment; to this aim a small bias in the a_{lm}'s is acceptable (we do not want to estimate the true a_{lm}'s, but the detectability of them, even if the biased ones). Of course, in the analysis of the real data it will be preferable to directly look for cross correlations with the full maps like the ones in Fig. 6.6, whose electronic version is available from the authors upon request.

In the following, we shall consider two kinds of instruments: Satellite-based missions, and in particular GLAST [253], and extensive air shower experiments like TIBET [254], ARGO [206], MILAGRO [255], or planned observatories like HAWC [208]. Unfortunately, ACT instruments like HESS or MAGIC are not well suited for such kind of searches, given the small field

Experiment	$A_{\rm eff}$ (cm^2)	$\Omega_{\rm fov}$ (sr)	DC	$g_{\rm cut}$	$h_{\rm cut}$	range
GLAST[253]	10^4	2.4	∼90%	∼1	∼.06 f_γ	$E \lesssim$ 0.5-1 TeV
MILAGRO[255]	$\gtrsim 10^7$	~ 2	$> 90\%$	0.5	0.08	E ∼1–20 TeV
HAWC[208]	$\sim 10^{8.5}$	∼2	$> 90\%$	0.5	0.08	E ∼0.3–10 TeV

Table 6.1: The characteristics of the experiments considered in our estimates. The fraction of the sky observable by a given experiment $f_{\rm sky}$ is needed for our estimate of the errors, see Appendix 6.8.

of view, the low duty cycle, and the relatively high impact of the variability of the instrumental and atmospheric conditions on the rate of diffuse signals.

Denoting by $I(E_\gamma)$ the extrapolated EGRET flux which accounts for attenuations (see section 6.2), one can estimate the number of events, N_γ, above the energy E_γ to be collected in the time t as

$$N_\gamma = t \cdot g_{\rm cut} \cdot DC \cdot \Omega_{\rm fov} \cdot f_{\rm m} \cdot \int_{E_\gamma}^{\infty} {\rm d}E\, A_{\rm eff}(E) I_\gamma(E)\,, \qquad (6.16)$$

where: DC is the duty-cycle of the instrument; $\Omega_{\rm fov}$ is the solid angle of the field of view; $f_{\rm m} < 1$ is the useful fraction of the sky due to the presence of the galactic mask; $g_{\rm cut}$ is the fraction of γ's passing the actual cuts; $A_{\rm eff}(E)$ is the effective collecting area of the instrument (averaged over the field of view of the instrument). In the following, we shall assume $f_{\rm m} = 0.84$ due to the mask in the PSCz catalogue, but the actual value may differ. The previous formula assumes a quasi-isotropic γ sky. This assumption may be violated to some extent at the multi-TeV energies of interest for EAS detectors. Even in this case, right ascension anisotropies would not affect the estimate, and only large latitude anisotropies might affect N_γ by a factor of $\mathcal{O}(1)$. This is acceptable enough since we shall only perform a parametric study of the performances of an EAS observatory. Analogously, the CR background can be estimated as

$$N_{\rm CR} = t \cdot h_{\rm cut} \cdot DC \cdot \Omega_{\rm fov} \cdot f_{\rm m} \int_{E_\gamma}^{\infty} {\rm d}E\, A_{\rm eff}(E) I_{\rm CR}(E), \qquad (6.17)$$

with clear meaning of the symbols. Note that we consider the same area for CRs as for γ's, although a differential performance of the instrument may be taken into account by properly rescaling the factor $h_{\rm cut}$. The typical parameters we shall use are taken from existing literature, and reported in Tab. 6.1. Note that GLAST is expected to have an excellent background identification,

so that only cosmic rays in the amount of $\sim 6\%$ of the gamma flux pass the cuts. On the other hand, EAS experiments have a poor rejection capability (some of them like TIBET [254] have none), which increases typically the gamma content of the diffuse flux by no more than one order of magnitude. Therefore one should keep in mind that even after gamma/hadron separation, the anisotropies of the gamma sky have to be identified against a *quasi*-isotropic background which is $\gtrsim 10^4$ larger than the gamma flux.

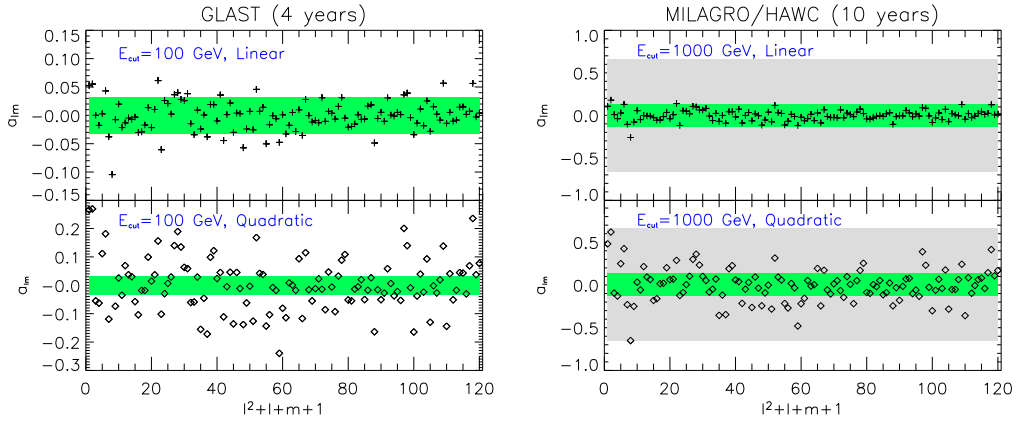

Figure 6.7: The coefficients a_{lm} up to $l_{\max} = 10$ calculated from the PSCz gamma maps of Fig. 6.6. The shaded band shows the 1-σ shot noise error given by Eq. (6.23); in the right panel the inner shaded region refers to HAWC, the outer one to MILAGRO. We report the predictions for both the linear and quadratic cases.

In Fig. 6.7 we report the coefficients a_{lm}'s up to $l_{\max} = 10$ calculated from the PSCz gamma maps of Fig.6.6, with the errors estimated according to what reported in Appendix 6.8. The GLAST mission is expected to last 5+5 years (so we plot a realistic 4 years exposure), while EAS instruments have longer run times, so we plot the expectations for a decade of collecting time by MILAGRO, or by the proposed project HAWC. GLAST should be able to detect some structures above 100 GeV at the 2σ level, even if the correlation with matter density is only linear. For a quadratic correlation one expects a more robust detection, and possibly even hints for anisotropies at higher energies*. On the contrary, instruments like MILAGRO may find hints of structures (at the 1 σ level, see gray band in the right panel of Fig. 6.7) only if correlations are quadratic or in any case strongly biased with overdensities. As a technical remark, note that the performances of MILAGRO above the TeV were estimated by using an effective area $A_{\rm eff}(E_\gamma) \simeq 10^{7.1}\,{\rm cm}^2$ (see e.g.

*Our estimate does not include the fraction of the CGB measured by EGRET which may be resolved by GLAST. If this is removed, our predictions should be rescaled accordingly.

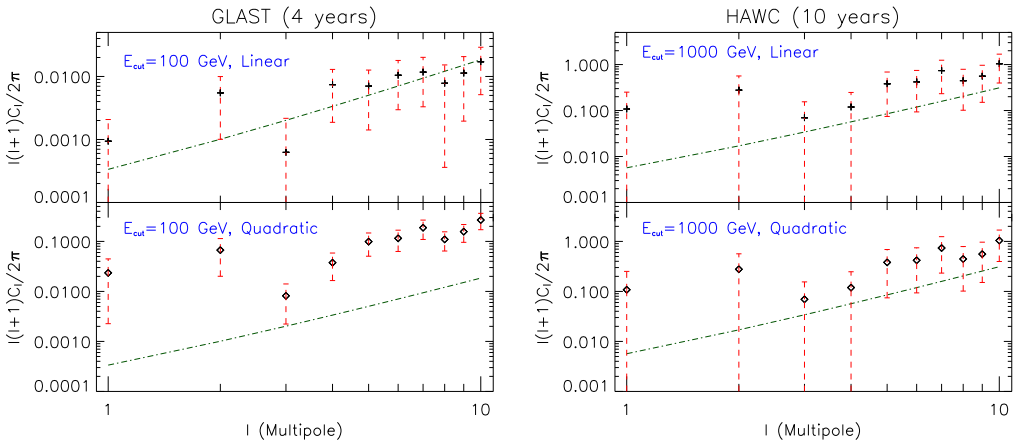

Figure 6.8: The coefficients C_l up to $l_{\max} = 10$ calculated from the PSCz gamma maps of Fig. 6.6. We shown the level of shot noise [see Eq. (6.22)] expected from four years of GLAST and one decade of HAWC. We report the predictions for both the linear and quadratic cases.

[208]). A proper treatment should take into account the energy-dependence of the area, and calculate the expected sky maps for MILAGRO weighting accordingly the integral maps. Given the limited chances of this instrument to detect the features we have described, we consider this simple estimate sufficient to illustrate our point. It is worth to stress that for an EAS detector the error on the a_{lm}'s scales as $\sqrt{N_{\rm CR}}/N_\gamma$. Therefore the reduction of the shot-noise error goes like $(t \cdot A_{\rm eff})^{-1/2}$ (both $N_{\rm CR}$ and N_γ grow linearly with $t \cdot A_{\rm eff}$), or equivalently as $\sqrt{h_{\rm cut}}/g_{\rm cut}$: improving the exposure is equally important as improving the gamma/hadron separation capability. A simple inspection of Fig. 6.7 reveals that for a realistic detection of the features in the VHE sky one would need the improvement in effective area planned to be reached by instruments like HAWC [208] (see inner green band in the right panel of Fig. 6.7). An instrument like ARGO [206] is expected to have performances in between MILAGRO and HAWC, and may have some chance especially if a significant improvement comes with respect to the hadron rejection. Also, note that due to their altitude HAWC and ARGO have a significant acceptance of sub-TeV events. While the gamma/hadron separation is less efficient at lower energies, the higher statistics may help in revealing these structures.

In Fig. 6.8 we plot the expectations for GLAST and HAWC in terms of the C_l coefficients. At the large scales we are focusing on cosmic variance makes any detection of the C_l's challenging even when the corresponding

a_{lm}'s are easily detectable. This proves the importance of the deterministic nature of the expected anisotropies in the flux: for comparison, despite the larger statistics available at lower energies, the detection of the C_l's at low l studied in [227] is precluded by the cosmic variance.

Since our predictions are shaped by the nearby universe, for a fixed background the absolute value of the detected anisotropy in principle measures the index of the correlation of gamma sources with respect to the matter, as clearly shown by the comparison of the top and lower panels in both Fig. 6.7 and Fig. 6.8. On the other hand, a partial degeneracy exists with the intensity of the infrared background. However, both the study of single sources and of the energy spectrum of the CGB should pin down the remaining uncertainty on this quantity, and the corresponding degeneracy should eventually be broken.

Finally, let's note that these estimates are somewhat conservative: summing the power at different l's may favor the detection (see e.g. [229]), and cross-correlating directly with the maps would eventually exploit all the information. Therefore, once the data on the CGB become available, reassessing the detection issue with a detailed study will be mandatory.

6.7 Summary and Conclusions

The universe is pervaded by diffuse backgrounds of low-energy photons, of cosmological origin like the CMB or due to stellar activity, like the optical and infrared background (CIB). This extragalactic background light makes the universe opaque to energetic γ's. The most energetic part of the gamma-ray background (CGB) is thus of primary importance for high energy astroparticle physics, since it acts as a "cosmic calorimeter". Besides telling us about the integrated history of the most powerful astrophysical accelerators of the universe, it may constrain non-standard physics taking place at high energy, even much higher than the GeV-TeV scale. As an example, we remind that the most stringent limits on the decays of superheavy particles coupled at the tree-level *only to neutrinos* come from the observed diffuse extragalactic γ-ray flux [258].

In this work we have studied the anisotropy pattern of the CGB in the very-high energy regime, beyond about 100 GeV. Due to the onset of the pair-production losses of VHE photons on the CIB, most of the flux is coming from local structures, within $z \lesssim 0.1$. In particular at the largest angular scales, the pattern and *the amplitude* of the anisotropies are almost independent from the energy spectral shape of the sources and from the cosmological model: modulo the magnitude of the CIB, the key parameter in shaping the

signature is the degree of the correlation of the gamma-emitters with the known matter density field in the nearby universe. In particular, dark matter annihilation models for the origin of most of the CGB predict a strong (quadratic) correlation of the flux with the matter density, which should clearly manifest in the forthcoming observations. Looking for dark matter signatures at VHE is promising since, despite the limited statistics, the predictions are more robust than the ones at low energy and small scales (see e.g. [227]), which are affected by more astrophysical and particle physics uncertainties, besides the cosmic variance.

Starting from the PSCz astronomical catalogue, we produced maps of the VHE gamma sky and estimated the potential of the satellite mission GLAST or of extensive air shower observatories to detect these features. The GLAST mission should be able to detected the imprint of dark matter signatures at large scales, if the annihilation product of these exotic particles constitute any relevant fraction of the diffuse extragalactic flux. EAS experiments are instead limited by the scarce cosmic ray rejection capabilities, and only the next generation of instruments like HAWC (or maybe already ARGO) may have real chances to achieve the needed sensitivity. For EAS experiments, there is a further remark. The SK experiment has recently detected an anisotropy at the level of few$\times 10^{-4}$ in the cosmic rays around 10 TeV, from a sample of about 2×10^8 muons [257] (MILAGRO has also detected this effect, as mentioned in [217]). At similar or higher energies, the TIBET collaboration has reported the detection of several anisotropies at the $\sim 0.1\%$ level in the cosmic ray flux, probably associated with galactic sources and/or galactic transport [210]. While the exposure needed to reveal the features we have discussed so far is within the reach of the next generation of EAS instruments, even assuming an excellent control over experimental spurious effects, the ultimate limitation in detecting these signatures comes from the understanding of the intrinsic anisotropy in the CR background. Therefore, an efficient gamma/hadron separation is not only necessary to enhance the statistical significance of the point-like or diffuse gamma ray sources observed by EAS instruments, but also to control systematics. In particular, reversing the gamma cut and thus enriching the sample in hadronic showers may help identifying and removing non-gamma anisotropies.

6.8 Appendix: Summary of the properties of noise

In this section we briefly review the noise properties of a discrete poisson process on the sphere. The main results can be easily obtained analytically and concern the amplitude of the noise variance and the related power spectrum. The map resulting from a random realization of N equally weighted points can be written as $f(\hat{\Omega}) = 4\pi/N \sum_i \delta(\hat{\Omega} - \hat{\Omega}_i)$, normalized to its mean value, so that to be adimensional; then the harmonic expansion coefficients $a_{lm} = \int d\hat{\Omega} f Y_{lm}(\hat{\Omega})$ follow (apart the constant monopole contribution) a gaussian distribution with $\langle a_{lm} \rangle = 0$ and

$$\sigma^2_{a_{lm}} = \langle a^2_{lm} \rangle = \frac{4\pi}{N} \tag{6.18}$$

independent from l, m. From this, the spectrum of the shot noise $C_l = \sum_m |a_{lm}|^2/(2l+1)$ follows a χ^2 distribution with mean

$$\langle C_l \rangle = \frac{4\pi}{N} \tag{6.19}$$

again independent of l, and variance

$$\sigma^2_{C_l} = \langle C_l^2 \rangle - \langle C_l \rangle^2 = \left(\frac{4\pi}{N}\right)^2 \frac{2}{2l+1}. \tag{6.20}$$

These results surely hold in the limit of large statistics; however for our applications it is worth testing them also in the limit of very low statistics, say for $N \leq 1000$. We performed a set of Monte Carlo simulations to clarify the issue an found that the simulations and analytic results are in perfect agreement even in the completely unphysical limit of $N = 10$; the analytical results can then be safely used in all the cases of interest.

In general, in addition to the white noise C_l^N, one has a signal C_l^S. Moreover, there is normally incomplete sky coverage, and additional white noise may be present, as in our case because of the background due to cosmic rays passing the cuts[†]. A generalization of Eq. (6.20) then reads

$$\sigma^2_{C_l} = \frac{2}{(2l+1) f_{\rm sky}} (C_l^S + C_l^N)^2, \tag{6.21}$$

[†]In principle, the formulae should receive a correction at large l due to the finite angular resolution of the experiment. Since the experimental resolutions are better than a degree, and we limit our considerations to the most prominent signatures at large scales, this correction is unnecessary for our application.

where $f_{\rm sky}$ is the fraction of the sky accessible to the experiment (assumed with uniform acceptance over this region), and the noise spectrum C_l^N (including the cosmic ray background) is given by

$$C_l^N = \frac{4\pi f_{\rm sky}}{N_\gamma}\left[1 + \frac{N_{\rm CR}}{N_\gamma}\right]. \tag{6.22}$$

For the a_{lm}'s, the variance due to the shot-noise plus the background is written as

$$\sigma^2_{a_{lm}} = C_l^N = \frac{4\pi f_{\rm sky}}{N_\gamma}\left(1 + \frac{N_{\rm CR}}{N_\gamma}\right). \tag{6.23}$$

We have used these results in estimating the errors reported in Sec. 6.6. Note that what is really measured is always the sum signal+noise: the noise is an unavoidable component in any experiment. However, being constant in l, m, the average level of the noise can be fitted and subtracted (this is trivial for deterministic predictions since $\langle a_{lm}^N \rangle = 0$). On the other hand, the error in its determination depends on the sensitivity of the experiment and thus the statistics collected, and on the level of background rejection.

Conclusions and outlook

In the first part of this dissertation I have investigated the prospects for using CRs to perform astronomy at the highest energy range actually observed in astro-particle physics. In particular, given the limited statistics available, I focused the attention on the large scale anisotropies expected in the data. A reasonable expectation is that the pattern of UHECR anisotropies should resemble in same way the anisotropies of the cosmological Large Scale Structures from which they likely derive. Moreover, in this scenario, due to the GZK effect, only the very near universe in a sphere of few hundreds Mpc is expected to contribute to the UHECR flux. In the limit in which Cosmological Magnetic Field play a negligible role, this allows to forecast not only the statistical properties of the expected anisotropies but also their pattern on the sky, lowering considerably the statistics required to investigate the model. The detection of the anisotropies in the position and with the intensity expected from LSS would rule out a large class of exotic models in which UHECR are supposed to derive from unconventional sources like topological defects or super-massive particles.

The findings of chapter 3 indicate that a statistics of few hundreds events is necessary to robustly detect this kind of anisotropy or, eventually, to disprove the model. Luckily, this statistics is well within the reach of few years of operation of the Auger Observatory, actually in phase of completion in the country of Mendoza, in the Argentinean Pampas. This forthcoming statistics is expected, definitely, to clarify the issue.

However, though the actual UHECRs statistics amounts only to about 100 events, a first hint of large scale anisotropy has been already detected in the form of prominent (3σ) peak at 20° in the clustering autocorrelation function of the dataset. This result is analyzed in chapter 4, and the signal is nicely explained in the light of the expected anisotropies from the LSS model, whose predictions also explain some other (less statistically significant) features of the data at scales larger than 100°. Likely, the large statistics of the AUGER observatory is required to confirm this result, though this preliminary evidence is quite promising.

The field of γ-astronomy is in a quite advanced phase respect to UHECRs and dozen of galactic and extra-galactic sources have already been detected in the last decade with an almost exponential number increment. Though, many of the potentialities of γ-astronomy await still to be exploited. Among

these, a clear detection of the anisotropies of the cosmological gamma background would be a great progress in the field bringing the attention also to diffuse emissions besides the actual point sources search. Potentially, the diffuse emission contains information on the presence of dark matter in the universe. Though with a very weak rate, DM is expected to self-annihilate producing γ photons. The anisotropy of the resulting diffuse emission has quite different properties from the conventional astrophysical emission. The anisotropies of the extragalactic gamma background could then offer an interesting an complementary tool to investigate DM. The prospects to detect this kind of signal with next generation of satellite and ground-based observatories are pursued in chapter 6. The result of the forecast analysis indicate that the GLAST satellite has, indeed, good chances of detecting the LSS anisotropies and at least, to put strong constraints on the DM emission. Ground based observatories, like the planned large area HAWC are basically limited by their hadron background rejection capabilities though this is partly compensated by the longer integration time allowed. In any case the ground based contribution is indispensable to cover the energy range above ~ 1 TeV, at present not in the reach capabilities of satellites experiments.

High Energy Astronomy is, at present, in a pioneering phase of discovery. A lot of experimental activity in CRs and γ-physics is flourishing providing steadily new pieces of information. Likely, complemented with the birthing discipline of neutrino astronomy, these efforts will allow finally emerge the hidden picture of the High Energy Universe.

Bibliography

[1] S. Eidelman *et al.* [Particle Data Group], "Review of particle physics," Phys. Lett. B **592** (2004) 1.

[2] J. W. Cronin, "Cosmic rays: The most energetic particles in the universe," Rev. Mod. Phys. **71** (1999) S165.

[3] L. Anchordoqui, T. Paul, S. Reucroft and J. Swain, "Ultra-high energy cosmic rays: The state of the art before the Auger observatory," Int. J. Mod. Phys. A **18** (2003) 2229 [arXiv:hep-ph/0206072].

[4] M. Nagano and A. A. Watson, "Observations And Implications Of The Ultrahigh-Energy Cosmic Rays," Rev. Mod. Phys. **72** (2000) 689.

[5] X. Bertou, M. Boratav and A. Letessier-Selvon, "Physics of extremely high energy cosmic rays," Int. J. Mod. Phys. A **15** (2000) 2181 [arXiv:astro-ph/0001516].

[6] S. Yoshida and H. Dai, "The extremely high energy cosmic rays," J. Phys. G **24** (1998) 905 [arXiv:astro-ph/9802294].

[7] P. Biermann and G. Sigl, "Introduction to cosmic rays," Lect. Notes Phys. **576** (2001) 1 [arXiv:astro-ph/0202425].

[8] F. Ferrari and E. Szuszkiewicz, "Cosmic ray recipes," arXiv:astro-ph/0601158.

[9] R. W. Clay, Z. Kurban and N. R. Wild, *Cosmic Ray Related Undergraduate Experiments*, GAP Note 1998-061 (Technical and Scientific Notes about the Pierre Auger Project), http://www.auger.org/tech.html.

[10] M. Takeda *et al.* [AGASA Collaboration], "Extension of the cosmic-ray energy spectrum beyond the predicted Greisen-Zatsepin-Kuzmin cutoff," Phys. Rev. Lett. **81**, 1163 (1998) [astro-ph/9807193].

[11] S. Yoshida *et al.*, "The Cosmic ray energy spectrum above 3 x 10**18-eV measured by the Akeno Giant Air Shower Array," Astropart. Phys. **3** (1995) 105.

[12] N. Hayashida *et al.*, "Observation of a very energetic cosmic ray well beyond the predicted 2.7-K cutoff in the primary energy spectrum," Phys. Rev. Lett. **73** (1994) 3491.

[13] Proc. of International Symposium on *Extremely High Energy Cosmic Rays: Astrophysics and Future Observatories*, ed. M. Nagano (Institute for Cosmic Ray Research, Tokyo, 1996)

[14] Proc. *24th International Cosmic Ray Conference* (Istituto Nazionale Fisica Nucleare, Rome, Italy, 1995)

[15] S. C. Corbato *et al.*, "HiRes: A High resolution Fly's Eye detector,"Proc. of the International Workshop on Techniques to Study Cosmic Rays with Energies Greater than 10^{19} eV, Paris, Nucl. Phys. Proc. Suppl. **28B** (1992) 36.; D. J. Bird, et al., in Ref. [14], Vol. **2**, 504; Vol. **1**, 750; M. Al-Seady, et al., in Ref. [13], p. 191
see also http://hires.physics.utah.edu/

[16] T. Abu-Zayyad *et al.* [HiRes-MIA Collaboration], "Measurement of the cosmic ray energy spectrum and composition from 10**17-eV to 10**18.3-eV using a hybrid fluorescence technique," Astrophys. J. **557** (2001) 686 [arXiv:astro-ph/0010652].

[17] T. Antoni *et al.* [The KASCADE Collaboration], "KASCADE measurements of energy spectra for elemental groups of cosmic Astropart. Phys. **24** (2005) 1 [arXiv:astro-ph/0505413].

[18] R. J. Rand and S. R. Kulkarni, *Ap. J.* **343** (1989), 760.

[19] D. J. Bird *et al.* [Fly's Eye Collaboration], "Evidence for correlated changes in the spectrum and composition of cosmic rays at extremely high-energies," Phys. Rev. Lett. **71**, 3401 (1993).

[20] D. J. Bird *et al.* [Fly's Eye Collaboration], "The Cosmic ray energy spectrum observed by the Fly's Eye," Astrophys. J. **424**, 491 (1994).

[21] D. J. Bird *et al.* [Fly's Eye Collaboration], "Detection of a cosmic ray with measured energy well beyond the expected spectral cutoff due to cosmic microwave radiation," Astrophys. J. **441**, 144 (1995).

[22] K. Greisen, "End To The Cosmic Ray Spectrum?," Phys. Rev. Lett. **16**, 748 (1966).

[23] G. T. Zatsepin and V. A. Kuzmin, "Upper Limit Of The Spectrum Of Cosmic Rays," JETP Lett. **4**, 78 (1966) [Pisma Zh. Eksp. Teor. Fiz. **4**, 114 (1966)].

[24] D. R. Bergman [HiRes Collaboration], "Observation of the GZK cutoff using the HiRes detector," arXiv:astro-ph/0609453.

[25] R. W. Clay, A.G. K. Smith and J. L. Reid, *Publ. Astron. Soc. Aust.* **14** (1997), 195.

[26] L. Landau, I. Pomeranchuk, *Dokl. Akad. Nauk. SSR* **92** (1953) 535.; A. B. Migdal, *Phys. Rev.* **103** (1956) 1811.

[27] S. J. Sciutto, "Air shower simulations with the AIRES system," arXiv:astro-ph/9905185.

[28] J. N. Capdevielle *et al.*, "The Karlsruhe extensive air shower simulation code CORSIKA," Karlsruhe preprint KfK 4998 (1992); J. Knapp, D. Heck, preprint KfK 5196 (1993).

[29] A. M. Hillas, *Proc. 19th ICRC (La Jolla)*, **1** (1985) 155.

[30] R. Engel, *Xth Int. Symposium on Very High Energy Cosmic Rays Interactions*, Gran Sasso (1998).

[31] H. O. Klages *et al.*, "The KASCADE Experiment," Nucl. Phys. Proc. Suppl. **52B**, 92 (1997).

[32] R. S. Fletcher, T. K. Gaisser, P. Lipari and T. Stanev, "SIBYLL: An Event generator for simulation of high-energy cosmic ray cascades," Phys. Rev. D **50**, 5710 (1994).

[33] K. Werner, "Strings, pomerons, and the venus model of hadronic interactions at ultrarelativistic energies," Phys. Rept. **232**, 87 (1993).

[34] N. N. Kalmykov and S. S. Ostapchenko, "The Nucleus-Nucleus Interaction, Nuclear Fragmentation, And Fluctuations Of Extensive Air Showers," Phys. Atom. Nucl. **56**, 346 (1993) [Yad. Fiz. **56N3**, 105 (1993)].

[35] J. Ranft, "DPMJET versions II.3 and II.4: Sampling of hadron hadron, hadron nucleus and nucleus nucleus interactions at cosmic ray energies according to the dual parton model description of the model and code manual," INFN-AE-97-45

[36] J. Knapp, "High-energy interactions and extensive air showers," arXiv:astro-ph/9710277. T T. Antoni *et al.* [KASCADE Collaboration], "Test of high-energy interaction models using the hadronic core of EAS," J. Phys. G **25** (1999) 2161 [arXiv:astro-ph/9904287].

[37] A. D. Erlykin and A. W. Wolfendale, "On the problem of determining the mass composition of cosmic rays derived from air shower measurements," Astropart. Phys. **9** (1998) 213.

[38] K. Greisen, *Ann. Rev. Nucl. Sc.* **10** (1960) 63.
K. Suga, *Proc. 5th Interamerican Seminar on Cosmic Rays*, La Paz (Bolivia) 1962.

[39] G. L. Cassiday, Ann. Rev. Nucl. Part. Sci. **35** (1985) 321.

[40] Linsley, "Evidence for a Primary Cosmic-Ray Particle with Energy 10**20 eV", Phys. Rev. Lett. **10**, 146 (1963).

[41] M. A. Lawrence, R. J. O. Reid and A. A. Watson [Haverah Park Collaboration], "The Cosmic ray energy spectrum above 4x10**17-eV as measured by the Haverah Park array," J. Phys. G **17**, 733 (1991).

[42] M. M. Winn *et al.*[SUGAR Collaboration], "The Cosmic Ray Energy Spectrum Above 10**17-Ev," J. Phys. G **12**, 653 (1986).

[43] B. N. Afanasiev *et al*, *Proc. of the 24th ICRC*, Rome, Italy **2** (1995) 756.

[44] J. W. Cronin, Nucl. Phys. Proc. Suppl. **28B**, 213 (1992); The Pierre Auger Observatory Design Report (2^{nd} edition), March 1997; see also `http://www.auger.org/`.

[45] Y. Arai *et al.*, "The Telescope Array experiment: An overview and physics aims," Proceedings of 28th ICRC (2003), Tsukuba.

[46] P. Sokolsky, *Introduction to Ultra High Energy Cosmic Ray Physics* (Addison Wesley, Frontiers in Physics, 1989), Chapter 3.

[47] T. K. Gaisser *et al.* [HIRES Collaboration], "Cosmic ray composition around 10**18-eV," Phys. Rev. D **47** (1993) 1919.

[48] B. Z. Kopeliovich, N. N. Nikolaev and I. K. Potashnikova, "Rising Cross-Sections In QCD And The Cosmic Ray Data," Phys. Rev. D **39** (1989) 769.

[49] P. Sokolsky *et al.* [HIRES Collaboration], "The Cosmic Ray Composition Above 0.1-Eev: Highlight Talk," *Prepared for 23rd International Conference on Cosmic Rays (ICRC 23), Calgary, Canada, 19-30 Jul 1993*

[50] Kalmykov N N et al, 1995, Proc. 24th ICRC, 1, 123.

[51] Elbert J W & Gaisser T K, 1979, Proc. 16th ICRC, 8, 42.

[52] N. Hayashida *et al.* [AGASA Collaboration], "Muons (>= 1-GeV) in large extensive air showers of energies between 10**16.5-eV and 10**19.5-eV observed at Akeno," J. Phys. G **21** (1995) 1101. See also: `www.icrr.u-tokyo.ac.jp/as/project/agasa.html`.

[53] B. R. Dawson, R. Meyhandan and K. M. Simpson, "A comparison of cosmic ray composition measurements at the highest energies," Astropart. Phys. **9** (1998) 331 [arXiv:astro-ph/9801260].

[54] F. Halzen *et al*, *Astropart. Phys.* **2** (1995) 151.

[55] K. S. Capelle, J. W. Cronin, G. Parente and E. Zas, "On the detection of ultra high energy neutrinos with the Auger Observatory," Astropart. Phys. **8** (1998) 321 [arXiv:astro-ph/9801313]. P. Billoir, "Neutrino capabilities of the AUGER detector", *8th International Workshop on Neutrino Telescopes*, Venice, 1999; S. Coutu, X. Bertou, P. Billoir, "Ultra-high energy neutrinos with Auger", *John Hopkins Workshop (Neutrinos in the Next Millenium)*, 1999.

[56] Antoni T et al. - KASCADE collaboration 2005 *Astrop. Phys.* **24** 1

[57] A. Haungs, "Air Shower Measurements in the Primary Energy Range from PeV to EeV," arXiv:astro-ph/0610677.

[58] P. Bhattacharjee and G. Sigl, "Origin and propagation of extremely high energy cosmic rays," Phys. Rept. **327** (2000) 109 [arXiv:astro-ph/9811011].

[59] L. N. Epele and E. Roulet, "Comment on *On the origin of the highest energy cosmic rays*," Phys. Rev. Lett. **81** (1998) 3295 [arXiv:astro-ph/9806251].

[60] A. Venkatesan, M. C. Miller and A. V. Olinto, "Constraints on the production of ultra-high-energy cosmic rays by isolated neutron stars," Astrophys. J. **484** (1997) 323 [arXiv:astro-ph/9612210].

[61] R. J. Protheroe "Origin and propagation of the highest energy cosmic rays", Towards the Millennium in Astrophysics: Problems and Prospects, Erice 1996, eds. M.M. Shapiro and J.P. Wefel (World Scientific, Singapore).

[62] L. O'C. Drury, *Rep. Prog. Phys.* **46** (1983) 973.

[63] J. G. Kirk and P. Duffy, "Particle acceleration and relativistic shocks," J. Phys. G **25** (1999) R163 [arXiv:astro-ph/9905069].

[64] A. M. Hillas, "The Origin Of Ultrahigh-Energy Cosmic Rays," Ann. Rev. Astron. Astrophys. **22** (1984) 425.

[65] P. L. Biermann, T. K. Gaisser and T. Stanev, "The Origin of galactic cosmic rays," Phys. Rev. D **51** (1995) 3450 [arXiv:astro-ph/9501001].

[66] A. Vilenkin, E. P. S. Shellard, "Strings and Other Topological Defects", Cambridge Univ. Press, Cambridge, 1994.

[67] T. Vachaspati, "Formation of Topological Defetcs", ICTP summer school on Cosmology (1997), hep-ph/9710292.

[68] T. Vachaspati, "Formation, Interaction and Observation of Topological Defects", Les Houches (1998), astro-ph/9903362.

[69] P. Bhattacharjee, "Ultrahigh Energy Cosmic Rays from Topological Defects — Cosmic Strings, Monopoles, Necklaces, and All That", astro-ph/9803029.

[70] V. Berezinsky, P. Blasi and A. Vilenkin, "Ultra high energy gamma rays as signature of topological defects," Phys. Rev. D **58** (1998) 103515 [arXiv:astro-ph/9803271].

[71] Y. B. Zeldovich, I. Y. Kobzarev and L. B. Okun, "Cosmological Consequences Of The Spontaneous Breakdown Of Discrete Symmetry," Zh. Eksp. Teor. Fiz. **67** (1974) 3 [Sov. Phys. JETP **40** (1974) 1].

[72] V. Berezinsky, "Ultra high energy cosmic rays," Nucl. Phys. Proc. Suppl. **70** (1999) 419 [arXiv:hep-ph/9802351].

[73] P. P. Kronberg, "Extragalactic magnetic fields," Rept. Prog. Phys. **57** (1994) 325.

[74] J. P. Vallée, *Ap. J.* **366** (1991) 450.

[75] *The Pierre Auger Project Design Report*, Fermilab, October 1995 (Web site: `www.auger.org/admin/`).

[76] M. Lemoine, G. Sigl, P. Biermann, "Supercluster Magnetic Fields and Anisotropy of Cosmic Rays above 10^{19} eV", astro-ph/9903124.

[77] G. R. Farrar and T. Piran, "GZK violation: A Tempest in a (magnetic) teapot?," Phys. Rev. Lett. **84** (2000) 3527 [arXiv:astro-ph/9906431].

[78] K. Dolag, D. Grasso, V. Springel and I. Tkachev, "Mapping deflections of Ultra-High Energy Cosmic Rays in Constrained Simulations of Extragalactic Magnetic Fields," JETP Lett. **79**, 583 (2004) [Pisma Zh. Eksp. Teor. Fiz. **79**, 719 (2004)] [astro-ph/0310902]; See also "Constrained simulations of the magnetic field in the local universe and the propagation of UHECRs," JCAP **0501**, 009 (2005) [astro-ph/0410419].

[79] G. Sigl, F. Miniati and T. A. Ensslin, "Ultra-high energy cosmic ray probes of large scale structure and magnetic fields," Phys. Rev. D **70**, 043007 (2004) [astro-ph/0401084]. See also "Cosmic magnetic fields and their influence on ultra-high energy cosmic

ray propagation," Nucl. Phys. Proc. Suppl. **136**, 224 (2004) [astro-ph/0409098].

[80] M. Takeda *et al.*, "Small-scale anisotropy of cosmic rays above 10**19-eV observed with the Akeno Giant Air Shower Array," Astrophys. J. **522** (1999) 225 [arXiv:astro-ph/9902239].

[81] N. Hayashida *et al.* [AGASA Collaboration], "The anisotropy of cosmic ray arrival directions around 10**18-eV," Astropart. Phys. **10** (1999) 303 [arXiv:astro-ph/9807045].

[82] D. J. Bird *et al.* [HIRES Collaboration], "Study of broad scale anisotropy of cosmic ray arrival directions from 2 x 10**17-eV to 10**20-eV from Fly's Eye data," arXiv:astro-ph/9806096.

[83] C. Cesarsky, Proc. of the International Workshop on Techniques to Study Cosmic Rays with Energies Greater than 10^{19} eV, Paris, *Nucl. Phys. B (Proc. Suppl.)* **28B** (1992) 51.
C. Cesarsky, V. Ptuskin, Proc. 23rd ICRC (Calgary), **2** (1993) 341.

[84] M. Kachelrieß, P. D. Serpico and M. Teshima, Astropart. Phys. in press (2006) [astro-ph/0510444].

[85] V. Springel, C. S. Frenk and S. D. M. White, "The large-scale structure of the Universe," Nature **440** (1137) [arXiv:astro-ph/0604561].

[86] V. P. Reshetnikov, "Sky surveys and deep fields of ground-based and space telescopes," arXiv:astro-ph/0603154.

[87] Gott, J. R. I. *et al.* A Map of the Universe. *Astrophys. J.* **624**, 463–484 (2005).

[88] N. A. Bahcall, "Large-scale structure in the universe indicated by galaxy clusters," Ann. Rev. Astron. Astrophys. **26** (1988) 631.

[89] N. A. Bahcall, "Large scale structure of the universe," arXiv:astro-ph/9612046.

[90] Colless, M. *et al.* The 2dF Galaxy Redshift Survey: spectra and redshifts. *Mon. Not. R. Astron. Soc.* **328**, 1039–1063 (2001).

[91] York, D. G. *et al.* The Sloan Digital Sky Survey: Technical Summary. *Astron. J.* **120**, 1579–1587 (2000).

[92] Geller, M. J. & Huchra, J. P. Mapping the universe. *Science* **246**, 897–903 (1989).

[93] Bond, J. R., Kofman, L. & Pogosyan, D. How filaments of galaxies are woven into the cosmic web. *Nature* **380**, 603 (1996).

[94] Springel, V. *et al.* Simulations of the formation, evolution and clustering of galaxies and quasars. *Nature* **435**, 629–636 (2005).

[95] White, S. D. M., Frenk, C. S. & Davis, M. Clustering in a neutrino-dominated universe. *Astrophys. J. Let.* **274**, L1–L5 (1983).

[96] Guth, A. H. Inflationary universe: A possible solution to the horizon and flatness problems. *Physical Review D* **23**, 347–356 (1981).

[97] Starobinsky, A. A. Dynamics of phase transition in the new inflationary universe scenario and generation of perturbations. *Physics Letters B* **117**, 175–178 (1982).

[98] Zwicky, F. Die Rotverschiebung von extragalaktischen Nebeln. *Helvetica Physica Acta* **6**, 110–127 (1933).

[99] Zwicky, F. Nebulae as Gravitational Lenses. *Physical Review* **51**, 290–290 (1937).

[100] Fischer, P. *et al.* Weak Lensing with Sloan Digital Sky Survey Commissioning Data: The Galaxy-Mass Correlation Function to 1 H^{-1} Mpc. *Astron. J.* **120**, 1198–1208 (2000).

[101] Wilson, G., Kaiser, N., Luppino, G. A. & Cowie, L. L. Galaxy Halo Masses from Galaxy-Galaxy Lensing. *Astrophys. J.* **555**, 572–584 (2001).

[102] Clowe, D., Luppino, G. A., Kaiser, N. & Gioia, I. M. Weak Lensing by High-Redshift Clusters of Galaxies. I. Cluster Mass Reconstruction. *Astrophys. J.* **539**, 540–560 (2000).

[103] Van Waerbeke, L. *et al.* Cosmic shear statistics and cosmology. *Astroparticle Physics* **374**, 757–769 (2001).

[104] White, S. D. M., Navarro, J. F., Evrard, A. E. & Frenk, C. S. The Baryon Content of Galaxy Clusters - a Challenge to Cosmological Orthodoxy. *Nature* **366**, 429–433 (1993).

[105] Spergel, D. N. *et al.* First-Year Wilkinson Microwave Anisotropy Probe (WMAP) Observations: Determination of Cosmological Parameters. *Astrophys. J. Suppl.* **148**, 175–194 (2003).

[106] Efstathiou, G., Sutherland, W. J. & Maddox, S. J. The cosmological constant and cold dark matter. *Nature* **348**, 705–707 (1990).

[107] Saunders, W., Frenk, C., Rowan-Robinson, M., Lawrence, A. & Efstathiou, G. The density field of the local universe. *Nature* **349**, 32–38 (1991).

[108] Riess, A. G. *et al.* Observational Evidence from Supernovae for an Accelerating Universe and a Cosmological Constant. *Astron. J.* **116**, 1009–1038 (1998).

[109] Perlmutter, S. *et al.* Measurements of Omega and Lambda from 42 High-Redshift Supernovae. *Astrophys. J.* **517**, 565–586 (1999).

[110] Smoot, G. F. *et al.* Structure in the COBE differential microwave radiometer first-year maps. *Astrophys. J. Let.* **396**, L1–L5 (1992).

[111] de Bernardis, P. *et al.* A flat Universe from high-resolution maps of the cosmic microwave background radiation. *Nature* **404**, 955–959 (2000).

[112] Netterfield, C. B. *et al.* A Measurement by BOOMERANG of Multiple Peaks in the Angular Power Spectrum of the Cosmic Microwave Background. *Astrophys. J.* **571**, 604–614 (2002).

[113] Tegmark, M. *et al.* The Three-Dimensional Power Spectrum of Galaxies from the Sloan Digital Sky Survey. *Astrophys. J.* **606**, 702–740 (2004).

[114] Seljak, U. *et al.* Cosmological parameter analysis including SDSS Lyα forest and galaxy bias: Constraints on the primordial spectrum of fluctuations, neutrino mass, and dark energy. *Physical Review D* **71**, 103515 (2005).

[115] Sunyaev, R. A. & Zeldovich, Y. B. Small-Scale Fluctuations of Relic Radiation. *Astrophys. Space Sci.* **7**, 3–19 (1970).

[116] Davis, M., Efstathiou, G., Frenk, C. S. & White, S. D. M. The evolution of large-scale structure in a universe dominated by cold dark matter. *Astrophys. J.* **292**, 371–394 (1985).

[117] Cen, R., Miralda-Escude, J., Ostriker, J. P. & Rauch, M. Gravitational collapse of small-scale structure as the origin of the Lyman-α forest. *Astrophys. J. Let.* **437**, L9–L12 (1994).

[118] Press, W. H. & Schechter, P. Formation of Galaxies and Clusters of Galaxies by Self-Similar Gravitational Condensation. *Astrophys. J.* **187**, 425–438 (1974).

[119] Lacey, C. & Cole, S. Merger rates in hierarchical models of galaxy formation. *Mon. Not. R. Astron. Soc.* **262**, 627–649 (1993).

[120] Reed, D. S. *et al.* The first generation of star-forming haloes. *Mon. Not. R. Astron. Soc.* **363**, 393–404 (2005).

[121] Abel, T., Bryan, G. L. & Norman, M. L. The Formation of the First Star in the Universe. *Science* **295**, 93–98 (2002).

[122] Kaiser, N. Weak gravitational lensing of distant galaxies. *Astrophys. J.* **388**, 272–286 (1992).

[123] Van Waerbeke, L., Mellier, Y. & Hoekstra, H. Dealing with systematics in cosmic shear studies: New results from the VIRMOS-Descart survey. *Astroparticle Physics* **429**, 75–84 (2005).

[124] Viel, M., Weller, J. & Haehnelt, M. G. Constraints on the primordial power spectrum from high-resolution Lyman α forest spectra and WMAP. *Mon. Not. R. Astron. Soc.* **355**, L23–L28 (2004).

[125] Benson, A. J., Cole, S., Frenk, C. S., Baugh, C. M. & Lacey, C. G. The nature of galaxy bias and clustering. *Mon. Not. R. Astron. Soc.* **311**, 793–808 (2000).

[126] Giavalisco, M. *et al.* The Angular Clustering of Lyman-Break Galaxies at Redshift $z \sim 3$. *Astrophys. J.* **503**, 543–552 (1998).

[127] Baugh, C. M., Cole, S., Frenk, C. S. & Lacey, C. G. The Epoch of Galaxy Formation. *Astrophys. J.* **498**, 504 (1998).

[128] Pierce, A. Dark matter in the finely tuned minimal supersymmetric standard model. *Physical Review D* **70**, 075006 (2004).

[129] Haiman, Z., Mohr, J. J. & Holder, G. P. Constraints on Cosmological Parameters from Future Galaxy Cluster Surveys. *Astrophys. J.* **553**, 545–561 (2001).

[130] Peebles, P. J. E. & Yu, J. T. Primeval Adiabatic Perturbation in an Expanding Universe. *Astrophys. J.* **162**, 815–836 (1970).

[131] Eisenstein, D. J. *et al.* Detection of the Baryon Acoustic Peak in the Large-Scale Correlation Function of SDSS Luminous Red Galaxies. *Astrophys. J.* **633**, 560–574 (2005).

[132] Allen, B. Stochastic gravity-wave background in inflationary-universe models. *Physical Review D* **37**, 2078–2085 (1988).

[133] Lyth, D. H. What Would We Learn by Detecting a Gravitational Wave Signal in the Cosmic Microwave Background Anisotropy? *Physical Review Letters* **78**, 1861–1863 (1997).

[134] R. U. Abbasi *et al.* [The HiRes Collaboration], "Search for point sources of ultra-high energy cosmic rays above 40-EeV using a maximum likelihood ratio test," Astrophys. J. **623**, 164 (2005) [astro-ph/0412617].

[135] B. Revenu [Pierre Auger Collaboration], "First estimate of the primary cosmic ray energy spectrum above 3-EeV from the Pierre Auger observatory," in Proceedings of the 29$^{\rm th}$ ICRC, (2005) Pune India.

[136] E. Waxman, K. B. Fisher and T. Piran, "The signature of a correlation between $>$ 10**19-eV cosmic ray sources and large scale structure," Astrophys. J. **483**, 1 (1997) [astro-ph/9604005].

[137] N. W. Evans, F. Ferrer and S. Sarkar, "The anisotropy of the ultra-high energy cosmic rays," Astropart. Phys. **17**, 319 (2002) [astro-ph/0103085].

[138] A. Smialkowski, M. Giller and W. Michalak, "Luminous infrared galaxies as possible sources of the UHE cosmic rays," J. Phys. G **28**, 1359 (2002) [astro-ph/0203337].

[139] S. Singh, C. P. Ma and J. Arons, "Gamma-ray bursts and magnetars as possible sources of ultra high energy cosmic rays: Correlation of cosmic ray event positions with IRAS galaxies," Phys. Rev. D **69**, 063003 (2004) [astro-ph/0308257].

[140] W. Saunders *et al.*, "The PSCz Catalogue," Mon. Not. Roy. Astron. Soc. **317**, 55 (2000) [astro-ph/0001117].

[141] Jarrett, T.H., Chester, T., Cutri, R., Schneider, S., Skrutskie, M. & Huchra, J. 2000a, AJ, 119, 2498.

[142] Jarrett, T.H., "Large Scale Structure in the Local Universe: The 2MASS Galaxy Catalog," Publ. Astron. Soc. Aust. 21, 396 (2004) [astro-ph/0405069].

[143] York, D. et al. 2000, AJ, 120, 1579

[144] J. K. Adelman-McCarthy *et al.* [SDSS Collaboration], "The Fourth Data Release of the Sloan Digital Sky Survey," astro-ph/0507711.

[145] Peebles, P. J. E. 1980, "The Large-Scale Structure of the Universe" (Princeton, NJ: Princeton University Press)

[146] Sandage, A., Tammann, G. A., & Yahil, A. 1979, "STY luminosity function fitting method", Astrophys. J. 232, 352.

[147] Efstathiou, G., Ellis, R. S., & Peterson, B. S. 1988, *MNRAS*, 232, 431

[148] M. Blanton, P. Blasi and A. V. Olinto, "The GZK feature in our neighborhood of the universe," Astropart. Phys. **15**, 275 (2001) [astro-ph/0009466].

[149] M. Tegmark *et al.* [SDSS Collaboration], "The 3D power spectrum of galaxies from the SDSS," Astrophys. J. **606**, 702 (2004) [astro-ph/0310725].

[150] Davis, M., Meiksin, A., Strauss, M. A., da Costa, L. N., & Yahil, A. 1988, *ApJ*, **333**, L9

[151] Berezinskii,V. and Grigor'eva, S. I. 1988, A&A, 199, 1.

[152] D. N. Spergel *et al.* [WMAP Collaboration], "First Year Wilkinson Microwave Anisotropy Probe (WMAP) observations: Determination of cosmological parameters," Astrophys. J. Suppl. **148**, 175 (2003) [astro-ph/0302209].

[153] L. A. Anchordoqui, M. T. Dova, L. N. Epele and J. D. Swain, "Effect of the 3-K background radiation on ultrahigh energy cosmic rays," Phys. Rev. D **55**, 7356 (1997) [hep-ph/9704387].

[154] M. J. Chodorowski,A. Zdziarski and M. Sikora, Astrophys. J. **400**, 181 (1992).

[155] P. Sommers, "Cosmic Ray Anisotropy Analysis with a Full-Sky Observatory," Astropart. Phys. **14**, 271 (2001) [astro-ph/0004016].

[156] K.B. Fisher *et al.*, Astrophys.J.Suppl. 100, 69 (1995)

[157] N. Hayashida *et al.*, "Updated AGASA event list above 4*10**19-eV," Astron. J. **120**, 2190 (2000) [astro-ph/0008102].

[158] X. Bertou [Pierre Auger Collaboration], "Performance of the Pierre Auger Observatory surface array," astro-ph/0508466, in the Proceedings of the 29$^{\rm th}$ ICRC, (2005) Pune India.

[159] K. Kasahara *et al.* [TA Collaboration], "The Current Status and Prospect of the Ta Experiment," astro-ph/0511177.

[160] R. Tagliaferri, G. Longo, S. Andreon, S. Capozziello, C. Donalek and G. Giordano, "Neural Networks and Photometric Redshifts," astro-ph/0203445.

[161] A. A. Collister and O. Lahav, "ANNz: estimating photometric redshifts using artificial neural networks," Publ. Astron. Soc. Pac. **16**, 345 (2004) [astro-ph/0311058].

[162] E. Vanzella *et al.*, "Photometric redshifts with the Multilayer Perceptron Neural Network: application to the HDF-S and SDSS," astro-ph/0312064.

[163] P. N. Best *et al.*, "The host galaxies of radio-loud AGN: mass dependencies, gas cooling and AGN feedback," Mon. Not. Roy. Astron. Soc. **362**, 25 (2005) [astro-ph/0506269].

[164] P. N. Best, G. Kauffmann, T. M. Heckman and Z. Ivezic, "A sample of radio-loud AGN in the Sloan Digital Sky Survey," Mon. Not. Roy. Astron. Soc. **362**, 9 (2005) [astro-ph/0506268].

[165] M. Kachelrieß and D. V. Semikoz, "Clustering of ultra-high energy cosmic ray arrival directions on medium scales," Astrop. Phys. **26**, 10-15 [astro-ph/0512498].

[166] A. Cuoco, R. D. Abrusco, G. Longo, G. Miele and P. D. Serpico, "The footprint of large scale cosmic structure on the ultra-high energy cosmic ray distribution," JCAP **0601**, 009 (2006) [astro-ph/0510765].

[167] Talk of M. Pravdin at the 29$^{\text{th}}$ ICRC Pune 2005, `http://icrc2005.tifr.res.in/htm/PAPERS/HE14/rus-pravdin-MI-abs1-he14-poster.pdf`

[168] L. A. Anchordoqui *et al.*, "Full-sky search for ultrahigh-energy cosmic ray anisotropies," Phys. Rev. D **68**, 083004 (2003) [astro-ph/0305158].

[169] R. U. Abbasi *et al.* [The High Resolution Fly's Eye Collaboration (HIRES)], "Study of small-scale anisotropy of ultrahigh energy cosmic rays observed in stereo by HiRes," Astrophys. J. **610**, L73 (2004). [astro-ph/0404137].

[170] Talk of S. Westerhoff at the CRIS-2004 workshop "GZK and Surrounding", Catania, Italy, `http://www.ct.infn.it/cris2004/talk/westerhoff.pdf`

[171] V. Berezinsky, A. Z. Gazizov and S. I. Grigorieva, "Dip in UHECR spectrum as signature of proton interaction with CMB," Phys. Lett. B **612**, 147 (2005). [arXiv:astro-ph/0502550].

[172] R. A. Ong, "Very high-energy gamma-ray astronomy," Phys. Rept. **305** (1998) 93.

[173] T. C. Weekes, "VERY HIGH-ENERGY gamma-ray ASTRONOMY," Phys. Rept. **160** (1988) 1.

[174] C. M. Hoffman, C. Sinnis, P. Fleury and M. Punch, "Gamma-ray astronomy at high energies," Rev. Mod. Phys. **71** (1999) 897.

[175] R. A. Ong, "High energy particles from the universe," in *Proc. of the 19th Intl. Symp. on Photon and Lepton Interactions at High Energy LP99* ed. J.A. Jaros and M.E. Peskin, *In the Proceedings of 19th International Symposium on Lepton and Photon Interactions at High-Energies (LP 99), Stanford, California, 9-14 Aug 1999, pp 740-764* [arXiv:hep-ex/0003014].

[176] R. A. Ong, "The status of VHE gamma-ray astronomy," based on the Rapporteur Talk at ICRC 2005 [astro-ph/0605191].

[177] N. Gehrels, C.E. Fichtel, G.J. Fishman, J.D. Kurfess, Volker Schonfelder, Scientific American 269 (1993) 68.

[178] P. Sreekumar *et al.* [EGRET Collaboration], "EGRET observations of the extragalactic gamma ray emission," Astrophys. J. **494**, 523 (1998) [astro-ph/9709257].

[179] M. Boratav, Proc. 25th Int. Cosmic Ray Conf. (Durban), ed. M.S. Potgieter *et al.* (World Scientific, Singapore), **5**, 205 (1997).

[180] A.A. Moiseev *et al.*, Proc. 29th Int. Cosmic Ray Conf., Pune, **5**, 419 (2005).

[181] AGILE web page: http://agile.mi.iasf.cnr.it/

[182] Jackson J.D., Elettrodinamica classica. 2 ed., 2001, Zanichelli

[183] M.F. Cawley, T.C. Weekes, Exp. Astron. 6 (1995) 7

[184] D. J. Fegan, "gamma/hadron separation at TeV energies," J. Phys. G **23** (1997) 1013.

[185] T. Yoshikoshi *et al.*, Proc. 29th Int. Cosmic Ray Conf., Pune, **5**, 343 (2005).

[186] W. Hoffman, Proc. 29th Int. Cosmic Ray Conf., Pune, Review, Rapporteur and Highlight Papers, **10**, 97 (2005).

[187] R. Mirzoyan, Proc. 29th Int. Cosmic Ray Conf., Pune, **4**, 23 (2005).

[188] D. Bose *et al.*, Proc. 29th Int. Cosmic Ray Conf., Pune, **4**, 343 (2005).

[189] V.G. Sinitsyna *et al.*, Proc. 29th Int. Cosmic Ray Conf., Pune, **4**, 395 (2005).

[190] J. Kildea *et al.*, Proc. 29th Int. Cosmic Ray Conf., Pune, **4**, 89 (2005).

[191] R.C. Rannot *et al.*, Proc. 29th Int. Cosmic Ray Conf., Pune, **4**, 355 (2005).

[192] J. Holder *et al.*, Proc. 29th Int. Cosmic Ray Conf., Pune, **5**, 379 (2005).

[193] J. Perkins *et al.*, Proc. 29th Int. Cosmic Ray Conf., Pune, **4**, 423 (2005).

[194] S. Vernetto *et al.*, Proc. 29th Int. Cosmic Ray Conf., Pune, **4**, 375 (2005).

[195] P.K. Mohanty *et al.*, Proc. 29th Int. Cosmic Ray Conf., Pune, **6**, 21 (2005).

[196] A. Smith, Proc. 29th Int. Cosmic Ray Conf., Pune, Review, Rapporteur and Highlight Papers, **10**, 227 (2005).

[197] M. Amenomori *et al.*, Proc. 29th Int. Cosmic Ray Conf., Pune, **4**, 211 (2005).

[198] S. Danaher et al., Solar Energy 28 (1982) 355.

[199] D. A. Smith *et al.*, "Celeste: A Large Heliostat Array For Gamma-Ray Astronomy," Nucl. Phys. Proc. Suppl. **54B** (1997) 362.

[200] D. A. Smith *et al.*, "Mrk 421, Mrk 501, and 1ES 1426+428 at 100-GeV with the CELESTE Cherenkov telescope," arXiv:astro-ph/0608247.

[201] M. C. Chantell *et al.* [STACEE Collaboration], "Prototype Test Results of the Solar Tower Atmospheric Cherenkov Effect Experiment (STACEE)," Nucl. Instrum. Meth. A **408** (1998) 468 [arXiv:astro-ph/9704037].

[202] A. Daum *et al.*, "First results on the performance of the HEGRA IACT array," Astropart. Phys. **8** (1997) 1.

[203] P. Cogan *et al.*, Proc. 29th Int. Cosmic Ray Conf., Pune, **4**, 371 (2005).

[204] P. Vincent *et al.*, Proc. 29th Int. Cosmic Ray Conf., Pune, **5**, 163 (2005).

[205] R. W. Atkins *et al.* [Milagro Collaboration], "Observation of TeV gamma rays from the Crab nebula with Milagro using a new background rejection technique," Astrophys. J. **595** (2003) 803 [arXiv:astro-ph/0305308].

[206] A. Alolisio et al., "The ARGO-YBJ experiment in Tibet," Nuovo Cim. C24, 739 (2001); Z. Cao, "Status of the ARGO-YBJ experiment," G. Di Sciascio et al. "Selection of the primary cosmic ray light-component by muon detection at high altitude." 29$^{\text{th}}$ International Cosmic Ray Conference (ICRC) Pune, India (August 3 - August 10, 2005); I. Di Mitri, at CRIS 2006, Catania, Italy.

[207] T. Di Girolamo *et al.*, Proc. 29th Int. Cosmic Ray Conf., Pune, **4**, 431 (2005).

[208] G. Sinnis, A. Smith and J. E. McEnery, "HAWC: A next generation all-sky VHE gamma-ray telescope," astro-ph/0403096. G. Sinnis, "HAWC - A Bird's Eye View of the Extreme Universe"

[209] F. Aharonian *et al.* [H.E.S.S. Collaboration], "HESS observations of the galactic center region and their possible dark matter interpretation," arXiv:astro-ph/0610509.

[210] M. Amenomori, Journal-ref, Science, V. 3. n. 5798, p. . n. DOI and 1. 1. 1131702 [Tibet AS-gamma Collaboration], "Anisotropy and corotation of galactic cosmic rays," [astro-ph/0610671].

[211] O.C. de Jager and A. K. Harding, 1992, Astrophys. J. 396, 161.

[212] T. C. Weekes *et al.*, "Observation of TeV gamma rays from the Crab nebula using the atmospheric Cerenkov imaging technique," Astrophys. J. **342** (1989) 379.

[213] A.M. Hillas et al., 1998, Astrophys. J. 503, 744.

[214] F. Aharonian *et al.* [HESS Collaboration], "The HESS survey of the inner galaxy in very high-energy gamma-rays," Astrophys. J. **636** (2006) 777 [arXiv:astro-ph/0510397].

[215] S. Funk *et al.*, Proc. 29th Int. Cosmic Ray Conf., Pune, **4**, 123 (2005).

[216] G. Sinnis *et al.*, Proc. 29th Int. Cosmic Ray Conf., Pune, **4**, 81 (2005).

[217] R. W. Atkins *et al.* [The Milagro Collaboration], "Evidence for TeV gamma-ray emission from the galactic plane," Phys. Rev. Lett. **95** (2005) 251103 [arXiv:astro-ph/0502303].

[218] A. Smith *et al.*, Proc. 29th Int. Cosmic Ray Conf., Pune, **4**, 271 (2005).

[219] F. W. Stecker and M. H. Salamon, "The Gamma-Ray Background from Blazars: A New Look," Astrophys. J. **464**, 600 (1996) [astro-ph/9601120].

[220] V. Pavlidou and B. D. Fields, "The Guaranteed Gamma-Ray Background," Astrophys. J. **575**, L5 (2002) [astro-ph/0207253].

[221] S. Gabici and P. Blasi, "The gamma ray background from large scale structure formation," Astropart. Phys. **19**, 679 (2003) [astro-ph/0211573].

[222] T. Totani, "Gamma-ray bursts, ultra high energy cosmic rays, and cosmic gamma-ray background," Astropart. Phys. **11**, 451 (1999) [astro-ph/9810207].

[223] L. Bergstrom, J. Edsjo and P. Ullio, "Spectral gamma-ray signatures of cosmological dark matter annihilations," Phys. Rev. Lett. **87**, 251301 (2001) [astro-ph/0105048].

[224] P. Ullio, L. Bergstrom, J. Edsjo and C. G. Lacey, "Cosmological dark matter annihilations into gamma-rays: A closer look," Phys. Rev. D **66**, 123502 (2002) [astro-ph/0207125].

[225] D. Elsaesser and K. Mannheim, "Cosmological gamma ray and neutrino backgrounds due to neutralino dark matter annihilation," Astropart. Phys. **22**, 65 (2004) [astro-ph/0405347].

[226] D. Elsaesser and K. Mannheim, "Supersymmetric dark matter and the extragalactic gamma ray background," Phys. Rev. Lett. **94**, 171302 (2005) [astro-ph/0405235].

[227] S. Ando and E. Komatsu, "Anisotropy of the cosmic gamma-ray background from dark matter annihilation," Phys. Rev. D **73**, 023521 (2006) [astro-ph/0512217].

[228] P. J. H. Zhang and J. F. Beacom, "Angular Correlations of the MeV Cosmic Gamma Ray Background," Astrophys. J. **614**, 37 (2004) [astro-ph/0401351].

[229] S. Ando, E. Komatsu, T. Narumoto and T. Totani, "Angular power spectrum of gamma-ray sources for GLAST: blazars and clusters of galaxies," astro-ph/0610155.

[230] F. W. Stecker and M. H. Salamon, "GLAST and the extragalactic gamma ray background," astro-ph/9909157.

[231] J. E. McEnery, I. V. Moskalenko and J. F. Ormes, "GLAST: Understanding the high energy gamma-ray sky," astro-ph/0406250.

[232] U. Seljak, "Analytic model for galaxy and dark matter clustering," Mon. Not. Roy. Astron. Soc. **318** (2000) 203 [arXiv:astro-ph/0001493].

[233] J. A. Peacock and R. E. Smith, "Halo occupation numbers and galaxy bias," Mon. Not. Roy. Astron. Soc. **318** (2000) 1144 [arXiv:astro-ph/0005010].

[234] C. P. Ma and J. N. Fry, "Deriving the Nonlinear Cosmological Power Spectrum and Bispectrum from Analytic Dark Matter Halo Profiles and Mass Functions," Astrophys. J. 543 (2000) 503, [arXiv:astro-ph/0003343].

[235] J. Chiang et al., Astrophys. J. **452**, 156 (1995).

[236] A. W. Strong, I. V. Moskalenko and O. Reimer, "A new determination of the extragalactic diffuse gamma-ray background from EGRET data," Astrophys. J. **613**, 956 (2004) [astro-ph/0405441].

[237] M. Kachelriess and P. D. Serpico, "The Compton-Getting effect on ultra-high energy cosmic rays of cosmological Phys. Lett. B **640**, 225 (2006) [astro-ph/0605462].

[238] M. G. Hauser and E. Dwek, "The Cosmic Infrared Background: Measurements and Implications s," Ann. Rev. Astron. Astrophys. **39**, 249 (2001) [astro-ph/0105539].

[239] Y. T. Gao, F. W. Stecker and D. B. Cline, "The Lightest Supersymmetric Particle And The Extragalactic Gamma-Ray Background," Astron. Astrophys. **249**, 1 (1991).

[240] F. A. Aharonian *et al.* [HEGRA Collaboration], "Limits on the TeV flux of diffuse gamma rays as measured with the HEGRA air shower array," Astropart. Phys. **17**, 459 (2002) [astro-ph/0109145].

[241] V. Springel, "The cosmological simulation code GADGET-2," Mon. Not. Roy. Astron. Soc. **364** (2005) 1105 [astro-ph/0505010].

[242] V. Springel, N. Yoshida and S. D. M. White, "GADGET: A code for collisionless and gasdynamical cosmological simulations," New Astron. **6** (2001) 79 [astro-ph/0003162].

[243] M. Crocce, S. Pueblas and R. Scoccimarro, "Transients from Initial Conditions in Cosmological Simulations," astro-ph/0606505.

[244] K. M. Gorski, E. Hivon, A. J. Banday, B. D. Wandelt, F. K. Hansen, M. Reinecke and M. Bartelman, "HEALPix – a Framework for High Resolution Discretization, and Fast Analysis of Data Distributed on the Sphere," Astrophys. J. **622** (2005) 759 [astro-ph/0409513].

[245] A. Cooray and R. Sheth, "Halo models of large scale structure," Phys. Rept. **372** (2002) 1 [astro-ph/0206508].

[246] R. E. Smith *et al.* [The Virgo Consortium Collaboration], "Stable clustering, the halo model and nonlinear cosmological power spectra," Mon. Not. Roy. Astron. Soc. **341** (2003) 1311 [astro-ph/0207664].

[247] P. Gondolo and J. Silk, "Dark matter annihilation at the galactic center," Phys. Rev. Lett. **83**, 1719 (1999) [arXiv:astro-ph/9906391].

[248] L. Bergstrom, T. Bringmann, M. Eriksson and M. Gustafsson, "Gamma rays from Kaluza-Klein dark matter," Phys. Rev. Lett. **94**, 131301 (2005) [arXiv:astro-ph/0410359].

[249] N. Fornengo, L. Pieri and S. Scopel, "Neutralino annihilation into gamma-rays in the Milky Way and in external galaxies," Phys. Rev. D **70**, 103529 (2004) [arXiv:hep-ph/0407342].

[250] G. Bertone, D. Hooper and J. Silk, "Particle dark matter: Evidence, candidates and constraints," Phys. Rept. **405**, 279 (2005) [arXiv:hep-ph/0404175].

[251] C. Calcaneo-Roldan and B. Moore, "The surface brightness of dark matter: Unique signatures of neutralino annihilation in the galactic halo," Phys. Rev. D **62**, 123005 (2000) [arXiv:astro-ph/0010056].

[252] P. Erdogdu *et al.*, "Reconstructed Density and Velocity Fields from the 2MASS Redshift Survey," astro-ph/0610005.

[253] See the URL: `http://www-glast.slac.stanford.edu/`

[254] See the URL: `http://www.icrr.u-tokyo.ac.jp/em/`

[255] J. A. Goodman [Milagro Collaboration], "Recent results from the Milagro gamma ray observatory," Nucl. Phys. Proc. Suppl. **151**, 101 (2006). R. W. Atkins *et al.*, "TeV gamma-ray survey of the northern hemisphere sky using the Milagro Observatory," Astrophys. J. **608**, 680 (2004).

[256] F. Halzen and D. Hooper, "Gamma ray astronomy with IceCube," JCAP **0308**, 006 (2003) [astro-ph/0305234].

[257] G. Guillian *et al.* [Super-Kamiokande Collaboration], "Observation of the anisotropy of 10-TeV primary cosmic ray nuclei flux with the Super-Kamiokande-I detector," astro-ph/0508468.

[258] V. Berezinsky, M. Kachelriess and S. Ostapchenko, "Electroweak jet cascading in the decay of superheavy particles," Phys. Rev. Lett. **89**, 171802 (2002) [hep-ph/0205218].

[259] S. Lee, "On the propagation of extragalactic high-energy cosmic and gamma-rays," Phys. Rev. D **58**, 043004 (1998) [astro-ph/9604098].

[260] F. W. Stecker, M. A. Malkan and S. T. Scully, "Intergalactic photon spectra from the far IR to the UV Lyman limit for 0 $<$ z $<$ 6 and the optical depth of the universe to high energy gamma-rays," astro-ph/0510449.

Ringraziamenti

Varie persone hanno contribuito in vari modi a questo lavoro di tesi. Vorrei innanziattutto ringraziare il mio supervisore Gennaro Miele. Nel corso di questi anni, durante la tesi di laurea prima e il dottorato adesso, è stato un costante punto di riferimento, per ogni questione di fisica, per le discussioni critiche e puntuali, e per il suo continuo incoraggiamento ed entusiasmo nel proporre nuove idee che mi hanno fatto avvicinare a nuovi ed affascinanti temi di ricerca. Lo ringrazio inoltre per le correzioni durante le varie fasi della stesura della tesi e per averne migliorato la leggibilità.

Un ringraziamento è dovuto a tutte le persone con cui ho collaborato in questi anni, il gruppo di astroparticelle di Valencia, di Aarhus ed il gruppo di Astronomia di Napoli. Ringrazio, in particolare, il dott. Pasquale Serpico, per l'instancabile lavoro durante le varie collaborazioni e per le innumerevoli discussioni di fisica sui temi più diversi.

Ringrazio, i vari membri del gruppo di Astroparticelle di Napoli per la continua collaborazione e l'aiuto non solo in faccende di fisica. Grazie anche per le varie simpatiche "astrocene" trascorse insieme. Ringrazio, in particolare, Giampiero Mangano per un filetto Wellington che difficilmente scorderò.

Vorrei ringraziare i vari "abitanti" dell'aula dottorandi che si sono succeduti nel corso dei tre anni e che hanno contribuito a rendere un po' piu' movimentata la permanenza all'università al di là degli impegni di lavoro.

Per i due mesi intensi e piacevoli trascorsi a Valencia, per aver condiviso il suo appartamento e per aver esplorato un po' di Spagna insieme ringrazio il mio amico Celio Moura.

Ringrazio, infine, la mia famiglia per l'affetto, il sostegno ed il calore che mi hanno sempre accompagnato in questi anni.